

Electron Paramagnetic Resonance Spectroscopy of Conjugated Polymers and Fullerenes for Organic Photovoltaics

Dissertation zur Erlangung des
naturwissenschaftlichen Doktorgrades
der Julius-Maximilians-Universität Würzburg



vorgelegt von

Friedrich Andreas Sperlich

aus Essen

Würzburg 2013

Eingereicht am: 2013-05-06
bei der Fakultät für Physik und Astronomie

1. Gutachter: Prof. Dr. Vladimir Dyakonov
2. Gutachter: PD. Dr. Achim Schöll
der Dissertation.

1. Prüfer: Prof. Dr. Vladimir Dyakonov
2. Prüfer: PD. Dr. Achim Schöll
3. Prüfer: Prof. Dr. Matthias Kadler
im Promotionskolloquium.

Tag des Promotionskolloquiums: 2013-09-06

Doktorurkunde ausgehändigt am:

Contents

1	Introduction	5
2	Organic Semiconductors for Photovoltaics	9
2.1	Organic Semiconductors	9
2.2	Excited Singlet and Triplet States	10
2.3	Organic Solar Cells	11
2.4	Used Materials	13
3	Electron Paramagnetic Resonance	17
3.1	Zeeman Splitting	17
3.2	Spin- $1/2$ Systems	18
3.2.1	The g-Factor and EPR Powder Spectra	19
3.2.2	Line Broadening	20
3.3	High-Frequency EPR	23
3.4	Electron–Electron Interactions	25
3.4.1	The Anisotropic Dipole-Dipole Interaction – D	25
3.4.2	The Isotropic Exchange Interaction – J	27
3.4.3	Eigenstates and Base Transformations	28
3.5	Spin-Coupled Radical Pairs	32
3.6	Triplet Excitons	34
3.7	Polaron Pairs	37
3.8	Optically Detected Magnetic Resonance	37
4	Experimental Section	41
4.1	Sample Preparation	41
4.2	The X-Band EPR Spectrometer	41
4.2.1	Continuous Wave EPR	43
4.2.2	Time-Resolved EPR	44
4.2.3	Optically Detected Magnetic Resonance	45
4.3	Photo-Induced Absorption – PIA	46

5	Results	49
5.1	Spectroscopic Signatures of Photo-Generated C ₇₀ -Fullerene Radical Anions	49
5.1.1	Introduction	50
5.1.2	Experimental Details	51
5.1.3	Results	52
5.1.4	Discussion	60
5.1.5	Conclusion	62
5.2	CT in Polymer:PC ₆₀ BM:PC ₇₀ BM Ternary Blends: Which Fullerene Gets the Electron?	63
5.2.1	Introduction	64
5.2.2	Experimental Details	66
5.2.3	Results	68
5.2.4	Discussion	76
5.2.5	Conclusion	76
5.3	(Ir-)Reversible P3HT:O ₂ Interactions Studied by Spin-Sensitive Methods .	79
5.3.1	Introduction	80
5.3.2	Experimental Details	80
5.3.3	Results	82
5.3.4	Discussion	90
5.3.5	Conclusion	92
5.4	Temperature-Dependent Charge Separation Dynamics in P3HT:PC ₆₀ BM .	93
5.4.1	Introduction	94
5.4.2	Experimental Details	95
5.4.3	Results and Discussion	95
5.4.4	Conclusion	101
6	Summary	103
	Bibliography	108
7	Appendix	121
7.1	List of Useful Constants	121
7.2	Publications and Conference Contributions	122
7.3	Lebenslauf	126
7.4	Danksagung	127

1 Introduction

“Our dependence on fossil fuels amounts to global pyromania, and the only fire extinguisher we have at our disposal is renewable energy.”

Heermann Scheer, initiator of the “Erneuerbare Energien Gesetz”

The burning of fossil fuels emits CO₂ (carbon dioxide) which is the main reason for climate change due to the greenhouse effect. Nowadays the largest share of the world’s energy production comes from carbon based fossil fuels like coal and oil. This will change in the foreseeable future, either because we run out of easily accessible deposits of fossil fuels, or because of their rising costs. No matter whether it will be direct production costs or the cost of the environmental impact, that we cannot afford any more. This is illustrated in Figure 1.1. The usage of carbon based fossil fuels is a “short-term” intermediate chapter when compared to centuries of human development. Large-scale consumption did not start before the early 20th century. And even the most optimistic predictions do not see the deposits lasting for several centuries to come. We can therefore simply divide the time axis in *pre-* and *post-carbon age*. It is thus essential to shift our energy production to renewable energy resources. Especially direct sun-to-electricity conversion is the method of choice among sustainable energy sources. Compared to the world’s energy demand, the sun offers an almost infinite supply of free energy.

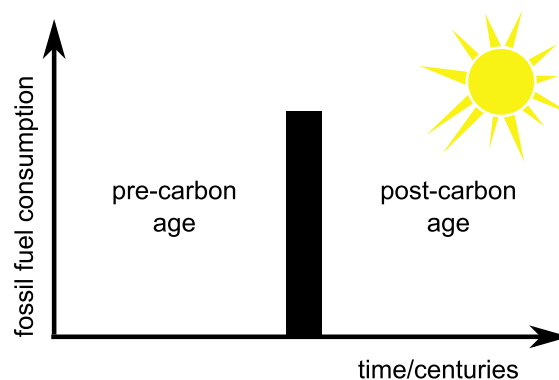


Figure 1.1: Usage of fossil fuels over time. The consumption period of carbon based fossil fuels is short, compared to centuries of human development. Sustainable energy resources need to be developed to lead humanity into the post-carbon age.

1 Introduction

As for solar cell technology, mainly three basic numbers are used for description: power conversion efficiency (PCE), module lifetime and costs per W_{peak} . Over the last half century there has been a race for even higher efficiencies and cheaper production lead by inorganic solar cell technologies. The best solar cells to date even reach a PCE of over 40 % [1]. However, this point of view does not consider that most solar cell technologies are dependent on scarce materials. When upscaling production to the terawatt scale needed for global supply, the available technologies would hit a natural resource limitation which might hold back their contribution to the energy production [2]. Therefore the cheapest or most efficient technology is not automatically the best choice for widespread adoption. Instead, the technology that can be upscaled the best will have a serious impact on energy production in the long run. This is where organic photovoltaics (OPV) come into play. The PCE of this technology still lacks behind considerably in comparison to commercial silicon based modules – the OPV record just topped 12 % PCE (Heliatek GmbH press release, jan. 2013). Also, availability, module lifetime and costs need improvement for a relevant market share. Despite these shortcomings the technology offers great opportunities for up-scaling. The light-absorbing materials are carbon-based and the solar cells themselves can be processed on cheap plastic foil in a role-to-role printing process [3]. Until now the production of this type of solar cells usually involves the need for indium-doped tin-oxide (ITO) as transparent anode and a metal back contact, which are again potentially limited materials. But recent developments point towards the possibility to produce completely metal-free organic solar cells, substituting mentioned limitations [4, 5, 6]. There is still a lot of fundamental research necessary to enable OPV to supply a substantial amount of energy production, but the outlook for this young technology is promising [7].

The method of electron paramagnetic resonance (EPR) and related techniques have proven extremely effective to study fundamental processes in organic solar cells. This is the case because most of the key processes that take place in an organic solar cell en route to photocurrent involve spin-carrying particles that can be directly addressed using spin-sensitive techniques. Also aging and loss-mechanisms, like energy loss via triplet excitons or oxygen induced degradation of the absorber materials can be characterized. At the same time not only dynamic processes are addressable, but the spin itself can be used as a measuring probe for its molecular environment.

For this thesis, advanced EPR methods were established in a newly found EPR research group at the chair for energy research (Experimental Physics VI) at the University of Würzburg. Two EPR spectrometers were constructed in the X-band (9.4 GHz) and Q-band (34 GHz) frequency range and especially the X-band machine was heavily upgraded with further equipment. In addition to the continuous wave operation

(cwEPR), the time-resolved analogue trEPR and the extremely sensitive method of optically detected magnetic resonance (ODMR) were implemented.

With this diverse instrumentation, fundamental processes in OPV absorbers were studied in great detail. Especially solution-processable light-absorbing conjugated polymers, fullerene derivatives and their excited states in solar cell blends were investigated. Apart from the common fullerene PC₆₀BM, a lot of attention was given to C₇₀-derivatives because most of the best-performing organic solar cells to date incorporate this molecule class. Yet, little was known about the spectroscopic signatures of C₇₀ and the specific differences to C₆₀-based molecules.

The thesis is organized as follows: First the basics of organic semiconductors and the working principle of organic solar cells are explained in Chapter 2. Then the theoretical background of EPR is introduced and the observed spectral features of excited states in OPV-materials are explained in the context of EPR theory (Chapter 3). Chapter 4 describes the experimental details of the used EPR spectrometers and related equipment. The main results are presented in Chapter 5, divided into four parts addressing different topics of this thesis. In 5.1 the spectroscopic signatures of polarons in polymer:fullerene bulk-heterojunctions are studied and – for the first time – the EPR signature and NIR-absorption band of the negative polaron localized on C₇₀-fullerenes are described. This research enables the directed study of the charge separated states in this class of OPV materials. This knowledge is used in 5.2 to resolve the minuscule energetic differences for an electron being localized on either C₆₀ or C₇₀ in a ternary OPV blend of a polymer with different fullerene derivatives. This material combination could help to make organic solar cells cheaper while maintaining maximum efficiency. The next part (5.3) deals with the light- and oxygen-induced degradation of the polymer P3HT. With the help of spin-sensitive methods, an important degradation pathway, involving triplet excited states of the polymer, could be identified. At last (5.4) the evolution of charge separation at the polymer:fullerene interface in an OPV blend is studied with time-resolved EPR. New insights into this process could be derived from the temperature dependence of the charge separation, suggesting a suppressed generation of free charge carriers at cryogenic temperatures.

2 Organic Semiconductors for Photovoltaics

This Chapter gives a general overview of organic semiconductors. The origin of the semiconducting properties of this material class and of the band-gap is explained. Excited states such as singlets, triplets and polarons are described in the context of organic solar cells. In the end, the materials that are the basis for this work and their properties are characterized. The more detailed discussion on the topic can be found in reviews by e.g. Deibel et al. [3] or Brabec et al. [8].

2.1 Organic Semiconductors

Organic semiconductors are carbon hydrates and can be divided into two main categories: molecular crystals and conjugated polymers. The first category consists of small molecules such as pentacene or fullerenes. Functional layers of these materials are often produced by thermal vapor deposition. They can form highly crystalline films with good electrical conductivity. The second category – conjugated polymers, are synthesized from repeating monomer units. Due to their size (typically >10 g/mol), they cannot be evaporated and are processed from solution. The results are mostly amorphous films with low conductivity and thus completely different electrical characteristics in comparison to the molecular crystals. What all of these materials have in common is a conjugated π -electron system. The carbon backbone of the molecules consists not only of single bonds, but also contains double or even triple bonds. The sp^2 -hybrid orbitals form σ -bonds while the additional non-hybrid p_z -orbitals of neighboring carbon atoms overlap and form delocalized π -bonds. These delocalized bond-electrons are the origin of conductivity in organic semiconductors. Since the π -bond is weaker than the σ -bond, a band-gap opens between the highest occupied molecular orbital (HOMO) and the lowest unoccupied molecular orbital (LUMO). Typical band-gap values are in the range of 1 to 3 eV, which covers the visual spectrum for photonic transitions. The electronic characteristics can be influenced by varying the chemical structure of backbone and side-chains. For example, variations in the spatial extent of

the π -conjugation change the optical band-gap, while the solubility and crystallinity of polymers can be influenced by aimed modifications of the side-chains. These exemplary modification are not necessarily straight forward, but they should demonstrate the vast possibilities to chemically engineer materials for their intended application.

2.2 Excited Singlet and Triplet States

When an incident photon with an energy larger than the band-gap is absorbed by an organic semiconductor, an electron is excited from the HOMO to the LUMO. The corresponding hole remains in the HOMO. The result is a bound electron-hole pair with singlet multiplicity ($S = 0$). In organic semiconductors, excitons are highly localized particles that are usually confined to one molecule or monomer (Frenkel exciton). This process is also described as an excitation from the molecule's singlet ground-state (S_0) to a singlet excited state (S_1 or higher) as shown in Figure 2.1. Higher singlet excitations (S_2, S_3, \dots) are omitted in this picture. Excitations to higher vibrational energies will relax fast to the lowest singlet energy by internal conversion (IC). This process is non-radiative and occurs on a fs time scale. Excited singlet states can radiatively recombine by emitting photoluminescence (PL) within typical time constants in the order of 1 ns. Higher vibrational energies of the ground-state can be involved yielding a red-shift of the emitted photons' wavelengths in comparison to the absorbed photons.

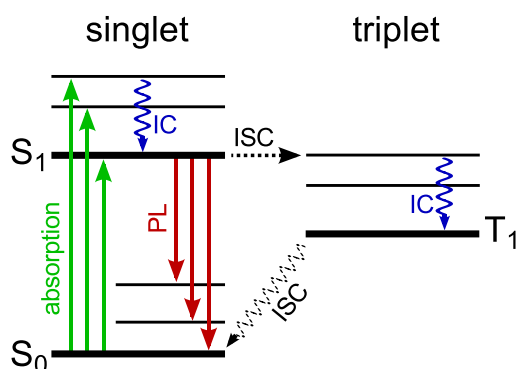


Figure 2.1: Absorption of photons creates singlet excitons that relax via internal conversion (IC) and subsequent photoluminescence (PL). Alternatively intersystem crossing (ISC) to the triplet state is possible.

A competing process is the transition to the triplet state with spin $S = 1$. The spin-forbidden transition between the singlet and triplet manifolds is called intersystem crossing (ISC). Due to spin-orbit coupling effects the spin is no exact quantum number in organic semiconductors and ISC is partially allowed. The lowest triplet state T_1 is always lower in energy than the lowest singlet S_1 because of the Pauli-principle. Higher

vibrational energies will again relax via IC. Triplet states in organic semiconductors are extremely long-lived and have typical lifetimes in the μs to ms range. The recombination is usually non-radiative, while radiative triplet recombination is referred to as phosphorescence.

2.3 Organic Solar Cells

In *inorganic* semiconductors excitons are delocalized states (Mott-Wannier exciton) with a Coulomb attraction of electrons and holes in the order of the thermal energy at room temperature ($k_B T = 25 \text{ meV}$). The main reason is the large dielectric constant of this material class ($\epsilon_r \approx 12$ for Si and GaAs). In this case the optical absorption leads directly to free charge carriers, which can be extracted as photocurrent from a solar cell.

In *organic* semiconductors, ϵ_r is between 3 and 4. Consequently excitons are highly localized particles that are usually confined to one molecule or monomer (Frenkel exciton) and have a Coulomb attraction of around 0.5 eV. In order to split them into separate charge carriers, the help of a material with higher electron affinity is necessary. The energy levels need to be aligned in a way that it is energetically favorable for the singlet exciton to split at the interface of these two materials. They are usually referred to as electron donor and electron acceptor.

The following part is focussed on solar cells consisting of conjugated polymers as electron donors and soluble fullerene derivatives as electron acceptors. However, many of the discussed aspects are similar for other OPV approaches.

Because of the short singlet lifetime ($\sim\text{ns}$) and resulting limited diffusion range, the next available donor:acceptor interface needs to be in the range of several nm. Otherwise the exciton will most probably recombine and its energy will be lost. For conjugated polymers, this is realized by the concept of the bulk heterojunction (BHJ) solar cell. The conjugated polymer and soluble fullerene-derivative are blended in solution and deposited together. The phases of both materials separate on a nm-scale and form an interdigitated network with an extremely large interface area. Percolation paths enable the charges to reach the electrodes. Because of the high optical absorption coefficients (typically $>10^7 \text{ m}^{-1}$), thin layers of the order of 100 nm are sufficient to absorb the incident light.

The absorption coefficient of conjugated polymers is much higher than for fullerenes, therefore the excitation usually takes place on the donor, as shown in Figure 2.2a. The singlet exciton will then diffuse randomly in the donor phase. When it reaches the donor:acceptor interface within its lifetime ($\sim\text{ns}$) it will undergo charge transfer (CT)

2 Organic Semiconductors for Photovoltaics

and an electron is transferred from the donor LUMO to the energetically favorable acceptor LUMO. If a photon is absorbed by the acceptor material as depicted in Figure 2.2b, a similar process takes place: After the singlet excitation and diffusion to the interface, a hole is transferred to the donor HOMO. Both processes take place on an ultrafast timescale within tens of fs. The result is the same with the hole being localized on the donor HOMO and the electron on the acceptor LUMO.

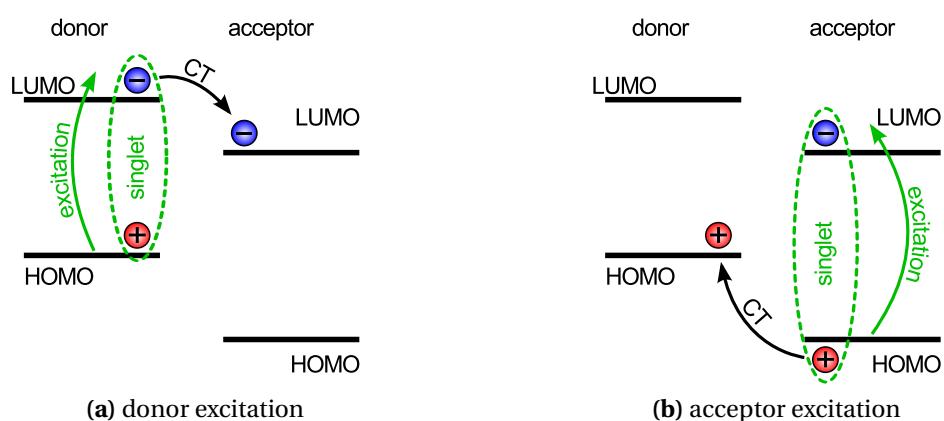


Figure 2.2: Light absorption creates singlet excitons, which can undergo charge transfer (CT) at the donor:acceptor interface. Excitation of (a) the donor or (b) the acceptor material yield the same result.

After the charge transfer, electron and hole are not necessarily free non-interacting particles. For many material combinations a charge transfer complex (CTC) is formed as depicted in Figure 2.3a. Electron and hole remain closely bound across the donor: acceptor interface, but might be separated by an externally applied electric field that overcomes their Coulomb attraction.

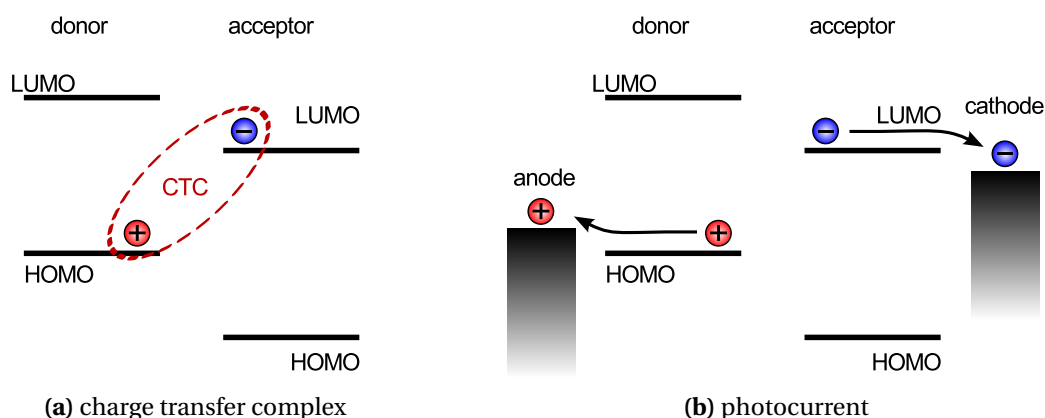


Figure 2.3: Light-induced charge transfer may yield a charge transfer complex (a). If the charges separate they can be extracted at the electrodes as photocurrent (b).

The charge carriers in organic semiconductors are also referred to as polarons. They are quasi-particles of the charge and its polarized molecular environment that diffuse together. The transport of polarons is a thermally activated hopping process from one molecule or polymer chain to the next one. In a solar cell configuration with anode and cathode the positive and negative polarons can be extracted as photocurrent (see Figure 2.3b). An extended discourse about transport phenomena and recombination kinetics is omitted here as these aspects of organic semiconductors are mostly irrelevant for this work.

2.4 Used Materials

Conjugated Polymers

The conjugated polymers that are the basis for this thesis are MEH-PPV, P3HT and PTB7. Their chemical structures are shown in Figure 2.4.

MEH-PPV – or poly[2-methoxy-5-(2'-ethyl-hexyloxy)-1,4-phenylenevinylene] consists of phenyl rings with added side-chains. Along the molecular backbone, the phenyl rings alternate with ethenyl groups. The band-gap is 2.2 eV and it has been used as a prototype material for both organic solar cells and light emitting diodes. Its derivative PPV was the first polymer for which electroluminescence was observed back in 1990 [9]. The material used for this work was purchased from Sigma-Aldrich.

P3HT (poly(3-hexylthiophene-2,5-diyl)) is polymerized from thiophene rings with a hexyl side-chain attached. It makes a difference whether the side-chain is regularly located at the second or third carbon atom or if the location is random. For a random order of the side-chains the material is classified as regio-random P3HT, which is an amorphous material with low conductivity. For usage in electronic devices P3HT is synthesized with all side-chains being attached to the third carbon atom. Hence they all point in the same direction. This material is called regio-regular P3HT and has a partially crystalline structure in solution-processed thin films and a much higher conductivity. The band-gap of 2.2 eV is comparable to that of MEH-PPV. The material used in this work has a high regio-regularity of $\approx 98\%$ and was purchased from Rieke Metals or BASF (product name sepiolid P200).

The polymer **PTB7** is a novel low band-gap donor-acceptor copolymer consisting of thieno[3,4-b]thiophene and benzodithiophene monomers. Its full name is poly[[4,8-bis[(2-ethylhexyl)oxy]benzo[1,2-b:4,5-b']dithiophene-2,6-diyl][3-fluoro-2-[(2-ethylhexyl)carbonyl]thieno[3,4-b]thiophenediyl]]. It has a band-gap of about 1.6 eV and can therefore absorb a much higher portion of the solar spectrum than P3HT or MEH-PPV.

2 Organic Semiconductors for Photovoltaics

Solar cells produced from PTB7:PC₇₀BM blends with power conversion efficiencies of over 9 % have been demonstrated [10, 11]. The used polymer batch was purchased from 1-Material.

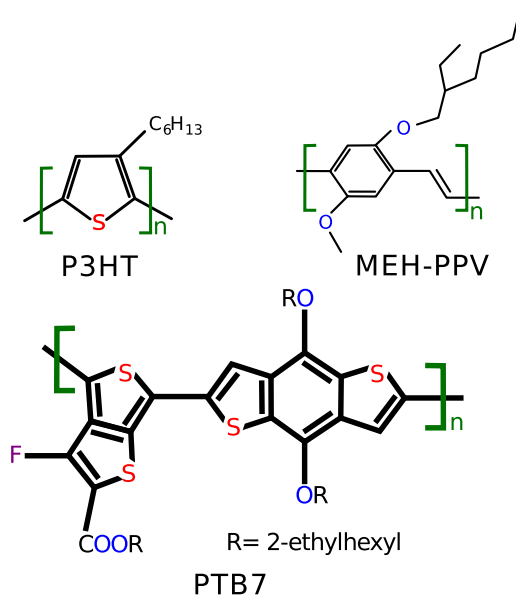


Figure 2.4: Donor-polymers P3HT, MEH-PPV and PTB7.

Fullerene Derivatives

Fullerenes are hollow spheres or ellipsoids composed of carbon atoms that are interconnected by alternating single and double bonds. There is a large variety of fullerenes with different numbers of carbon atoms. However the most common fullerene is the spherical C₆₀ that consists of 60 carbon atoms. Fullerenes are mostly produced by electrical arc-discharge from graphite electrodes in a helium atmosphere. Thus it is not surprising that they do also occur naturally under similar conditions in outer space [12]. Additionally, fullerenes could be identified on earth in carbon-rich rock [13].

Fullerenes and their derivatives are the best working acceptor material class for organic solar cells due to several reasons. They are spherical and can therefore accept electrons from any direction, which makes them ideal for incorporation into a BHJ. Also, after charge transfer from a donor material, the electron delocalizes over the whole fullerene and therefore hinders direct back recombination. Additionally the LUMO level of fullerenes is low enough so that they have a far higher electron affinity than most donors. Their downside is the low optical absorption coefficient, especially for C₆₀-derivatives. For fullerenes with lower symmetry the transition dipole moment is larger, resulting in a stronger absorption. This is the main reason why C₇₀-based acceptors are used in many of the most efficient organic solar cells.

The solubility of raw fullerenes is very limited in most solvents. therefore they can only be processed by thermal vapor deposition. The addition of side-chains enables processing fullerenes from solution. The most studied of these soluble fullerene derivatives is PC₆₀BM ([6,6]-phenyl-C₆₁-butyric acid methyl ester), but PC₇₀BM is also very common.

For this work, a variety of different fullerene derivatives has been investigated. Their chemical structures are shown in Figure 2.5. PC₆₀BM and PC₇₀BM were purchased from Solenne B.V. The other compounds are non-commercial and have been synthesized in the group of Nazario Martín in Madrid, Spain.

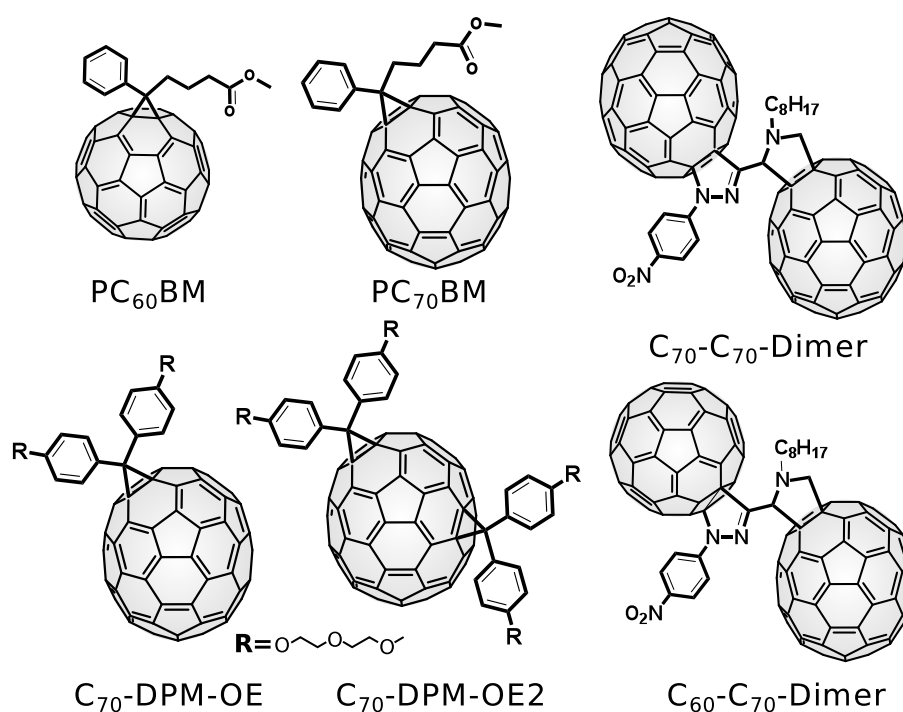


Figure 2.5: Fullerene derivatives used in this work.

For the new C₇₀-DPM-OE each phenyl group of the diphenylmethanofullerene (DPM) moiety is decorated with a solubilizing oligoether (OE) chain. For the C₇₀-DPM-OE2 bis-adduct two of these side-groups were attached. The synthesis has been carried out as reported for related compounds [14]. The fullerene dimers consist of one C₆₀- and one C₇₀-fullerene (hetero-dimer) or two C₇₀-fullerenes (homo-dimer). They are linked through a 2-pyrazoline moiety and a pyrrolidine ring. An octyl side-chain is added for enhanced solubility. Details about the synthesis of the fullerene dimers have been reported by Delgado et al. [15].

3 Electron Paramagnetic Resonance

This Chapter describes the theoretical background for electron paramagnetic resonance (EPR) and links the given formalism to relevant excited species, found in organic semiconductors. These are polarons or radical anions and cations, which are EPR-active spin- $1/2$ particles, as well as spin-1 triplet excitons, along with charge transfer complexes and polaron pairs, that can be described as strongly- to loosely-bound spin-interacting electron and hole. The shown formalism is based on the EPR book “Elementary Theory and Practical Applications” from John R. Weil, James R. Bolton and John E. Wertz [16], as well as the Ph.D. thesis of Stefan B. Knorr [17] and a review paper about electron–electron interactions by Gunnar Jeschke [18].

3.1 Zeeman Splitting

The origin of EPR is the Zeeman effect of paramagnetic particles with spin $S > 0$. Every spin-carrying particle has a magnetic moment μ , which leads to an energetic splitting in a magnetic field. Figure 3.1 shows this for a system with spin- $1/2$. The splitting is proportional to the magnetic field strength. Photons, which are in resonance with the Zeeman splitting (same energy) can induce transitions between the spin up $|\uparrow\rangle$ and spin down $|\downarrow\rangle$ state. For typical magnetic field values larger than 0.3 T this means microwave irradiation. When sweeping the magnetic field B , the transitions can be observed as microwave absorption (red). In a continuous wave EPR spectrometer usually the first derivative is recorded (blue).

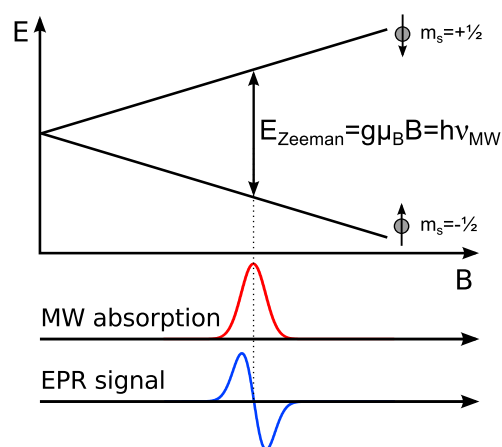


Figure 3.1: Zeeman-splitting for a spin- $1/2$ particle with microwave absorption and EPR signal in 1st derivative.

Multiplicity

The (spin-) multiplicity is equal to the number of quantized orientations of the spin direction vector of a spin-carrying particle in a magnetic field. It is given by the value of $2S + 1$, where S is the total spin quantum number of the system. The magnetic spin quantum number m_s of the respective orientation is ranging from $-S$ to S .

$$m_s = \underbrace{-S, -S + 1, \dots, S - 1, S}_{2S+1 \text{ values} = \text{multiplicity}} \quad (3.1)$$

Figure 3.2 gives an overview of the possible spin configurations of two spins S_a and S_b in an external magnetic field B_{ext} . The multiplicities are 1, 2 and 3 for singlet, doublet and triplet, respectively.

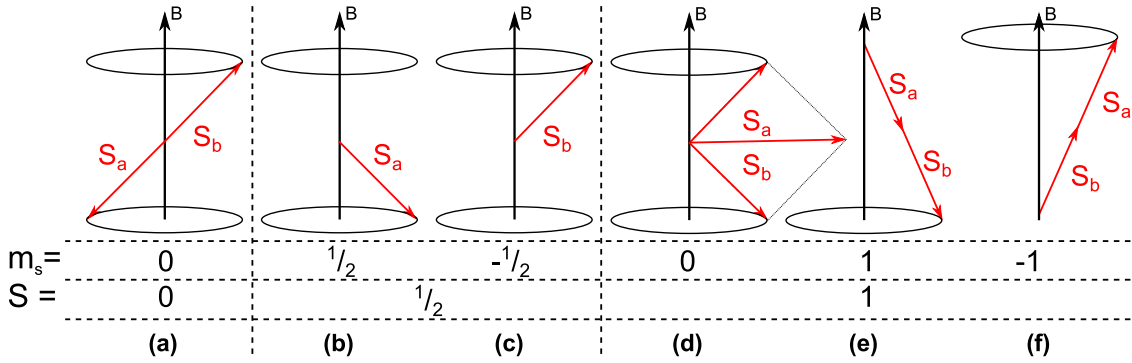


Figure 3.2: Multiplicity and orientation of two spins S_a and S_b in an external magnetic field. (a) singlet state of two spins with combined spin $S = 0$. (b), (c) spin-doublet of a spin- $1/2$ state. (d)-(f) Two spins in a triplet-state with $S = 1$.

3.2 Spin- $1/2$ Systems

The most simple system to be studied with EPR is a spin- $1/2$ particle; e.g. a free electron. The Hamiltonian for this system in an external magnetic field with field vector \mathbf{B}_{ext} is given by:

$$\mathcal{H} = g\mu_B \mathbf{S} \cdot \mathbf{B}_{\text{ext}} \quad (3.2)$$

Here, g is the electron g -factor or Landé-factor, μ_B the Bohr magneton and \mathbf{S} the spin operator vector, whose components are the Pauli matrices. The eigenstates of this system are spin up $|\uparrow\rangle$ and down $|\downarrow\rangle$ and the eigenenergies are:

$$\begin{aligned} |\downarrow\rangle: E_{\downarrow} &= +\frac{1}{2}g\mu_B B_{\text{ext}} \\ |\uparrow\rangle: E_{\uparrow} &= -\frac{1}{2}g\mu_B B_{\text{ext}} \end{aligned} \quad (3.3)$$

The resonance condition for EPR is then:

$$\Delta E_{\text{Zeeman}} = g\mu_B B_{\text{ext}} \Delta m_s = h\nu_{\text{MW}} \quad (3.4)$$

The Zeeman splitting energy is equal to the energy difference of spin up and down states, while $\Delta m_s = 1$ is the transition selection rule for EPR. The resonance condition is fulfilled, if the Zeeman splitting is equal to the energy of microwave photons with frequency ν_{MW} .

3.2.1 The g -Factor and EPR Powder Spectra

The g -factor is a unit-less number, that – in simple terms – gives the proportionality between the magnetic field strength and the resulting Zeeman splitting. The g -factor of the free electron is one of the best known natural constants and is ¹

$$g = 2.002\ 319\ 304\ 361\ 53(53). \quad (3.5)$$

In the solid state, the observed g -factor for a spin-1/2 particle deviates from this value due to interactions with the atomic environment. A charge localized on a molecule or at a specific position in a crystal is also subjected to the orbital momentum of the molecular orbital (spin-orbit coupling) or the crystal field, respectively. The influence acts as a local magnetic field being superimposed with the externally applied magnetic field \mathbf{B}_{ext} . This shifts the spectral position of the observed resonance transition and therefore the g -factor of the charge carrier. For materials consisting of light atoms ($Z < 30$) the shift of the g -factor is relatively small. For charges localized on organic semiconductors typical g -factors are within the range of $1.9 < g < 2.1$. All polarons and radical anions studied in this thesis fall into this category.

For localized charges the molecular / crystal environment is usually anisotropic and therefore interactions depend on relative orientations. The g -factor is then described as a second-order tensor to represent this orientation dependence. This tensor can always be diagonalized and is fully defined by the components of its principal axis: g_{xx}, g_{yy}, g_{zz} .

$$\mathbf{g} = \begin{pmatrix} g_{xx} & 0 & 0 \\ 0 & g_{yy} & 0 \\ 0 & 0 & g_{zz} \end{pmatrix} \quad (3.6)$$

For oriented samples, like single crystals, the observed spectral position of the transition shifts between the values defined by the g -tensor components, in dependence

¹Jan. 2013: <http://physics.nist.gov/cuu/Constants/index.html>

of the relative orientation of the crystal axis towards the external magnetic field vector. For unoriented samples, like amorphous solids or crystal powders, the orientation is statistically distributed. This leads to the observation of so-called “powder spectra”, where the spectrum is spread over the full range of the g -tensor components. Despite the statistical nature of the g -tensor orientation, the symmetry of the system is expressed in the spectrum. Figure 3.3 shows X-band (9.4 GHz) simulations for several powder spectra of spin- $1/2$ systems with different symmetry. The isotropic case has no orientation dependence. If two g -tensor components are identical (g_{\perp}) and one deviates (g_{\parallel}), the system has axial symmetry and the EPR signal is asymmetric with a characteristic bump at the position of g_{\parallel} . If all three g -tensor components are different, the system has rhombic symmetry. The spectrum is not to be mistaken with one of three independent spin- $1/2$ particles as shown in Figures 3.3c and 3.3d.

For spins in liquid or gaseous samples, the observed spectra differ from the same sample measured in the solid state – e.g. in frozen solution. In non-solid samples molecular motion and spinning is usually faster than spin relaxation times and this leads to an averaging of the observed spectrum. Only a broadened isotropic line is observed at the spectral position of the averaged g -factor $g_{\text{iso}} = \frac{1}{3}(g_{xx} + g_{yy} + g_{zz})$.

3.2.2 Line Broadening

There are various mechanisms, that result in *homogeneous* and *inhomogeneous* broadening of EPR spectra. Several, relevant for this work, are discussed here. The natural lineshape for dipole transitions is a Lorentzian profile, with the width being determined by the inverse lifetime of the observed transition – also called natural linewidth. Processes that shorten this lifetime are homogeneous, while all other interactions lead to inhomogeneous broadening, which is often of Gaussian shape. Most of these mechanisms are due to differences in the local environment. Usually several broadening mechanisms apply at the same time, resulting in a Voigt profile – the convolution of Gauss and Lorentz functions.

Homogeneous Broadening

Saturation of the EPR transition at sufficiently high microwave powers has the effect that not only regular microwave photon absorption, but also stimulated emission occurs. This leads to a reduction of the effective radiative lifetime and consequently, a homogeneous broadening of the EPR spectrum. Additionally, the population of upper and lower spin states are equalized and the observed EPR intensity saturates.

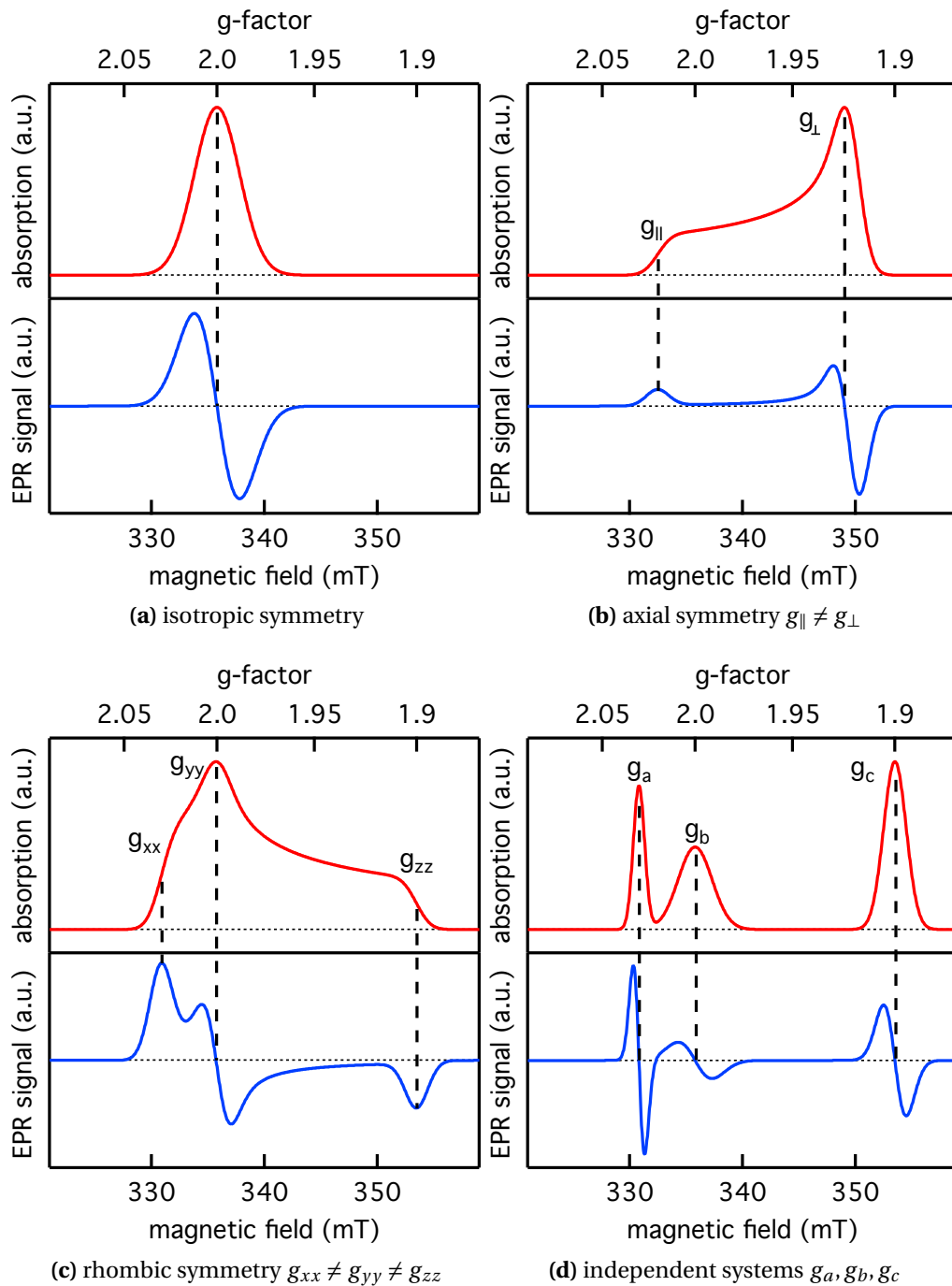


Figure 3.3: Simulation of EPR powder spectra for spin-1/2 systems. **red:** absorption spectra, **blue:** EPR signals in 1st derivative. **(a)** for a spin system with isotropic symmetry ($g_{xx} = g_{yy} = g_{zz} = 2.0$), **(b)** axial symmetry ($g_{\parallel} \neq g_{\perp}$), **(c)** rhombic symmetry ($g_{xx} \neq g_{yy} \neq g_{zz}$), **(d)** three independent spin systems with different g -factors and linewidths.

Inhomogeneous Broadening

Dipole–dipole interactions with nearby spin carrying particles of the same or different kind are possible. The second particle has its own local magnetic field, which superimposes with the external magnetic field and thus shifts the resonance field for the first particle. If distances are statistically distributed, a Gaussian broadening can be expected. This mechanism is directly related to the description of systems with vanishingly small dipole interaction D later in this Chapter (3.7).

Unresolved hyperfine interactions are also a type of dipole–dipole interaction. In this case with the spins of surrounding nuclei. If the number of interacting nuclei is very large, no individual hyperfine structure with a discrete splitting in the EPR spectrum is observed. Instead, the spectrum is averaged over many possible hyperfine interactions. Hence one detects the envelope of all lines. This effect is also observed for the linewidth of polarons in organic semiconductors, where it is referred to as **motional narrowing**. The electronic mobility and hence the diffusive motion of polarons is here strongly temperature dependent. Therefore the amount of protons that interact with a polaron in a given time are a function of mobility and temperature. At cryogenic temperatures, a broadening of the detected linewidth due to unresolved hyperfine interactions with these surrounding protons is observed. At higher temperatures the same mechanism yields a narrowing of the linewidth [19, 20, 21] and Ref. [22] (p. 511).

An inhomogeneous external magnetic field might be applied to the sample, setting a lower limit to the observable linewidth. A typical Bruker X-band EPR magnet has a local homogeneity of $\sim 10^{-6}$ over the sample width of 3 mm. However this needs serious consideration for superconducting magnets, which are usually a lot less homogeneous.

Modulation broadening is present if the modulation amplitude, expressed in magnetic field units, cannot be considered small in comparison to the observed linewidth. In general it is safe to apply a field modulation, that is less than half of the observed linewidth, to avoid spectral distortions.

All the broadening mechanisms presented above are isotropic. Hence, the whole EPR spectrum is convoluted with the additional broadening profile. However, for many spin-systems the linewidth also needs to be considered anisotropic. This is typically expressed by the **g-strain** tensor, which compliments the g -factor tensor. The strain can be understood as a measure of the heterogeneous environment, when one or another g -tensor component is not exactly determined any more, mainly owing to the interaction with the environment. In a first order approximation, the bigger the initial shift of the g -tensor component from the free electron g -factor g_e , the stronger the g -strain effect.

3.3 High-Frequency EPR

There are two main advantages of performing EPR experiments at high magnetic fields and high frequencies (HFEPR): First the spectral or g -factor resolution is enhanced, as it is directly proportional to the microwave frequency. And second the sensitivity is increased, due to larger spin polarization of the Zeeman sublevels. The theoretical basics are given here, while the measurement specific settings for the HFEPR spectrometers used for this thesis, will be described in the respective results Chapter.

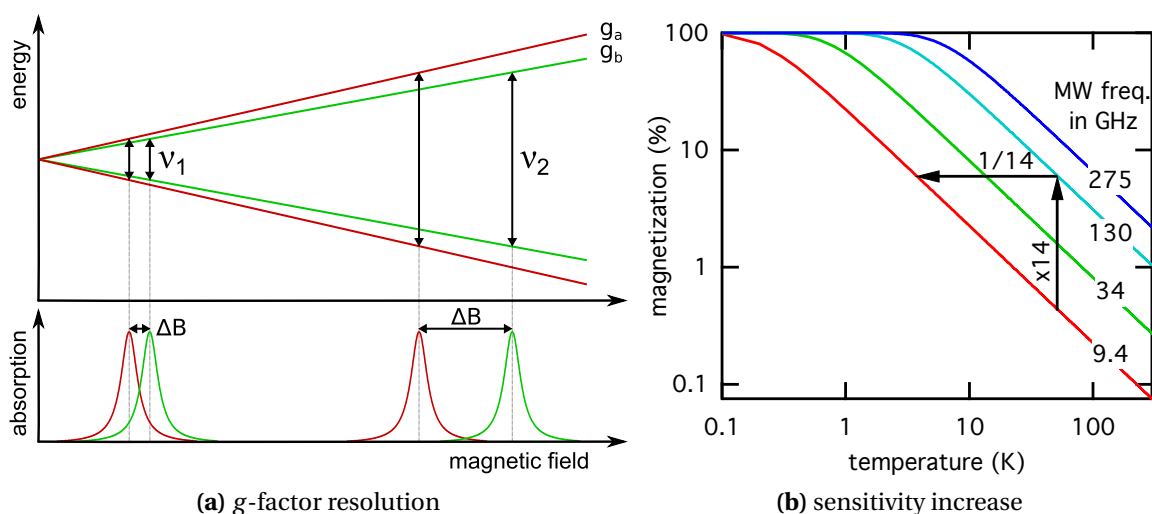


Figure 3.4: Advantages of HFEPR: **(a)** Resolution enhancement for HFEPR: At frequency ν_1 the two EPR lines are almost completely overlapping. When detecting the same spectrum at the higher frequency ν_2 the two lines are well separated. **(b)** Higher frequencies result in higher magnetization at a given temperature.

g -Factor Resolution

The g -factor resolution of an EPR spectrometer can be defined easiest for two spins with similar g -factors and isotropic lineshapes. This example is depicted in Figure 3.4a. The magnetic field splitting ΔB for two spins with g -factors g_a and g_b is directly proportional to the microwave frequency ν_{MW} of the EPR spectrometer:

$$\Delta B = \left(\frac{1}{g_a} - \frac{1}{g_b} \right) \frac{h\nu_{MW}}{\mu_B} \quad (3.7)$$

This does of course also enhance the resolution for spin systems with lower g -tensor symmetry. However, the splittings due to exchange and dipolar interaction described in the next Chapter are independent of the spectrometer frequency.

Spin Polarization

Spin polarization describes a deviation of the even population distribution between Zeeman sublevels – i.e. more spins are in the upper or lower spin state. In a magnetic field, spins are aligned along quantized orientations according to their multiplicity. If the energy splitting $\Delta E_{\text{Zeeman}} = g\mu_B B_{\text{ext}}$ between two orientations spin up (\uparrow) and spin down (\downarrow) is much smaller than the thermal energy $k_B T$, polarization is described by the Boltzmann distribution:

$$\frac{N_{\downarrow}}{N_{\uparrow}} = \exp\left(-\frac{\Delta E_{\text{Zeeman}}}{k_B T}\right) = \exp\left(-\frac{g\mu_B B_{\text{ext}}}{k_B T}\right) \quad (3.8)$$

Where N_{\downarrow} and N_{\uparrow} are the number of spins in the respective spin state. With this the macroscopic magnetization M of the sample can be expressed by spin populations:

$$M = \frac{N_{\uparrow} - N_{\downarrow}}{N_{\uparrow} + N_{\downarrow}} \quad (3.9)$$

The sensitivity of a cw EPR experiment is directly depending on the magnetization. In Figure 3.4b, the magnetization is plotted over temperature for several microwave frequencies used in EPR spectrometers. To achieve higher magnetization an increase in the operating frequency (and magnetic field) is equivalent to lowering the thermal energy $k_B T$ by the same factor. This is illustrated by the two arrows: the factor of ~ 14 for going from X-band (9.4 GHz) to D-band (130GHz) corresponds to lowering the temperature by the same factor.

For certain spin systems also so-called non-thermal spin polarizations and inverted populations are possible. In the latter case, this can result in (stimulated) microwave emission instead of absorption. Examples are the spin coupled radical pair described later in this Chapter (see Section 3.5) with a spin polarization of $m_s = 0$ states; or optically pumping an organic semiconductor to construct a maser using spin-polarized triplet excitons [23].

3.4 Electron–Electron Interactions

There are two major magnetic interactions for neighboring spin-carrying particles: exchange and dipolar interaction. The Hamiltonian for such a system of two interacting spins can be expressed in the following form:

$$\mathcal{H} = \underbrace{-J\mathbf{S}_a \cdot \mathbf{S}_b}_{\text{exchange interaction}} - \underbrace{\mathbf{D}(3S_a^Z S_b^Z - \mathbf{S}_a \cdot \mathbf{S}_b)}_{\text{dipolar interaction}} \quad (3.10)$$

Here J is the isotropic exchange interaction, \mathbf{D} is the anisotropic dipole–dipole coupling tensor, particles a and b have the spin operator vectors \mathbf{S}_a , \mathbf{S}_b and S_a^Z , S_b^Z are their projections in the Z -direction. The nuclear hyperfine interaction A is omitted, as it is not observed for the systems presented in this thesis.

The parameter J and the scalar representation D of the dipolar coupling are energy values, but they are usually handled in frequency (J/h , D/h) or magnetic field units (J' , D'). This is convenient as the output spectra from pulsed or cw EPR spectrometers are typically handled in MHz or mT. The relation between the two is:

$$\begin{aligned} D/h[\text{MHz}] &= \frac{g\mu_B}{h} D'[\text{mT}] \\ J/h[\text{MHz}] &= \frac{g\mu_B}{h} J'[\text{mT}] \end{aligned} \quad (3.11)$$

Here g is the g -factor of the spin system and the conversion factor $\frac{g\mu_B}{h} = 28.025 \frac{\text{MHz}}{\text{mT}}$ for $g = 2.00232$.

3.4.1 The Anisotropic Dipole-Dipole Interaction – D

The dipole–dipole coupling results from the interaction of magnetic moments of neighboring spins. One spin a is subjected to a shift of its local magnetic field due to the magnetic moment of spin b and vice versa. This results in an energy splitting observable with spectroscopy, such as EPR. Because it is independent of the applied external magnetic field and present even without, it is also called zero-field splitting. Like the name suggests, the dipolar coupling is an anisotropic interaction which is described by a second order tensor to express its direction dependency:

$$\mathbf{D} = \begin{pmatrix} D_{xx} & 0 & 0 \\ 0 & D_{yy} & 0 \\ 0 & 0 & D_{zz} \end{pmatrix} = \begin{pmatrix} \frac{1}{3}D - E & 0 & 0 \\ 0 & \frac{1}{3}D + E & 0 \\ 0 & 0 & -\frac{2}{3}D \end{pmatrix} \quad (3.12)$$

3 Electron Paramagnetic Resonance

The \mathbf{D} tensor is set traceless (the sum of all diagonal elements is zero) and symmetric ($D_{i,j} = D_{j,i}$). It is fully described by the two scalar parameters D and E :

$$D = -\frac{3}{2}D_{zz} \quad (3.13)$$

$$E = \frac{1}{2}(D_{yy} - D_{xx}) \quad (3.14)$$

D is the zero field interaction parameter and E is the rhombicity – it is the off-axial interaction strength for systems with symmetry lower than axial symmetry. If $E = 0$, the spins are considered to be point-objects, which is also called the point-dipole approximation for $|E| \ll |D|$. It is important to note that the values of D and E are not unique. They depend on which axis is chosen as Z . It is always possible to choose Z , such that $|E| \leq |\frac{D}{3}|$. Both values may be positive or negative and may have opposite signs.

Because of the direct analytic relation, the value of D can be used to derive an estimate of the inter-radical distance r [18]. In the case of $E = 0$, the point-dipole approximation is valid and the derivation of an analytical formula for $D(r)$ is possible. The dipole-dipole splitting between two spins a and b is then given by:

$$D(r_{ab}, \Theta) = -\frac{3}{2} \frac{1}{r_{ab}^3} \frac{\mu_0 g_a g_b \mu_B^2}{4\pi} (3\cos^2\Theta - 1) \quad (3.15)$$

where r_{ab} is the inter-radical distance, g_a and g_b are the g -factors of the two spins, and Θ is the angle between the direction of the external magnetic field and the vector connecting the two spins (see also Figure 3.10a). For the special case of $g_a = g_b = g_e$, as well as $\Theta = 0$ and considering 3.11 we obtain a “rule of thumb” for $r(D')$:

$$r_{ab}(D')[\text{nm}] = \sqrt[3]{\frac{2.785}{D'(r)[\text{mT}]}} \text{nm} \quad (3.16)$$

In literature, other permutations of this formula are found and differ often, because they actually refer to D_{zz} or another possible orientation $\Theta \neq 0$.

With this, typical values for D' of a radical pair can be calculated. For an inter-radical distance of $r_{ab} = 1.77$ nm, the value of D' is equal to 0.5 mT. While at a distance of 3.82 nm the interaction is becoming negligible at 50 μT , as this is also the approximate value of earth’s magnetic field [24].

3.4.2 The Isotropic Exchange Interaction – J

The exchange interaction parameter J is the energetic separation of singlet and triplet wavefunction for two coupled spins. It has a complex dependence on the electronic properties of the radicals, their separation, and the nature of the intervening medium. $J(r)$ is usually assumed to fall off exponentially with r and to be independent of Θ :

$$J(r) = J_0 \cdot e^{-\beta r} \quad (3.17)$$

Where J_0 may be positive as well as negative and reported values lie in the range of $1.4 \cdot 10^{10} \text{ mT} \leq |J_0| \leq 8 \cdot 10^{10} \text{ mT}$. The value for β can be in the range of $(14\text{--}18) \text{ nm}^{-1}$ [18, 24, 25]. The minimal value pair of $1.4 \cdot 10^{10} \text{ mT}$, 18 nm^{-1} is an estimate for the upper [26] limit for isolating solids. Such exchange coupling is negligible for r_{ab} larger than $\sim 1.5 \text{ nm}$. However, the exchange interaction might reach extremely further in conjugated systems, because the wavefunction overlap extends along the conjugation. The simplified exponential dependency is then no longer valid [18].

Care must be taken when comparing literature values of J . In the Hamiltonian, J is often defined with opposite sign and twice the absolute value.

Comparison of D and J

Figure 3.5 shows a graphical representation of the strength and reach of exchange and dipolar coupling in magnetic field and frequency units. The dipolar coupling $D(r)$ usually has the longer range and dominates the exchange interaction $J(r)$, except at very small inter-radical separations. In contrast to that, D is negligible when compared to the background magnetic field of the earth for separations larger than 3–4 nm, which means free, non-interacting spins.

The influence of D and J on the observed spectrum can be separated into three regimes of interaction strength [18]. In the *strong coupling regime*, the spectrum is a pure triplet pattern. For *intermediate coupling*, the system can be described as spin-coupled radical pair (SCRIP), with a complex dependence of the spectrum on the specific parameter set. In the *weak coupling regime*, the parameters D and J are often smaller than the linewidth, resulting in a sole broadened line without discernible spectral features, as in case of polaron pairs. The boundary lines plotted in Figure 3.5 are by no means strict. Especially because of the complex dependence of $J(r)$ on the specific wavefunction in conjugated systems, deviations are possible. Before the three coupling regimes are discussed in more detail, an introduction of the the general energy terms and definition of transitions is necessary.

3 Electron Paramagnetic Resonance

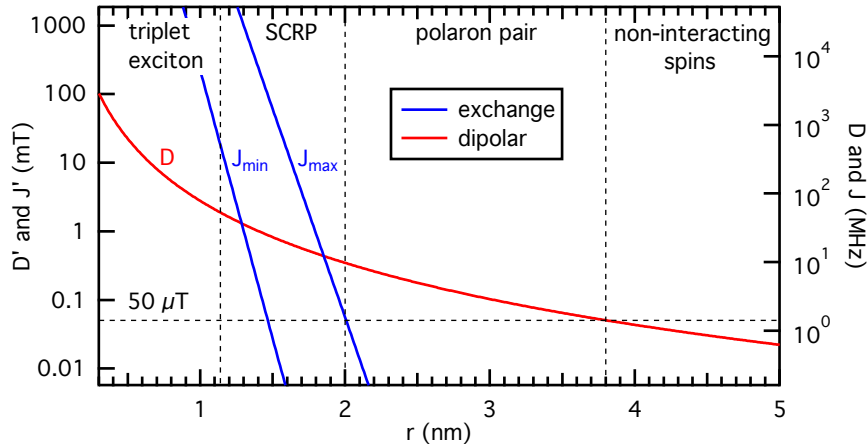


Figure 3.5: Simulation of dipolar and exchange interaction in dependence of the inter-radical distance r . Literature values were used for $J_{\min, \max}$, as stated in the text. For comparison, a dashed horizontal line at $50 \mu T$ represents the approximate strength of the earth's magnetic field.

3.4.3 Eigenstates and Base Transformations

When both dipolar and exchange coupling are present, the Hamiltonian 3.10 is non-diagonal in the product base of the two interacting spins. To calculate its eigenstates and transitions, a unitary transformation is necessary to diagonalize the Hamiltonian. This leads to the eigenstates $|1\rangle - |4\rangle$ in the SCRP base, which is the most general formulation.

<u>product base</u>	<u>ST base</u>	<u>SCRP base</u>	
$ \downarrow\downarrow\rangle$	$ T_{+1}\rangle$	$ 1\rangle$	
$ \uparrow\downarrow\rangle$	$ S\rangle = \frac{1}{\sqrt{2}}(\uparrow\downarrow\rangle - \downarrow\uparrow\rangle)$	$ 2\rangle = \cos(\phi) \uparrow\downarrow\rangle - \sin(\phi) \downarrow\uparrow\rangle$	(3.18)
$ \downarrow\uparrow\rangle$	$ T_0\rangle = \frac{1}{\sqrt{2}}(\uparrow\downarrow\rangle + \downarrow\uparrow\rangle)$	$ 3\rangle = \sin(\phi) \uparrow\downarrow\rangle + \cos(\phi) \downarrow\uparrow\rangle$	
$ \uparrow\uparrow\rangle$	$ T_{-1}\rangle$	$ 4\rangle$	

$$\phi = \frac{1}{2} \arctan\left(\frac{J-d}{h\Delta\nu}\right) \quad (3.19)$$

The mixing angle ϕ depends on the interaction strength $(J-d)$ and describes the base transformation to the product base ($\phi \rightarrow 0$) for weak coupling or the singlet triplet (ST) base for strong coupling ($\phi \rightarrow \pi/4$). The pure triplet states $|T_{\pm 1}\rangle$ are independent of this base transformation.

The formulation of the energies $E_1 - E_4$ in the SCRP base and the resulting transitions are completely general for all spin coupled systems in this thesis. All special solutions for the different coupling regimes can be directly derived.

$$\begin{aligned}
 E_1 &= h \left(+\nu_0 - \frac{1}{4}a \right) \\
 E_2 &= h \left(+\frac{1}{2}\Omega + \frac{1}{4}a \right) \\
 E_3 &= h \left(-\frac{1}{2}\Omega + \frac{1}{4}a \right) \\
 E_4 &= h \left(-\nu_0 - \frac{1}{4}a \right)
 \end{aligned} \tag{3.20}$$

The following abbreviations are used:

$$\begin{array}{ll}
 \underline{B_{\text{ext}} = \text{const.}} & \underline{\nu_{\text{MW}} = \text{const.}} \\
 a = \frac{1}{h} (J + 2d) & a' = J' + 2d' \\
 \Omega = \sqrt{\frac{1}{h^2} (J - d)^2 + \Delta\nu^2} & \Omega' = \sqrt{(J' - d')^2 + \Delta B^2} \\
 \Delta\nu = \nu_a - \nu_b & \Delta B = B_a - B_b \\
 \nu_0 = \frac{1}{2} (\nu_a + \nu_b) & B_0 = \frac{1}{2} (B_a + B_b) \\
 \nu_a = g_a \frac{\mu_B B_{\text{ext}}}{h} & B_a = \frac{1}{g_a} \frac{h\nu_{\text{MW}}}{\mu_B}
 \end{array} \tag{3.21}$$

ν_a and ν_b are the Larmor frequencies of the spin pair constituents and $\Delta\nu$ is the Larmor separation. $\Omega = \nu_{23}$ is the zero-quantum coherence frequency. That is the frequency with which the wavefunction is oscillating between singlet and triplet content. Both eigenstates $|2\rangle$ and $|3\rangle$ are $m_s = 0$ and hence the transition is called zero-quantum coherence. $h\Omega$ is the energy splitting between the states $|2\rangle$ and $|3\rangle$.

The representation of possible transitions is dependent on the experimental conditions under which they are observed. For pulsed EPR spectrometers usually the external magnetic field B_{ext} is kept constant and the transitions are observed as a function of delay times in microwave pulse sequences, which is transferred to a frequency axis by Fourier transformation. This leads to the formulation of transition frequencies in contrast to magnetic field positions for EPR experiments with constant microwave frequency ν_{MW} and magnetic field sweeps. Accordingly, B_a and B_b are the field positions of the separate spins with g -factors g_a and g_b , while ΔB is the field separation in a given spectrometer with fixed microwave frequency ν_{MW} . Because the formalism based on transition frequencies is more common in literature and the used spectrometer operates with a constant microwave frequency and field sweeps, both representations are discussed here side-by-side.

3 Electron Paramagnetic Resonance

The parameter d is a scalar representation of the dipolar coupling tensor \mathbf{D} with respect to the orientation of an external magnetic field $\vec{e}_{B_{ext}}$. The connection is the following, with possible simplifications for axial symmetry ($E = 0$) and orientation along \vec{z} ($\Theta = 0$), yielding the maximum value of $d = \frac{2}{3}D$.

$$d = \|\mathbf{D} \cdot \vec{e}_{B_{ext}}\| \stackrel{E=0}{=} D \left(\cos^2\Theta - \frac{1}{3} \right) \stackrel{\Theta=0}{=} \frac{2}{3}D = -D_{zz} \quad (3.22)$$

To calculate energies and transitions explicitly, the orientation needs to be defined first. Either by orienting a single crystal with respect to the magnetic field or by measuring an unoriented sample. The resulting powder spectrum can then be simulated as a superposition of all possible orientations. D is here in the high-field approximation ($D \ll g\mu_B B_{ext}$), which is in good agreement for all systems studied in this thesis.

Zero Magnetic Field

Vanishing magnetic field values $B_{ext} \rightarrow 0$ result in several boundary conditions: $\nu_a = \nu_b = \Delta\nu = \nu_0 = 0$ and accordingly $\Omega = \frac{1}{h}(J - d)$. The energy values from Equation 3.20 are then only defined by the values of J and d :

$$\begin{aligned} E_1 &= -\frac{1}{4}J - \frac{1}{2}d \\ E_2 &= +\frac{3}{4}J \\ E_3 &= -\frac{1}{4}J + d \\ E_4 &= -\frac{1}{4}J - \frac{1}{2}d \end{aligned} \quad (3.23)$$

Figure 3.6 shows E_1 to E_4 for zero (3.23) and rising magnetic field values (3.20) with orientation of the spin pair parallel to the external field ($\Theta = 0$) and exemplary values for $J \approx D$. Note the degeneracy of E_1 and E_4 at $B = 0$, which is lifted when applying a magnetic field $B > 0$.

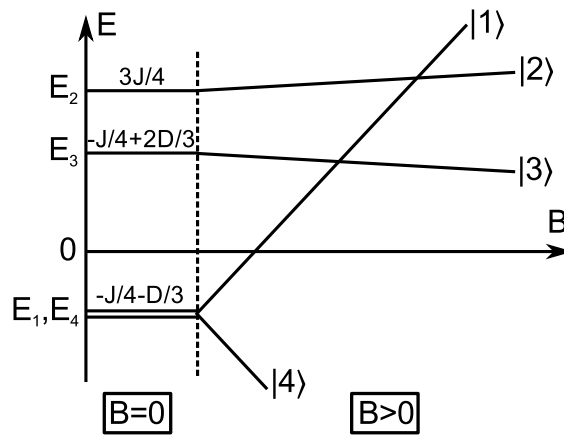


Figure 3.6: SCRP energy levels at zero magnetic field and for rising field values with $\Theta = 0$.

3.4 *Electron–Electron Interactions*

There are studies that give special attention to the intersections of E_1 with E_2 and E_3 for specific magnetic field values (see Figure 3.6), which results in resonant mixing of the according spin populations [24, 27]. This can be observed by their effect on spin polarization or influence on the balance of chemical reactions.

3.5 Spin-Coupled Radical Pairs

Spin-coupled radical pairs can be described in the frame of the *intermediate coupling regime* $|J - D| \approx h|\nu_a - \nu_b|$, which is the most general case. Strong and weak coupling can be derived and will be discussed afterwards. J and D are within the same order of magnitude for inter-radical separations of approximately 1–2 nm (compare Figure 3.5), which is large enough, that the point-dipole approximation is valid – hence $E = 0$.

The transition frequencies ν_{ij} or magnetic field positions B_{ij} for transitions from energy level $i \rightarrow j$ can generally be expressed in the SCRP base (3.18) for experiments with constant magnetic field or microwave frequency:

$$\begin{array}{ll}
 \underline{B_{\text{ext}} = \text{const.}} & \underline{\nu_{\text{MW}} = \text{const.}} \\
 \nu_{24} = \nu_0 + \frac{1}{2} (+\Omega + a) & B_{24} = B_0 + \frac{1}{2} (-\Omega' - a') \\
 \nu_{13} = \nu_0 + \frac{1}{2} (+\Omega - a) & B_{13} = B_0 + \frac{1}{2} (-\Omega' + a') \\
 \nu_{34} = \nu_0 + \frac{1}{2} (-\Omega + a) & B_{34} = B_0 + \frac{1}{2} (+\Omega' - a') \\
 \nu_{12} = \nu_0 + \frac{1}{2} (-\Omega - a) & B_{12} = B_0 + \frac{1}{2} (+\Omega' + a')
 \end{array} \tag{3.24}$$

Figure 3.7 depicts these transitions and the energy levels E_1 to E_4 from Equation 3.20 for $B > 0$ (Figure 3.7a), while Figure 3.7b shows the resulting EPR stick spectrum. The transitions are arranged in two doublets centered around B_0 with separation Ω' and splitting a' . The spectral positions g_a and g_b with separation ΔB for the non-interacting spins are also shown (notice $\Omega' \geq \Delta B$). For a thermal population of the energy levels, all four transitions are absorptive as indicated by the blue arrows.

The lower two illustrations (Figure 3.8) show the same SCRP, but with an initial spin polarization with population of the $m_s = 0$ levels. In Figure 3.8a the energy levels $|2\rangle$ and $|3\rangle$ are populated (bold line), while the $m_s = \pm 1$ levels $|1\rangle$ and $|4\rangle$ are unoccupied (dashed line). Accordingly, the transitions from levels $|2\rangle, |3\rangle$ to $|1\rangle$ at B_{13}, B_{12} are in absorption (A – blue), while the transitions to level $|4\rangle$ at B_{24}, B_{34} are in (stimulated) emission (E – red). This is also expressed in the EPR stick spectrum in Figure 3.8b by positive and negative intensities for absorptive (blue) and emissive (red) transitions, respectively. The sequence of transitions on the magnetic field axis is also called the polarization pattern, which is E/A/E/A in this example.

The described scenario with an initial $m_s = 0$ spin polarization has been reported numerous times in literature and is common for light-induced charge transfer reactions. Typical examples are charge transfer complexes in the process of photosynthesis [28] or in organic solar cells [29]. What they have in common is, that the initial excitation is a $m_s = 0$ singlet state. This singlet is subsequently split in a charge transfer reaction into electron and hole. If these do not directly separate further, they can be

described as SCRP. Because of spin conservation, the singlet exciton cannot populate the $m_s = \pm 1$ triplet states directly. The resulting $m_s = 0$ non-Boltzmann population is short-lived and relaxes to a thermal distribution over time, unless the charges separate or recombine beforehand.

Additionally, the signs of J and D can be inferred from the polarization pattern. For a SCRP that results from a singlet precursor and has E/A/E/A polarization $J > 0$ and $D < 0$ [30, 31]. If so, the triplet state $|T_0\rangle$ lies energetically lower than the singlet state $|S\rangle$.

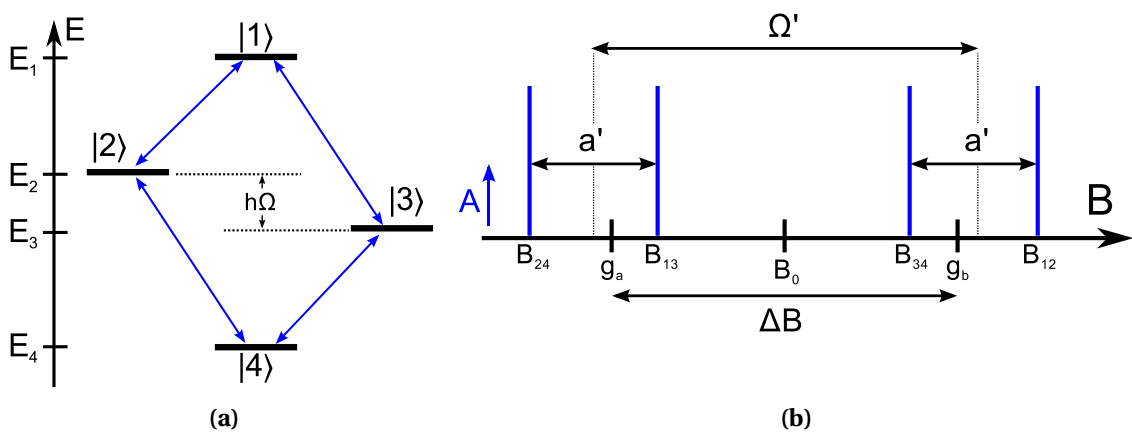


Figure 3.7: (a) Energy levels of a SCRP at magnetic field $B_{\text{ext}} > 0$ together with possible transitions. (b) Resulting EPR stick-spectrum for $\mathbf{B} \parallel \mathbf{z}$, consisting of two doublets with separation Ω' centered around B_0 and with the doublets split by $a' = J' + 2d'$.

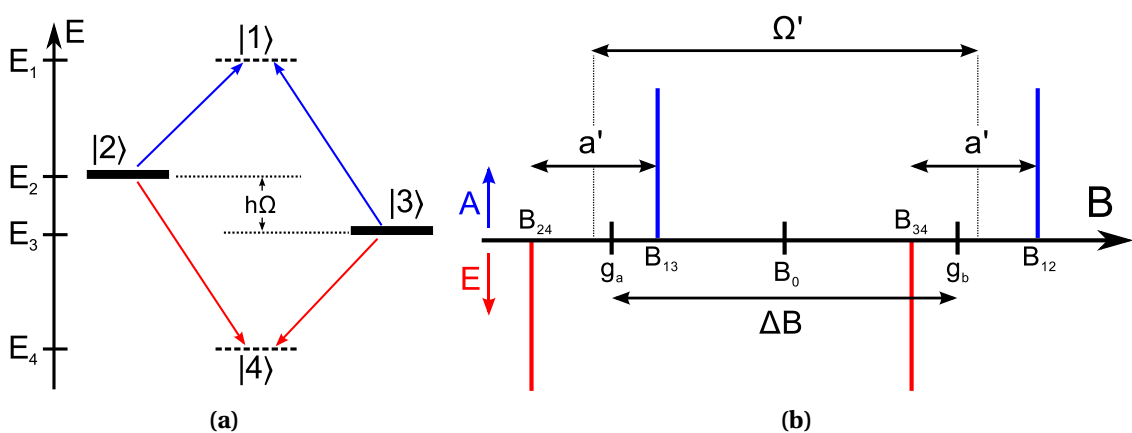


Figure 3.8: The same SCRP, but assuming an initial $m_s = 0$ spin polarization: $|2\rangle$ and $|3\rangle$ populated, $|1\rangle$ and $|4\rangle$ not populated. Transitions are either in absorption (A – blue) or emission (E – red). (b) Resulting EPR stick-spectrum, including microwave absorption and emission. The polarization pattern is E/A/E/A.

3.6 Triplet Excitons

Triplet excitons are quasi-particles with very narrow spatial extent ($r < 1$ nm) and can be described in the *strong coupling regime* $|J - D| \gg \hbar|\nu_a - \nu_b|$. In this case, the mixing angle is $\phi = \pi/4$ (3.19) and the SCRP base $|1\rangle$ – $|4\rangle$ transforms to the singlet triplet base (3.18), in which the Hamiltonian is diagonal. The eigenstates are the triplet states $|T_0\rangle$ and $|T_{\pm 1}\rangle$. The singlet state $|S\rangle$ is also defined, but transitions to or from this eigenstate are first-order forbidden and only possible via ISC. Since $|J - d| \gg \hbar\Delta\nu$, the zero-quantum coherence frequency Ω can be approximated by $\Omega = \frac{1}{\hbar}(J - d)$ and the energy levels are given by:

$$\begin{aligned} |T_{+1}\rangle & E_{T_{+1}} = -\frac{1}{4}J - \frac{1}{2}d + \hbar\nu_0 \\ |T_0\rangle & E_{T_0} = -\frac{1}{4}J + d \\ |T_{-1}\rangle & E_{T_{-1}} = -\frac{1}{4}J - \frac{1}{2}d - \hbar\nu_0 \\ |S\rangle & E_S = +\frac{3}{4}J \end{aligned} \quad (3.25)$$

Because of the small spatial extent of triplets, the point-dipole approximation is not always valid and the rhombicity E needs to be considered. Consequently, d is given in its general form with the angle pair (Θ, φ) setting the orientation of the dipole–dipole tensor \mathbf{D} in the laboratory coordinate system:

$$d = D \left(\cos^2\Theta - \frac{1}{3} \right) + E \sin^2\Theta \cos(2\varphi) \quad (3.26)$$

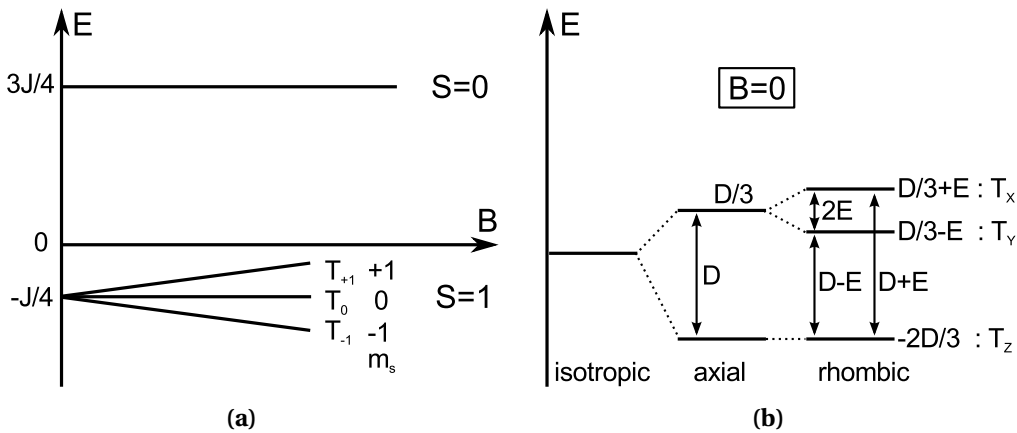


Figure 3.9: (a) Energy levels of a triplet at magnetic field $B_{\text{ext}} > 0$ and (b) zoom on the $S = 1$ levels for $B_{\text{ext}} = 0$. These are degenerate for the isotropic case and further split by D and E for axial and rhombic symmetries.

Figure 3.9 shows the energy levels (3.25) for the singlet and triplet states with separation J . For triplets the exchange interaction is by far larger than the dipolar interaction: $|J| \gg |D|$. The triplet levels $|T_0\rangle$ and $|T_{\pm 1}\rangle$ are referred to as $|T_X\rangle$, $|T_Y\rangle$ and $|T_Z\rangle$ for zero

magnetic field. The coordinate system is then defined by the molecular symmetry axis or the local crystal field. The symmetry of the zero field splitting (Figure 3.9b) reflects the definition of the \mathbf{D} tensor (3.12). Depending on the values of D and E , axial and rhombic symmetries are distinguished.

The transition frequencies and respective magnetic field positions are given in (3.27). They are symmetrically centered around ν_0 (or B_0) with separation $3d$. The values are independent of J , in contrast to the SCRP (3.24).

$$\begin{array}{ll} \underline{B_{\text{ext}} = \text{const.}} & \underline{\nu_{\text{MW}} = \text{const.}} \\ \nu_{+1/0} = \nu_0 - \frac{1}{\hbar} \frac{3}{2} d & B_{+1/0} = B_0 + \frac{3}{2} d' \\ \nu_{0/-1} = \nu_0 + \frac{1}{\hbar} \frac{3}{2} d & B_{0/-1} = B_0 - \frac{3}{2} d' \end{array} \quad (3.27)$$

Figure 3.10 shows the connection of the dipole orientation (3.10a), the spectral position of the resonant transitions (3.10b, top) and the resulting full-field powder spectrum for an unoriented sample (3.10b, bottom). The triplet in this example has axial symmetry ($E = 0$). The spectral positions of the transitions $B_0 \pm \frac{3}{2} d' = D(\frac{3}{2} \cos^2 \Theta - \frac{1}{2})$ for $0^\circ \leq \Theta \leq 90^\circ$ are plotted in 3.10b (top). The resulting powder pattern can be simulated as superposition of the transitions over all possible orientations. The width of the full-field spectrum is $3d' = 2D'$ and is given by the extreme positions of the angular dependence. The distance determination with “the rule of thumb” is again applicable for triplet systems with axial symmetry (see 3.16). Only in this case, the “distance” refers to the approximate spatial extent of the triplet wavefunction.

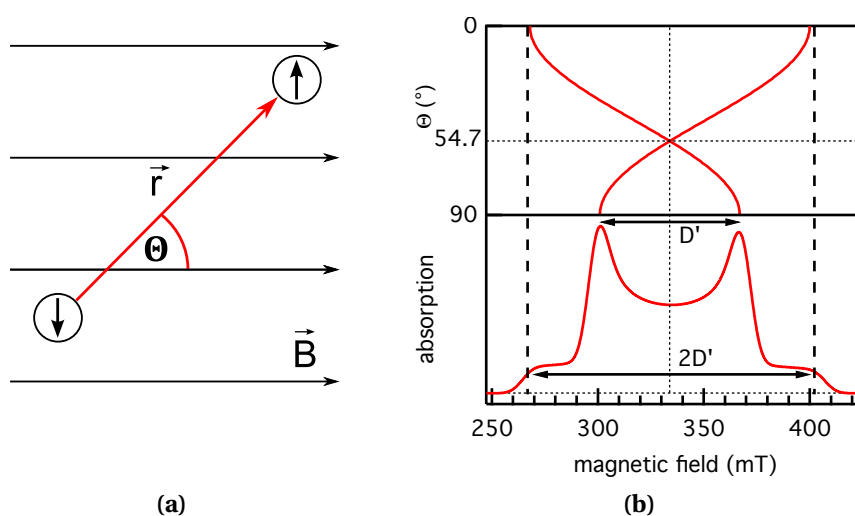


Figure 3.10: (a) Θ is the angle between the vector \vec{r} connecting the two interacting spins and the magnetic field \vec{B}_{ext} . (b) (top) Θ -dependence of the magnetic field splitting. For the “magic angle” of 54.7° the spectrum collapses to a single transition in oriented samples. (bottom) Resulting powder spectrum for an unoriented sample.

3 Electron Paramagnetic Resonance

The “magic angle” of $\Theta = 54.7^\circ$, for which $D(\cos^2\Theta - \frac{1}{3}) = 0$ is noteworthy, as for this orientation the whole triplet spectrum collapses to a single line. This circumstance is used in the field of magic angle spinning spectroscopy.

Figure 3.11 depicts simulations of X-band triplet spectra for different values of D and E . The top row shows the energy levels E_{T_0} and $E_{T_{\pm 1}}$ for $\Theta = 0$ together with the possible transitions (blue arrows). For better comparison with the microwave induced transitions, the splitting is expressed in GHz. The bottom row displays the resulting EPR powder spectra. For axial symmetry ($E = 0$), the spectrum consists of two wide shoulders with separation $2D'$ and two peaks with a gap of D' . If the spin system has rhombic symmetry, both $D, E \neq 0$. The width of the full-field spectrum is still $2D'$, but the two inner peaks now have a splitting of $D' - 3E$ and two additional shoulders appear with separation $D' + 3E'$. All values are absolutes, as the sign of D' and E' has no influence on the spectral shape of the peaks. For $D = 0$ the spectrum collapses to a central broadened peak, which is described in the context of weak coupling in the next section.

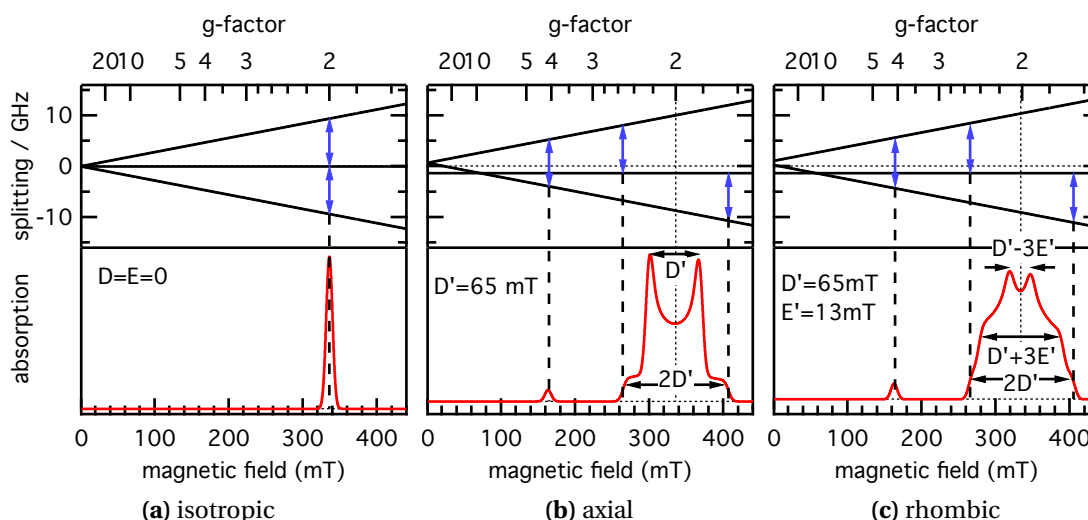


Figure 3.11: Zeeman-splitting in GHz (top) for $\Theta = 0^\circ$ for a $S = 1$ system with varying parameters D and E for (a) isotropic, (b) axial and (c) rhombic symmetry. Possible transitions (blue arrows) and simulated resulting EPR powder spectra (red, bottom). For (b), (c) the half-field transition at $g = 4$ can also be observed. For all simulations $g = 2.0$ and linewidth = 10 mT.

Additionally, there is a peak at $g = 4$ for $D > 0$, called “half-field” transition. It is the single photon, double quantum transition between the two triplet $|T_{\pm 1}\rangle$ states, which is first-order forbidden as $\Delta m_s = \pm 2$. The selection rule for EPR is $\Delta m_s = \pm 1$. However, for distances shorter than ~ 1 nm, the states are mixed and $\Delta m_s = \pm 2$ transitions between $|T_{+1}\rangle$ and $|T_{-1}\rangle$ become slightly allowed.

For EPR experiments with a fixed microwave frequency and sweeping magnetic field, this transition is observed at $g = 4$; i.e. at “half-field” compared to the regular $\Delta m_s = \pm 1$ transitions centered at $g = 2$:

$$\begin{aligned} \underline{B_{\text{ext}} = \text{const.}} \quad \underline{\nu_{\text{MW}} = \text{const.}} \\ \nu_{+1/-1} = 2\nu_0 \quad B_{+1/-1} = \frac{1}{2}B_0 \end{aligned} \quad (3.28)$$

3.7 Polaron Pairs

Polaron pairs can be described in the *weak coupling regime* with $|J - D| \ll h|\nu_a - \nu_b|$. The mixing angle $\phi = 0$ and hence the product base does apply (3.18). The product states $|\uparrow\downarrow\rangle$ and $|\downarrow\uparrow\rangle$ are equal in energy and hence degenerate. Usually $J \approx 0$ can be neglected and the observed spectrum is a very narrow triplet pattern with tiny zero-field splitting. The half-field transition, observed for triplets in the strong coupling regime, is not allowed in the weak coupling regime.

If D is smaller than the linewidth, the situation is best described as asymptotically free spin-1/2 particles with additional dipolar broadening (also see section 3.2.2). For $\Delta\nu > 0$ two transitions at g_a and g_b can be observed for the two spin centers. If $\Delta\nu = 0$ only one broadened central line is observed (see Figure 3.11a, $D = 0$). This situation is the case for the so-called polaron-pair peak at $g = 2$ in ODMR, which is described hereinafter.

3.8 Optically Detected Magnetic Resonance

EPR is usually detected by monitoring the microwave absorption of transitions between the Zeeman sublevels. However in many materials with optical transitions, absorption or emission of a photon in the visible range is dependent on relative spin orientations. The optical process might therefore be influenced by inducing EPR transitions between according spin sub-levels. Monitoring the change in absorption or emission of optical photons by inducing spin-flips with EPR is thus the basis of optically detected magnetic resonance (ODMR). The advantages are: First a boost in sensitivity by several orders of magnitude due to the much easier detection of photons in the visible range than in the microwave regime. Second with ODMR it is possible to study interaction processes, such as triplet-triplet annihilation (TTA), triplet-polaron quenching (TPQ), or ground state depletion (GSD), which usually can not be probed by ordinary EPR methods. The ODMR signal intensity is then recorded as the EPR-induced relative change (e.g. in %) of the optical transition intensity.

For the ODMR results shown in this thesis, TTA and TPQ are the dominant mechanisms, while GSD is not observed for the studied organic semiconductors. This can be shown by the excitation power dependence of the ODMR signal intensity. For TTA and TPQ, the ODMR effect is strongly dependent on the steady state concentration of triplets or charge carriers in the sample. This concentration is a function of the incident illumination intensity, which results in a characteristic dependence of the ODMR signal intensity over the illumination intensity [32]. This is not the case for GSD and the ODMR intensity has a different dependency of the photon flux. These processes are now described in more detail.

Triplet–Triplet Annihilation

In the organic semiconductors studied in this thesis, triplet excitons are a mobile species with long lifetimes. This makes the random encounter of two triplets relatively probable even at low excitation intensities in cw ODMR experiments. The resulting scattering event is depicted in Figure 3.12 and can be described by the formation of an intermediate two-triplet (TT) excited state with quintuplet multiplicity (spin $S = 2$) [33, 34]. This intermediate state can scatter into the singlet state (S_1+S_0), as well as one ($T+S_0$) or two ($T+T$) further diffusing triplets. If the spin configurations of the two initial triplets are independent, the processes will occur with probabilities $1/9$, $3/9$ and $5/9$ for one singlet, one triplet or two triplets, respectively. If the scattering results in a singlet exciton (S_1), it will subsequently most likely emit a photon as delayed fluorescence (DF), or might (with a lower probability) undergo intersystem crossing to the triplet state. By inducing EPR transitions between the triplet and quintuplet spin sublevels, the probabilities of the scattering process can be influenced, which ultimately yields an EPR-induced change of the delayed fluorescence, observable as ODMR [35]. Any triplets escaping the scattering process may participate in this mechanism again, if they don't recombine before that.

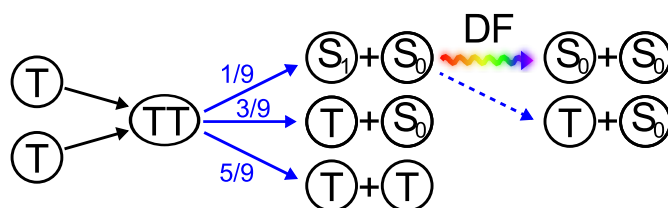


Figure 3.12: Triplet–triplet annihilation of two incoming triplets, resulting in outgoing singlet excitons (S_1), singlet ground states (S_0) and further diffusing triplet excitons. The singlets (S_1) will most probably emit delayed fluorescence (DF).

It has been shown that this process is responsible for the wide triplet ODMR spectra observed for many organic semiconductors [32]. Despite the characteristic dynamics and excitation power dependencies of this two-particle triplet-triplet process, the spectral information contains the symmetry (D, E, Θ, φ) of the triplet wavefunction.

Triplet-Polaron Quenching

Upon the encounter of two independent (e.g. non-geminate) charge carriers or polarons (P^\pm) with opposite charge, they can form a loosely-bound electron-hole pair (P^+P^-), that succeedingly recombines (see Figure 3.13a). This pair can be either in singlet or triplet spin state, depending on the initial spin orientation of the charges. Since the multiplicity of triplets is 3 (T_{+1}, T_0, T_{-1}) and 1 for singlets (S_1), the probability for their formation is $3/4$ and $1/4$, respectively. If the two polarons are separated relatively far, spin-spin interactions D and J can be considered to be negligible. This means, that the T_0 triplet state is in resonance with the singlet state S_1 , facilitating intersystem crossing (ISC). Because the luminescing singlet excitons are short lived, this opens a shortcut for the recombination of T_0 triplets, depleting this population. If by means of EPR, transitions from the triplet $T_{\pm 1}$ levels to the T_0 level are induced (see also Figure 3.11a), this would lead to an increase in radiative recombination, observable by means of ODMR.

The described effect is being discussed to be responsible for the narrow resonance at $g = 2$, observed for many organic semiconductors [32, 36]. This spectral feature is then often referred to as polaron-pair peak.

Ground State Depletion

Optical excitation of an organic semiconductor usually creates singlet excitons. These do either recombine radiatively (PL) during the singlet lifetime ($\sim ns$), or they can undergo intersystem crossing to triplet excitons, as shown in Figure 3.13b.

Lets consider a single molecule. This molecule can be either in the ground state, singlet or triplet excited state. The μs long triplet lifetime is several orders of magnitude longer than the singlet lifetime. Hence in a steady state experiment it is most likely, that the molecule is either in the ground state or triplet excited state. If the latter is the case, the molecule cannot participate in the singlet excitation / PL cycle. Consequently the situation can be described as ground state depletion.

There are three rates (k_{pop}) involved for the population of triplets in their spin sub-levels T_0 and $T_{\pm 1}$ from a singlet precursor, as well as additional three recombination rates from the triplet excited state back to the ground state. All of these rates can be

3 Electron Paramagnetic Resonance

considered to be at least slightly different. The T_0 triplet level has the highest wave-function overlap with the singlet regime and therefore usually the highest recombination rate. When EPR transitions between the Zeeman sublevels are induced (see also Figure 3.11), the steady state balance of the involved rate equations is changed, which will result in a change of the overall triplet recombination rate. This is equal to a change of the triplet lifetime, and will result in a relative change of the ground state repopulation rate, which in turn is connected to the singlet PL intensity.

While this process is not the dominant mechanism for the ODMR effect in the studied materials systems of this thesis, very similar processes are for example observed for nitrogen-vacancy (NV) defects in diamond [37, 38] or silicon-vacancies in silicon carbide [39].

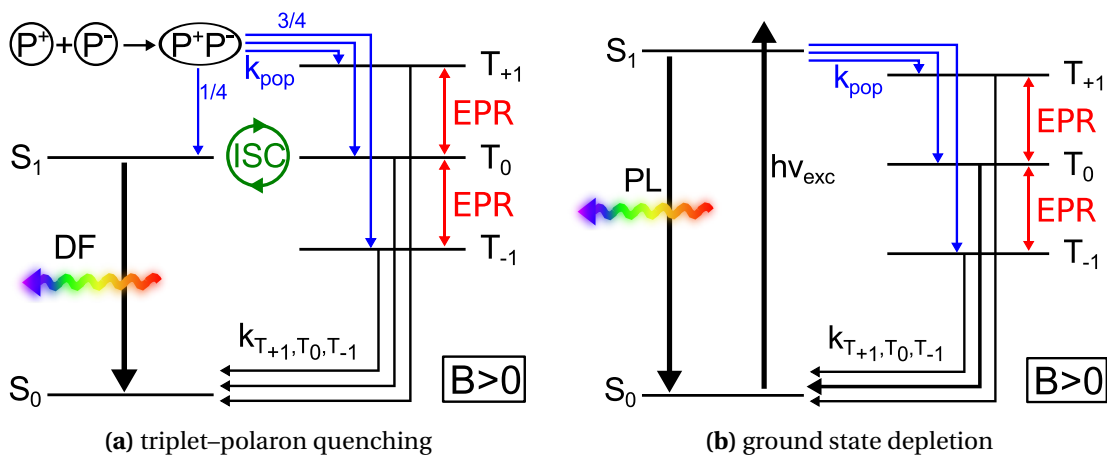


Figure 3.13: (a) Triplet-polaron quenching after the encounter of two polarons (P^\pm) forming a polaron pair (P^+P^-), which is either in singlet or triplet configuration. By inducing spin-flips in the triplet manifold, a shortcut for triplet recombination via ISC from T_0 to the singlet state S_1 and subsequent delayed fluorescence (DF) can be opened. (b) Ground state depletion occurs, when a relevant amount of the involved optically active material is populated with long-living triplet states, and consequently does not participate in the cycle of optical excitation and emission of PL. Since the triplet sublevels have different recombination rates k , spin flips induced by EPR, yield ground state repopulation and increase in PL.

4 Experimental Section

This Chapter will give a short introduction to sample preparation, the used EPR setups with extensions for optical (ODMR) and time-resolved detection (trEPR), as well as the all-optical methods photoluminescence (PL) and photo-induced absorption (PIA).

4.1 Sample Preparation

Sample preparation took place inside a nitrogen glovebox to avoid exposure to air. The organic materials were dissolved in chlorobenzene or ortho-dichlorobenzene at a concentration of 10–20 mg/ml. Magnetic steering over several hours ensured complete dissolution. For blends, the separate solutions of the different compounds were then mixed according to the desired blending ratio (e.g. 1:1 for most polymer:fullerene blends). For EPR ~0.1 ml solution were poured into 4 mm quartz EPR sample tubes and the solvent was evaporated under rough vacuum (final pressure $\sim 10^{-2}$ mbar), yielding a thick film on the inner sample tube wall. The sample tubes were finally sealed under vacuum with a blow torch. For optical measurements, thin films of ~100 nm were spin-cast onto sapphire substrates for use in PIA, PL and absorption. After deposition, most samples were annealed for ~10 minutes at ~130°C. The materials and resulting samples were at all time kept under dry nitrogen atmosphere or vacuum to avoid degradation due to exposure to oxygen or moisture.

4.2 The X-Band EPR Spectrometer

The used EPR spectrometer is a home-modified Bruker 200D X-Band spectrometer. Figure 4.1 gives an overview of the setup. It is outfitted with an optical transmission cavity (ER4104OR) with a loaded resonance frequency of 9.432 GHz, which results in a resonance magnetic field of 335 mT for $g = 2.0$. The magnetic field is calibrated for every measurement with a high-precision NMR (nuclear magnetic resonance) gaussmeter Bruker ER035. The frequency counter EIP28b handles readout of the NMR and microwave frequencies and thus ensures proper automated g -factor calibration. The microwave bridge ER047 with a maximum power output of 200 mW is specially equipped

4 Experimental Section

with an integrated, fast 100 MHz amplifier to allow for trEPR operation. A field-frequency lock ER033 can be used when long transient measurements are recorded to keep a set g -factor position stable for hours. The sample is placed in a helium-flow cryostat (Oxford Instruments ESR900), which has an accessible temperature range of (3.6–300) K. The temperature is controlled by a Lakeshore 330 temperature controller to enable stable operation at about ± 10 mK of the desired value. All components are controlled by a computer, running self-written Labview software that also handles the data processing.

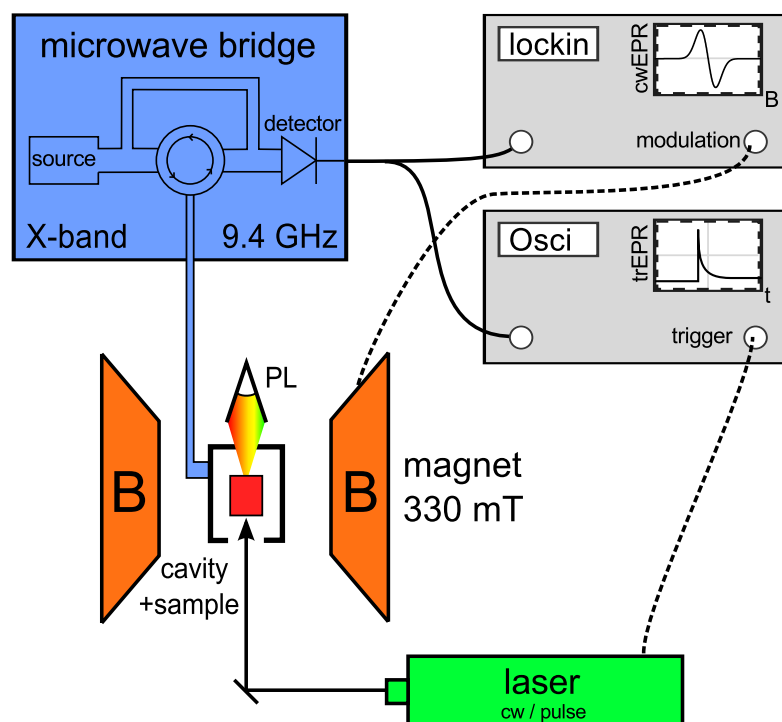


Figure 4.1: Overview of the EPR setup in configuration for cwEPR and trEPR detection, using either a lock-in amplifier or an oscilloscope for signal recording.

Several illumination sources are available to be used with the spectrometer. White light is provided by a halogen bulb lamp with a flexible fiber light guide, connected to the cavity. The infrared part of the halogen bulb spectrum is blocked by an IR filter. Continuous wave lasers include blue (405 nm), red (650 nm) and infrared (785 nm) diode lasers and a green (532 nm) DPSS laser, all with output powers in the range of 100 mW. For trEPR, a pulsed NdYAG laser with 532 nm frequency doubler is available. The pulse length for this laser is approximately 10 ns and the energy is ≈ 1 mJ per pulse.

A silicon photo diode can be mounted at the rear optical cavity access. Its output is used for ODMR detection or for recording the PL intensity. The light is filtered by optical long-pass filters to e.g. block the transmitted laser light, while letting the PL pass to the detector.

g-Factor Calibration

A major advantage of this EPR setup is the very precise g -factor calibration, due to the integrated NMR gaussmeter and a microwave frequency counter. With this equipment, it is possible to calibrate the spectrometer even without special samples like DPPH or Mn^{2+} . According to the EPR resonance condition (3.4), the measurement g -factor is $g_M = \frac{h\nu_{\text{MW}}}{\mu_B B_{\text{ext}}}$. The external magnetic field B_{ext} can be measured precisely by determining the proton Larmor frequency ν_{NMR} from the NMR gaussmeter. With this $B_{\text{ext}} = \frac{2\pi\nu_{\text{NMR}}}{\gamma'_p}$, with γ'_p being the shielded proton gyromagnetic ratio for protons in water or similar media. The measurement g -factor can then be written as:

$$g_M = \frac{\hbar\gamma'_p}{\mu_B} \frac{\nu_{\text{MW}}}{\nu_{\text{NMR}}} = g_e \frac{\gamma'_p}{\gamma_e} \frac{\nu_{\text{MW}}}{\nu_{\text{NMR}}} \quad (4.1)$$

The ratio $\frac{\hbar\gamma'_p}{\mu_B}$ can be expressed as the ratio of the proton and electron gyromagnetic ratios $\frac{\gamma'_p}{\gamma_e}$ times the free electron g -factor g_e . The measurement of the microwave to NMR frequency ratio is therefore sufficient for the calibration. The achievable relative g -factor uncertainty is in the order of $1 \cdot 10^{-5}$, limited by the electromagnet.

4.2.1 Continuous Wave EPR

For operation in cwEPR mode, the main magnetic field is superimposed with an alternating minor field, generated by additional modulation coils. These are mounted inside the walls of the microwave cavity. The 100 kHz sinusoidal modulation is applied with a typical amplitude in the range of 0.02 mT to 0.5 mT. The signal output of the microwave bridge is connected to a lock-in amplifier (Ametek 7265 or Stanford Research SR850), referenced by the modulation frequency for phase-sensitive detection. Due to the magnetic field modulation, cwEPR spectra are recorded in first derivative of the absorption. The signal reconstruction is depicted schematically in Figure 4.2.

The reason for using lock-in detection is the vast improvement in signal-to-noise ratio. Non-resonant background, as well as distortions at frequencies other than the modulation frequency are suppressed. The downside is the lack of time resolution. The lowpass frequency filter limits the available time resolution to roughly 0.1 s.

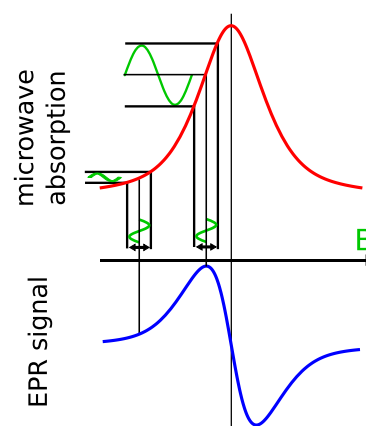


Figure 4.2: The EPR signal (blue) is recorded as 1st derivative of the microwave absorption (red) by modulating the static magnetic field (green) in a lock-in detection scheme.

4.2.2 Time-Resolved EPR

For trEPR operation, the microwave absorption is recorded directly with an oscilloscope, hence without field modulation and lock-in amplifier. Another notation used in literature is DDEPR (direct-detected), referring to the same method. The transient response of the spin system is recorded after a light pulse or similar initialization. This starts a (chemical) reaction or initiates a charge transfer that produces EPR-active excited species. Usually these are short-lived or even have changing EPR properties over time. The realization within the EPR setup is shown in Figure 4.1. The system is triggered by a laser pulse and the microwave bridge signal output is connected to a digital oscilloscope (Tektronix DPO3054). In-between, the signal is amplified by a high-pass Femto DLPCA amplifier to boost the signal amplitude and get rid of low-frequency distortions. The time resolution is determined by the Q-factor of the microwave cavity. A high Q-factor does provide excellent sensitivity improvement for cwEPR, however for trEPR the time resolution is limited by it. The cavity response time is given by:

$$\tau_{\text{cavity}} = \frac{Q}{\pi\nu_{\text{MW}}} \quad (4.2)$$

With $Q = 3400$ and $\nu_{\text{MW}} = 9.432$ GHz, the cavity response time is $\tau_{\text{cavity}} = 115$ ns.

Considerable effort is necessary for the data processing of the raw oscilloscope transients. For most samples studied with trEPR, there is a strong background signal, that is independent of the applied magnetic field. This signal is caused by laser-induced conductivity changes and is subject of the method of time-resolved microwave conductivity (TRMC). The standing microwave field inside the EPR cavity has residual electric field strength at the sample position. When the sample is excited by the laser flash, its conductivity changes due to the charge transfer reactions. This change in conductivity is then detected as a non-resonant microwave absorption, that is independent of the magnetic field. The EPR induced microwave absorption at the resonant magnetic field is superimposed with that background. By recording transients at off-resonance magnetic field values, the background can then be subtracted from the on-resonance measurements. Usually a step-wise sweep over the interesting magnetic field range is performed and transients are recorded for each step.

The raw data recorded by the oscilloscope is on a linear time axis with e.g. 1 million evenly spaced data points. For data-reduction and better handling the transient data is interpolated to resemble a logarithmic time axis. This also increases the signal-to-noise ratio especially for long delay times. Next, the data set is transferred to a matrix (B-field vs. logarithmic time) for further processing. Slices at different times or magnetic field values can then be used for plotting and fitting.

4.2.3 Optically Detected Magnetic Resonance

For operation in ODMR mode, the setup is driven by a Wiltron 69137A frequency synthesizer as microwave source (see Figure 4.3). This modification is necessary, because the output power of the Bruker microwave bridge cannot be modulated. To enable lock-in detection, the synthesizer is square-wave modulated (on/off) in the kHz-range. The output is then amplified by a 2 W Microsemi solid-state microwave amplifier and directed by a circulator to the cavity. The other output of the circulator is connected to a microwave detector diode for tuning the resonance frequency by minimizing the cavity reflection.

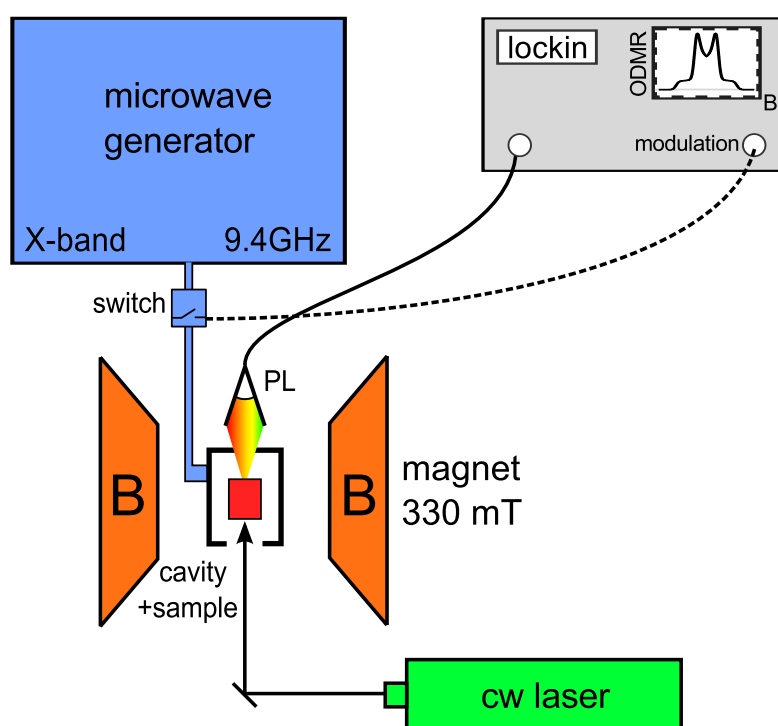


Figure 4.3: Overview of the EPR setup in ODMR configuration using a chopped microwave generator, a silicon diode for PL detection and a lock-in amplifier for signal recording.

The optical excitation is done using a stabilized cw laser and the PL is collected by a Si-diode behind a long-pass filter to block the laser light. A Femto DLPCA transimpedance amplifier is interposed between the PL detector and the Ametek 7265 lock-in amplifier. The ODMR signal is then the EPR-induced change in PL intensity, in relation to the undisturbed PL intensity $\Delta PL/PL$ and can be expressed in % PL-change. It is thus also referred to as PLDMR.

4 Experimental Section

The real challenge for ODMR is to eliminate all sources of noise and instability. This includes the control of an extremely constant helium flow, because the changes in optical density of the cold helium gas that passes the cavity, adds noise to the transmitted laser and PL light. Temperature drifts and instabilities over time (temperature noise), as well as fluctuating laser output power and noise result in signal distortions. Additionally, the optimal modulation frequency is different for every observed excited species and the frequency dependence of the signal-to-noise ratio is usually rather irrational.

4.3 Photo-Induced Absorption – PIA

For PIA, sapphire substrates are used, because of their transparency in the near-infrared. The substrates are coated in a spin coater and then mounted in a cold finger cryostat (5–300 K). For PL and PIA measurements, excitation is achieved by a 532 nm laser. The output power is set to ~30 mW after mechanical chopping. Additional cw illumination is provided by a halogen lamp. Both beams are superimposed on the sample. The transmitted light is collected by large diameter concave mirrors and focused into a Cornerstone monochromator. Depending on the wavelength, the detection is provided by a silicon photodiode (550–1030 nm), or by a liquid nitrogen cooled InSb-detector (1030–5500 nm). Therefore, a broad energy range of 0.23–2.25 eV is accessible (restricted by KBr cryostat windows). The detectors are coupled to the monochromator and signals are recorded using an Ametek 7265 lock-in amplifier referenced by the chopper. The chopping frequency is 330 Hz for spectral studies, low enough to see most of the signal and high enough to gain a good signal-to-noise ratio. The phase is set to zero under PL conditions, because the extremely short lifetime of fluorescing species prevents lifetime related phase shifts and compensates the phase shift caused by the measuring system alone.

The PIA-experiment consists of three measurements: PIAPL, PL and transmission. Figure 4.4 shows exemplary spectra. PIAPL is measured having both pump (laser) and probe lights on, where the laser beam is modulated with a mechanical chopper. PL is measured when only the laser is on and modulated. Transmission is measured by turning the laser off and modulating the halogen lamp. The PIA spectrum is then calculated using the following formula:

$$\text{PIA} = \frac{-\Delta T}{T} = \frac{\text{PIAPL} - \text{PL}}{\text{Transmission}} \quad (4.3)$$

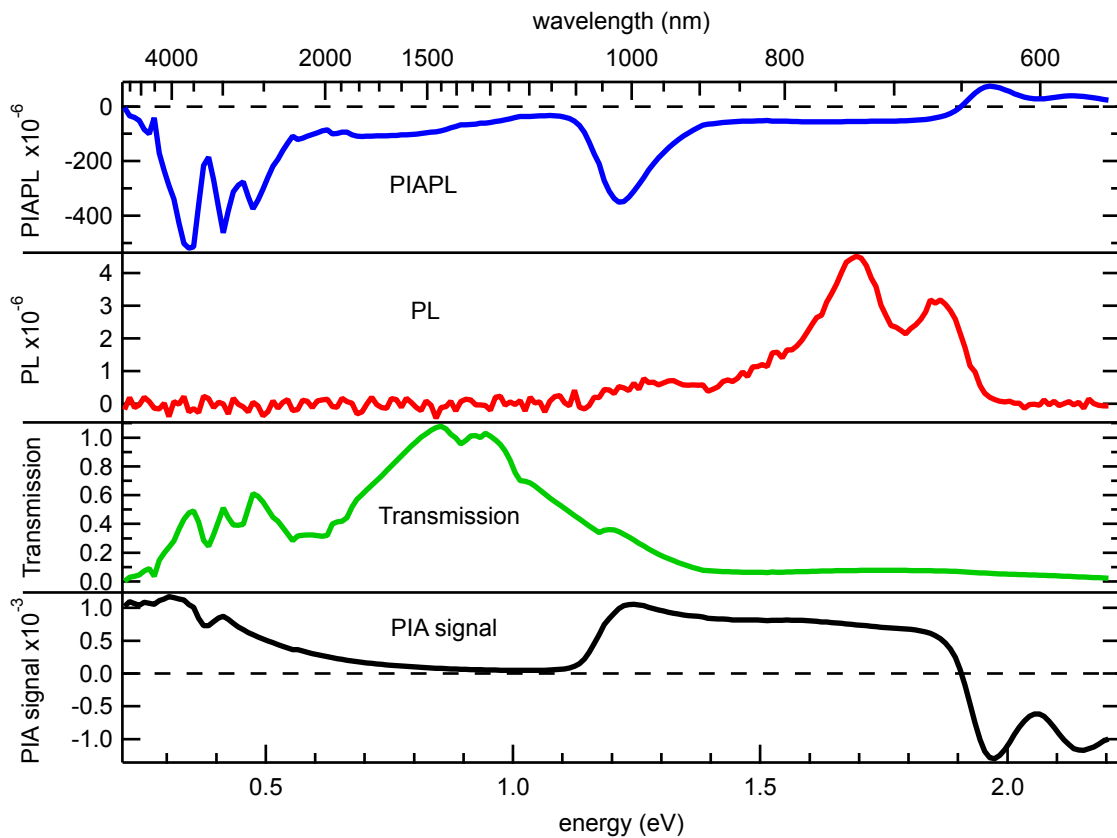


Figure 4.4: P3HT:PCBM blend at 30 K. The three necessary measurements for PIA are: PIAPL, PL and Transmission. The PIA signal is then calculated using Equation 4.3.

For photoluminescence measurements the same setup and samples as for PIA can be used. The resulting PL-spectra shown in this thesis were corrected for the spectral response of the spectrometer. For this it is necessary to have the spectral transmission of the used monochromator gratings and the sensitivity of the silicon detector diode. These curves are multiplied to calculate a wavelength dependent calibration coefficient. The recorded PL-spectra are then divided by this coefficient to gain absolute values.

Absorption

Absorption is measured with a Perkin-Elmer Lambda 900 spectrometer under ambient conditions, i.e. at room temperature in environmental air. The same sapphire substrates as for PIA and PL measurements can be used. The accessible wavelength range is 250–2500 nm, roughly equal to 5.0–0.5 eV.

5 Results

5.1 Spectroscopic Signatures of Photo-Generated C_{70} -Fullerene Radical Anions

Abstract

Photoinduced polarons in films of polymer:fullerene blends were studied by photoluminescence (PL), photoinduced absorption (PIA) and electron paramagnetic resonance (EPR). The donor materials used were P3HT and MEH-PPV. As acceptors we employed $PC_{60}BM$ as reference and various soluble C_{70} -derivatives: $PC_{70}BM$, two different diphenyl-methano-[70]fullerene oligoether (C_{70} -DPM-OE) and two dimers, C_{70} - C_{70} and C_{60} - C_{70} . Blend films containing C_{70} revealed characteristic spectroscopic signatures not detected for C_{60} . With EPR, the first experimental identification of the negative polaron (P^-) localized on the C_{70} -cage in polymer:fullerene BHJs has been obtained. When recorded with conventional X-band EPR, this signal is overlapping with the signal of the positive polaron (P^+), which does not allow for its direct experimental identification. Owing to the superior spectral resolution of high frequency D-band EPR, we were able to separate light-induced signals from P^+ and P^- in P3HT: C_{70} BHJs. Comparing signals from C_{70} -derivatives with different side-chains, we have obtained experimental proof that the polaron is localized on the cage of the C_{70} molecule. The formation of C_{70} radical anions also leads to a sub-gap PIA band at 0.92 eV, hidden in the spectra of C_{70} -based blends. These spectral features allow for more directed studies of charge separated states in conjugated polymer: C_{70} blends.

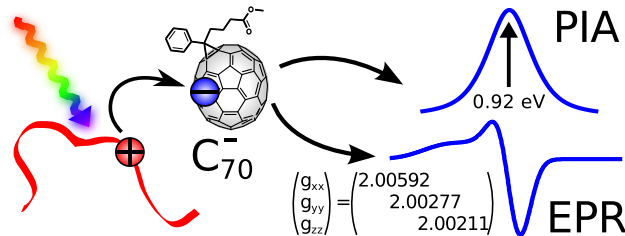


Figure 5.1: After light-induced charge transfer from a polymer (red ribbon), C_{70} -fullerene anions show typical spectral features in PIA and EPR.

5.1.1 Introduction

The soluble fullerene derivative PC₆₀BM is used as acceptor material in the vast majority of the OSC devices reported. One of the downsides of the PC₆₀BM acceptor material for photovoltaic applications is a very low absorption coefficient in the visible spectral region and, as a consequence, a relatively small contribution to the photocurrent. It was outperformed recently by PC₇₀BM, due to its higher absorption coefficient in the visible part of the solar spectrum (see Figure 5.2), but also due to the slightly higher open circuit voltage [10, 40, 41]. Although understanding of the elementary steps of efficient charge separation in the photovoltaic materials is a prerequisite for improving the efficiency, the photophysics of C₇₀ containing blends is much less investigated than of its C₆₀ relatives.

So far EPR and VIS-NIR spectra of C₇₀ derivatives obtained in different phases like crystallites, salt-like samples and dilute (frozen) solutions in (un)polar solvents were presented in the literature [42, 43, 44, 45]. The resulting signals differ for each different phase, due to interactions with the host material. therefore, from the EPR measurements, the undisturbed *g*-tensor components of the C₇₀ radical anion could not be obtained [46]. Additionally several partly overlapping NIR-absorption bands of single and multiply charged C₇₀ anions and cations obtained by reduction using potassium in tetrahydrofuran solution were detected. An absorption at 1370 nm (0.905 eV) was tentatively assigned to solvation complexes of C₇₀ radical anions in solution [42, 44].

Recently, new C₇₀-based fullerene dimers were introduced showing additional PIA and EPR features when blended with conjugated polymers in thin solid films [15]. Here, we report the first detailed characterization of the polaron states (radical anion and cation) in C₇₀-based polymer:fullerene heterojunctions by high frequency (HF 130 GHz) EPR. Having high spectral resolution, the HFEPR allows for the identification of the spectra of the positive polaron localized on the polymer and the negative one on the fullerene cage. The EPR spectra of the polymer:C₇₀-fullerene blends studied with the conventional X-band (9.5 GHz) technique were found to be significantly different from those of polymer:PC₆₀BM and poorly resolved, which makes the direct identification of the involved species speculative. To clarify this issue, we have carried out a comparative high and low frequency EPR study of polymer:fullerene composites. We generalize these findings for a broader class of C₇₀-fullerene derivatives in solid state and present results of the sub-gap PIA, determining the excitation energies of the involved excited state.

5.1.2 Experimental Details

Samples

The polymers P3HT and MEH-PPV as well as the fullerenes PC₆₀BM and PC₇₀BM were used as purchased. Details about the synthesis of the fullerene dimers C₇₀-C₇₀ and C₆₀-C₇₀ as well as C₇₀-DPM-OE are reported elsewhere [15]. Further details about the materials are given in Chapter 2.4. The materials and resulting samples were (at all time) kept under dry nitrogen atmosphere or vacuum to avoid oxidation. Samples were processed from chlorobenzene solutions (10–20 mg/ml) with a 1:1 weight ratio for blends. Thin films of ~100 nm were spincoated onto sapphire substrates for use in PIA, PL and absorption. For X-band EPR, ~0.1 ml solution were poured into quartz EPR sample tubes and the solvent was evaporated under rough vacuum (final pressure ~10⁻² mbar), yielding a thick film on the inner sample tube wall. The sample tubes were finally sealed under vacuum with a blow torch. Samples for D-band EPR were prepared inside thin EPR capillaries by drying the sample solution in the N₂ atmosphere and additional pumping of the samples for 48 h to remove the rest of the solvent. After deposition, all samples were annealed for ~10 minutes at ~130 °C.

Optical Measurements

Photoinduced absorption (PIA) and optical absorption of thin films on sapphire substrates were recorded according to Chapter 4. PL spectra were measured with the same setup as used for PIA.

EPR

X-band EPR spectra were recorded according to the description given in Chapter 4. Illumination was provided by a 532 nm DPSS laser. Calibration of *g*-factors were carried out according to Chapter 4.2.

High frequency EPR measurements were performed on a pulsed high frequency D-band spectrometer (130 GHz/4.6 T) equipped with a single mode cylindrical cavity TE₀₁₁ [47]. EPR spectra of the composites were recorded in the pulse mode in order to get rid of the microwave phase distortion due to fast-passage effects. The absorption line shape of the EPR spectra was recorded by monitoring the electron spin echo (ESE) intensity from a two microwave pulse sequence as a function of magnetic field. The duration of the $\pi/2$ microwave pulse was 40–60 ns, and typical separation times between microwave pulses were 150–300 ns. The differential line shapes of the spectra were obtained by numerical differentiation.

5 Results

Light excitation of the sample was achieved with an optical parametric oscillator (Opotek) pumped by a Nd:YAG laser (Quantel), the output of which was coupled to an optical fiber. The optical fiber allows delivery of up to 2 mJ per pulse to the sample. The excitation wavelength was 532 nm.

For the simulation of the EPR lineshapes and g -tensor determination (X-band and D-band), the software package EasySpin was used [48]. Spectra were fitted to the D-band experimental data and the gained data set of g -tensors and strains was used to reproduce the X-band data.

5.1.3 Results

Absorption and Photoluminescence

Figure 5.2 shows that PC₇₀BM has an increased absorption in the range of 400–700 nm compared to PC₆₀BM, which is favorable in view of the AM 1.5 solar flux. Absorption was measured under ambient conditions. At low temperatures (12 K) these samples emitted a weak, yet detectable PL when excited by a 532 nm laser.

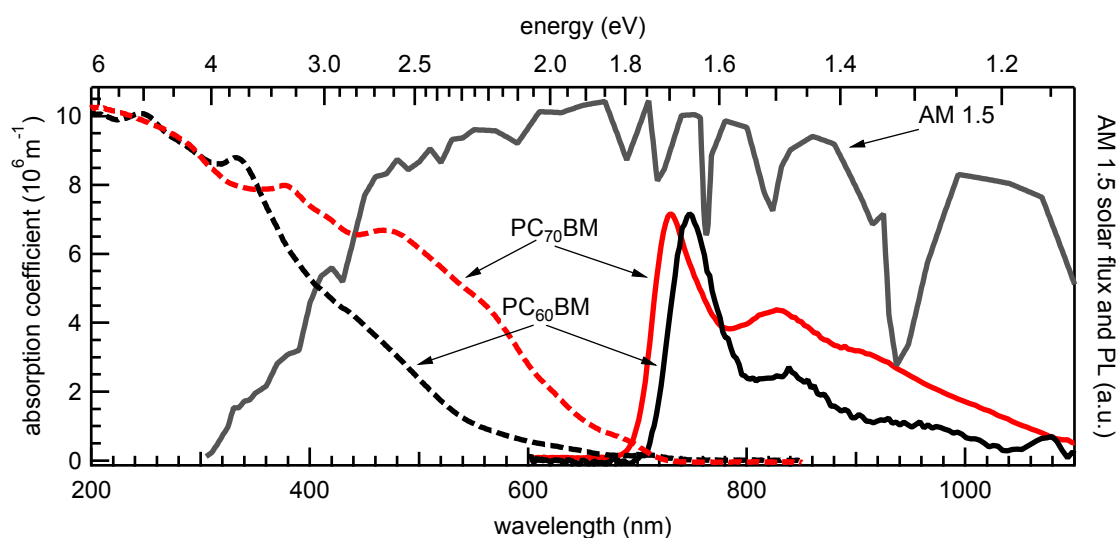


Figure 5.2: Normalized AM 1.5 solar flux (grey line), absorption at 300 K (dashed) and normalized PL at 12 K (solid) of thin films of PC₆₀BM (black) and PC₇₀BM (red).

Intensities of the PL spectra were corrected for the spectral response of the spectrometer (see Chapter 4.3). The spectra of both fullerene derivatives showed well resolved vibronic structures and the PL of PC₇₀BM was blue-shifted by ~ 40 meV (17 nm), matching literature values [49].

PIA

We studied the photophysical properties by photoinduced absorption (PIA). The excitation by a 532 nm laser leads to singlet excitons, which are separated at the polymer:fullerene interface yielding positive and negative polarons in the polymer and the fullerene phase, respectively. The resulting change in transmission ($-\Delta T/T$) of a white light continuum probe beam was measured (see Chapter 4.3). In most polymer:fullerene blends, transitions ascribed to polaronic states (radical cations) are located at 0.3 eV and 1.2 eV. For P3HT or PPV blended with $PC_{60}BM$ these spectral signatures are well documented [50, 51].

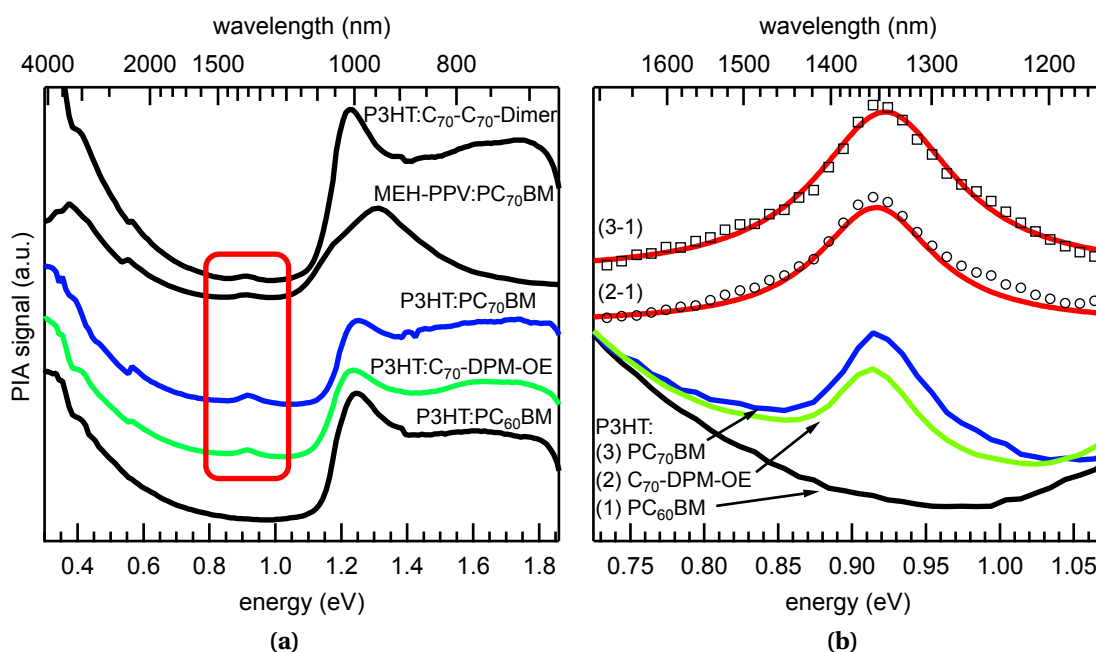


Figure 5.3: (a) PIA spectra at 30 K. While the structure of the spectra is similar, the peak at 0.92 eV only shows up in blends with C_{70} -derivatives. (b) Zoom on the 0.92 eV region for normalized spectra of P3HT: $PC_{60}BM$ (1), P3HT: C_{70} -DPM-OE (2) and P3HT: $PC_{70}BM$ (3). Additionally shown are subtractions of the spectra (2-1) and (3-1) together with Lorentzian fits of the lineshape (red).

Figure 5.3a shows the PIA spectra of the measured polymer:fullerene blend systems at 30 K. All spectra contain the two transitions at 0.3 eV and 1.2 eV, due to the positive polaron created on the polymer, shifting slightly according to the varying energy levels of the different polymers. Additionally we found an absorption at 0.92 eV in all C_{70} -containing blends, which is absent in the reference P3HT: $PC_{60}BM$ spectrum and therefore related to the C_{70} . We were able to separate the contribution of the underlying peak (see Figure 5.3b) by subtracting the normalized spectrum of P3HT: $PC_{60}BM$ (1) from P3HT: C_{70} -DPM-OE (2) and P3HT: $PC_{70}BM$ (3).

5 Results

Lorentzian fits of the resulting spectra (3-1) and (2-1) and the other materials investigated yield the parameters shown in Table 5.1. The observed slight differences could stem from systematic errors in the PIA measurement process, but are more likely a result of variations of the 0.92 eV absorption depending on the molecular environment of the excited state.

Table 5.1: Peak energy E_0 and linewidth FWHM of the observed C_{70} anion peaks.

Material	T (K)	E_0 (nm)	E_0 (eV)	FWHM (eV)
P3HT: C_{70} - C_{70} -dimer	30	1355	0.915	0.081
P3HT: C_{70} -DPM-OE	30	1352	0.917	0.095
P3HT:PC ₇₀ BM	30	1343	0.923	0.112
MEH-PPV:PC ₇₀ BM	30	1361	0.911	0.075
MEH-PPV:PC ₇₀ BM	120	1367	0.907	0.090

Average values: $E_0 = (1356 \pm 9)$ nm \equiv (0.915 ± 0.006) eV. FWHM = (0.091 ± 0.014) eV

As the examined fullerene derivatives have different side-chains, we can exclude them to account for the observed absorption band. Charge transfer complexes as possible candidates for an additional sub-gap absorption could be ruled out by replacing the polymer P3HT with MEH-PPV, which has different HOMO and LUMO energies [52, 53].

Furthermore the relation of the 0.92 eV peak to C_{70} -derivatives is also consistent with the different temperature dependence of the PIA peaks in the blend of MEH-PPV:PC₇₀BM (Figure 5.4). The polaron peaks at 0.3 eV and 1.2 eV both show an identical decrease in signal intensity when increasing the temperature from 30 K to 300 K, while the 0.92 eV peak decreases steeper and vanishes at 300 K. The intensity of the 0.92 eV peak has been determined by subtracting the background at this spectral position and integrating the peak.

In the polymer:PC₆₀BM blends, the signature of the C_{60} anion radical peak is an interesting issue. It is missing in the MEH-PPV or P3HT based PC₆₀BM blends. As discussed in literature [54], this may be due to the fact that the C_{60} anion peak is at 1.24 eV and therefore superimposed by the stronger polymer polaron signal located at the same energy. We do observe an additional C_{60} radical anion PIA peak in blends of PC₆₀BM and the novel low band-gap polymer PTDBT, confirming the results of Ref. [54].

The positive polymer polaron is well known to show the characteristic 1.2 eV and 0.3 eV signatures, but does not explain the feature at 0.92 eV. According to our findings, we associate this new feature to the negative radical anion on the C_{70} -fullerene, formed in the course of photoinduced electron transfer from donor to acceptor.

5.1 Spectroscopic Signatures of Photo-Generated C_{70} -Fullerene Radical Anions

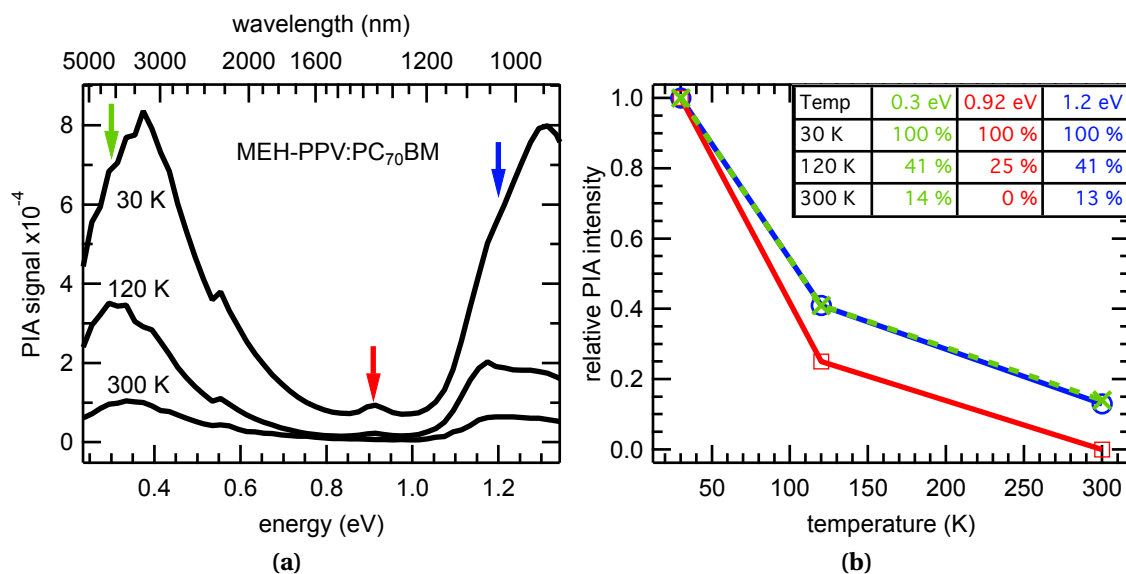


Figure 5.4: (a) Temperature-dependent PIA spectra for MEH-PPV:PC₇₀BM. (b) The main polaronic peaks at 0.3 and 1.2 eV show identical behavior. In contrast, the peak at 0.92 eV decreases steeper when increasing the temperature.

EPR

Prior to illumination, no EPR signals in the blends were observed. Under illumination at temperatures below 150 K, the X-band spectra of the composites containing C_{60} -derivatives show two distinct polaron signals (see Figure 5.5a (1)). These signals were previously assigned to photogenerated positive and negative polarons in the blends: P^+ localized on the polymer around $g = 2.002$ and P^- on the C_{60} -cage at $g = 2.000$ [55, 56, 57, 58]. At lower temperatures, however, part of the signal remains persistent after switching off the excitation, as shown in Figure 5.5a (2) and can be eliminated only by warming up the sample [57, 59]. This behavior is consistent with deeply trapped charge carriers [60, 61].

Remarkably, X-band spectra of C_{70} -based blends do not demonstrate any such signal around $g = 2.000$ (Figure 5.5b). Instead, only one signal around $g = 2.002$, corresponding to the P^+ (radical cation) on a P3HT chain can be seen. It is slightly broadened and reveals a shoulder at $g \geq 2.005$. We assume that the appearance of this shoulder is related to the negative polaron P^- localized on the C_{70} fullerene as it is observed for all blends containing C_{70} -derivatives (indicated by the red rectangle in Figure 5.5b) and absent in blends containing only C_{60} .

In order to deconvolute strongly overlapping signals, the “light on – light off” method can be applied. In general, the EPR spectral intensity is proportional to the number of spins in the sample, which is in turn dependent on the illumination intensity.

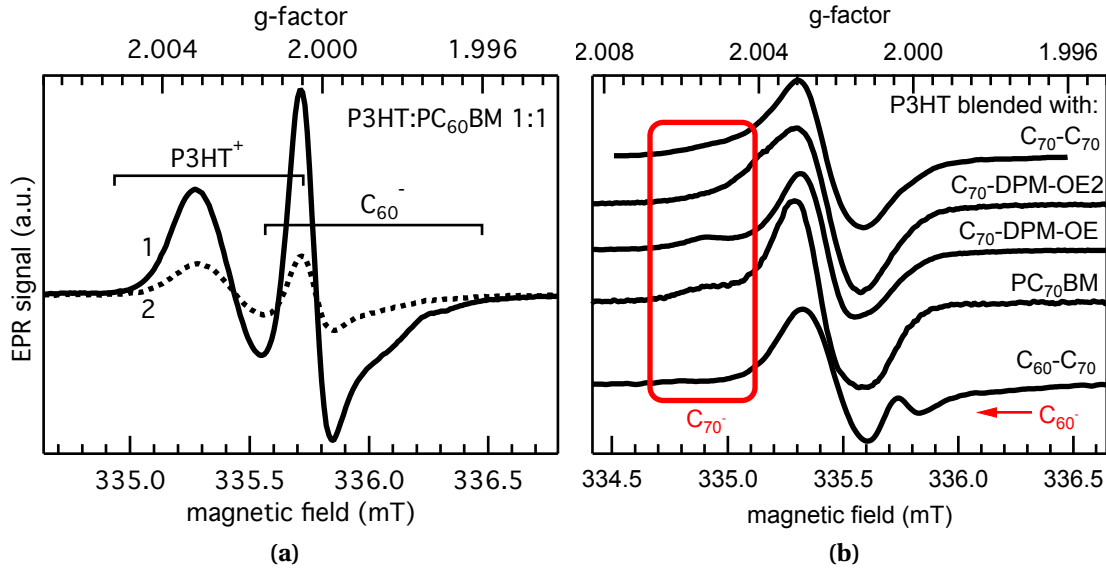


Figure 5.5: (a) EPR spectra of P3HT:PC₆₀BM 1:1 blend at T = 30 K: (1) under illumination; (2) after illumination (light off). (b) EPR spectra at 100 K of P3HT blended with different fullerene-derivatives. All C₇₀-containing composites show a shoulder for $g \geq 2.005$ (indicated by the red rectangle) which is assigned to the C₇₀ anion.

Figure 5.6a shows the spectral series taken in the dark, under ambient light conditions, and at 0.8, 8, and 80 mW laser excitation power, respectively. The vertical markers indicate the positions (shoulders) of interest at which the amplitudes of the spectra were determined. These values are shown in the inset of Figure 5.6a, indicating slightly different behavior for different parts of the EPR spectra.

In particular, it is seen that, at the highest excitation intensities, the shoulder at $g = 2.0050$ is growing larger in comparison to the signal position at $g = 2.0005$. This deviating intensity dependence has been reported before [62] and is in accordance with the formation of positive bi-polarons in the P3HT-domain as explained by Savenije et al. [63]. At high light intensities and cryogenic temperatures ($T \leq 30$ K) two P⁺-polarons can form a bi-polaron, which is not detectable by conventional cwEPR. Consequently this leads to the different light saturation behavior observed for P3HT:PC₇₀BM blends as shown in Figure 5.6a.

This finding was used for tentative deconvolution of the EPR spectrum to positive (P3HT⁺) and negative (C₇₀⁻) polarons by normalization and subsequent subtraction, as shown in Figure 5.6b. The overview in Figure 5.7a shows the experimental X-band EPR spectra (black) and the deconvoluted spectra (blue) of P3HT blended with PC₆₀BM (top) and PC₇₀BM (bottom). The extracted spectrum of the P3HT⁺ polaron is identical for both blends (2, 5). The spectra of C₆₀⁻ and C₇₀⁻ can be simulated in very good agreement with the parameters given in Table 5.2 as discussed below.

5.1 Spectroscopic Signatures of Photo-Generated C_{70} -Fullerene Radical Anions

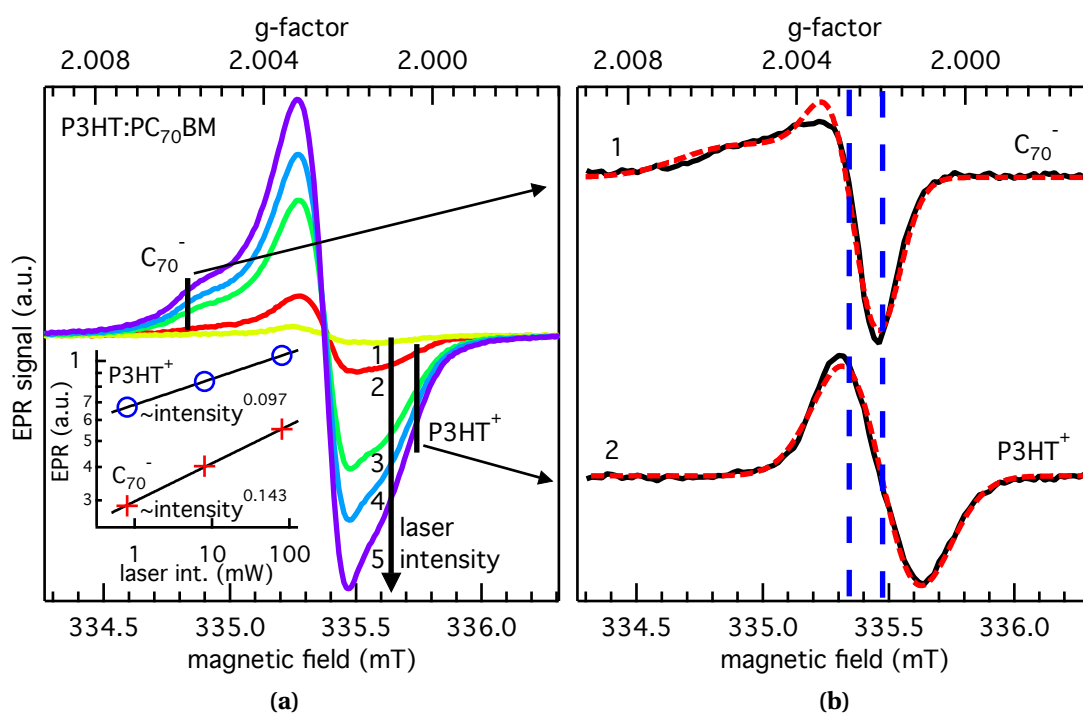


Figure 5.6: (a) X-band EPR spectra of a P3HT:PC₇₀BM blend at T = 30 K. Experimental spectra (1–5) were taken under different illumination conditions: dark, ambient lab illumination, 0.8, 8, and 80 mW laser intensity. The vertical markers indicate the positions (shoulders) at which the light intensity dependence was measured. Inset: EPR amplitude as a function of laser intensity for the marked position corresponding to C₇₀⁻ and P3HT⁺ contributions to the spectra and fitted with a power law. (b) Subtracted spectra of (2) and (5) after normalization at the vertical markers are assigned to (1) C₇₀⁻ and (2) P3HT⁺. Red (dashed) lines: simulated spectra with parameters from Table 5.2.

5 Results

The line shape and the g -value of the C_{70}^- EPR spectrum obtained as described above considerably differ from those of C_{60}^- in a similar composite environment. This striking observation is ambiguous, considering the low spectral resolution of X-band EPR. therefore, a direct experimental confirmation with higher resolution is necessary.

HFEPR

In order to spectrally separate overlapping signals with close g -values and to extract the parameters of the g -tensor, we applied the high frequency EPR technique (D-band 130 GHz). HFEPR spectra of P3HT:PC₆₀BM and P3HT:C₇₀-DPM-OE are shown in Figure 5.7b. The P^+ and P^- signals of P3HT:PC₆₀BM composites are now completely separated (1). Note that in a pulsed EPR experiment, the signals are detected as microwave absorption, while, in cwEPR experiments, the signals are detected as the first derivative of the absorption. For better comparison, we depicted the first derivative EPR spectrum together with the fit (2). The signal at $g = 2.000$ corresponds to C_{60}^- and shows near axial symmetry of the g -tensor. The high field part of this signal (corresponding parallel component $g_{||}$ of the g -tensor of the C_{60}^- spectrum) is very broad. Such large broadening is typical for a g -strain effect, when one or another g -tensor component is distributed mainly owing to the interaction with the environment. In the first approximation, the bigger initial shift of the g -tensor component from the free electron g -tensor, $g_e = 2.0023$, the stronger the g -strain effect. The large g -strain of the $g_{||}$ component reflects the sensitivity of the C_{60}^- molecular orbital energy levels of unoccupied molecular orbitals (see below) to the heterogeneous environment.

The line around $g = 2.0025$ (Figure 5.7b (1, 2)) is due to a positive polaron P^+ on the polymer chain with rhombic symmetry of the g -tensor. The low field component of P^+ is also unusually broadened which might be explained by the g -strain effect as well, and the sensitivity of the P3HT energy levels of occupied orbitals (see below) to the heterogeneous environment.

The HFEPR spectra of blends of P3HT with C_{70} -derivatives show only one broad signal with several shoulders at higher and lower g -factor (Figure 5.7b (3)). This signal is much more extended towards higher g -factors than the signal of P^+ in P3HT:C₆₀-derivative blends. Considering the X-band EPR results, it presumably consists of two overlapping spectra, one corresponding to $P3HT^+$ and another one to C_{70}^- . As the line shape of the P^+ signal, which is localized on P3HT, is expected to be identical for the C_{60} and C_{70} composites (compare Figure 5.7a), we can obtain a spectrum of the C_{70} radical anion by subtracting the low field parts of these two spectra, as shown in Figure 5.7b (4) ($4 = 1 - 3$). Again, to draw parallels between cw- and pulsed-EPR, the spectrum (5) is plotted as the first derivative of (4) together with the fit.

5.1 Spectroscopic Signatures of Photo-Generated C_{70} -Fullerene Radical Anions

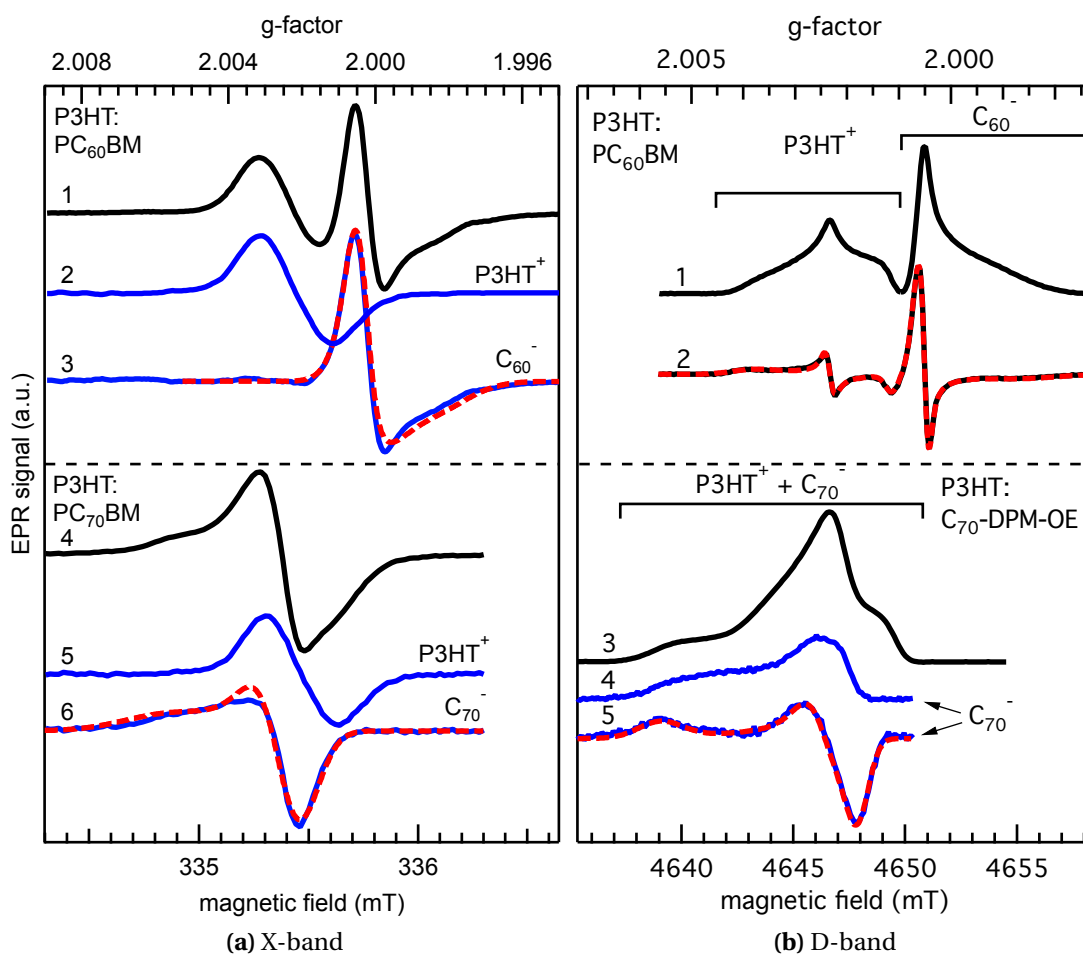


Figure 5.7: Comparison of X- and D-band EPR. Spectra taken at $T = 30$ K. Black: experimental spectra. Blue: deconvoluted by subtraction. Red dashed: simulation using parameters from Table 5.2. **(a)** X-band EPR spectra of P3HT:PC₆₀BM (top) and P3HT:PC₇₀BM (bottom). **(b)** D-band EPR spectra of P3HT:PC₆₀BM (top) and P3HT:C₇₀-DPM-OE (bottom). (1, 3) Experimental spectra, (2) first derivative of (1), (4) subtraction of P3HT⁺ spectrum (low field part of (1)) from (3), (5) first derivative of (4).

5 Results

The resulting signal (5) is matching the deconvoluted signal in X-band (Figure 5.7a (6)), demonstrating the good agreement of the two EPR techniques and the validity of our findings.

The signal obtained by the subtraction procedures in X- and D-band is definitely due to a negative polaron localized on the C_{70} molecule. However, it can be localized either on the C_{70} -cage or on the side-chain. To answer this question, we recorded spectra from composites of P3HT: C_{70} -derivatives that differ by their side-chains. With X-band EPR we tested various fullerene derivative blends yielding equivalent spectra (Figure 5.5b) with the same shoulder at $g \geq 2.005$, that only differed by the relative intensities of the underlying signal constituents. Using D-band EPR we were able to directly confirm that blends of P3HT with either $PC_{70}BM$ or C_{70} -DPM-OE show identical spectra of the C_{70} radical anion. We want to emphasize that X- and D-band EPR spectra were found to be equivalent, i.e. they did not depend on the chemical structure of the side-chain. Thus, we believe that the spectra in Figure 5.7 (bottom) are due to negative polarons being localized on the C_{70} -cage. The signal demonstrates a g -tensor close to axial symmetry, with higher anisotropy compared to the polaron localized on C_{60} , which reflects the lower symmetry of the C_{70} -molecule. The g -tensor parameters of the polaronic signals are summarized in Table 5.2.

Table 5.2: Main components of the g -tensors of positive ($P3HT^+$) and negative (C_{60}^- and C_{70}^-) polarons in P3HT-fullerene blends.

g -tensor ^{a)}	$P3HT^+$	C_{60}^-	C_{70}^-
g_{xx}	2.00380	2.00058	2.00592
g_{yy}	2.00230	2.00045	2.00277
g_{zz}	2.00110	1.99845	2.00211

^{a)} The relative error in the g -tensor measurements is ± 0.00005 .

5.1.4 Discussion

It is important to note that, while the g -tensor components of the C_{60} anion radical are lower than the free electron g -factor ($g_e = 2.0023$), for C_{70}^- the g -tensor components are mostly higher than g_e . According to the classical Stone theory of g -factors [64], a negative deviation of the g -factor from the free electron value is due to spin-orbit coupling with empty p- or d-orbitals, while spin-orbit coupling with occupied orbitals leads to positive deviations. The latter case is more often encountered for pure organic radicals. Thus, a difference in the g -value is an indication for the different electronic structure of molecular orbitals in C_{60} vs. C_{70} anion radicals.

5.1 Spectroscopic Signatures of Photo-Generated C_{70} -Fullerene Radical Anions

Previous studies of C_{70}^- in the liquid phase at room temperature [46, 65] demonstrate that the average g -factor of C_{70}^- is higher than the g -factor of C_{60}^- . This positive shift of the g -factors in solution has been explained on the basis of the static Jahn–Teller effect [66, 67]. It is probable that Jahn–Teller dynamics in the solid phase are quite different for C_{60} and C_{70} molecules, which might contribute to different signs of the g -value shifts [67]. Nevertheless, there is no unified theory that can explain g -tensors of both C_{60}^- and C_{70}^- radicals yet. Our precise measurements of the anisotropic g -tensor of C_{70} anion radicals in the solid phase might be a reference point for developing and testing such a unified theory.

Finally, the reported pulsed HFEPR experiments were carried out on samples that were dried in N_2 atmosphere. Upon removing the solvent by evaporation, the intensities of the lines considerably decreased and almost completely disappeared after annealing of the films. At the same time, a narrowing of the $P3HT^+$ spectra was observed. Both observations can be explained in accordance to literature:

The loss in EPR signal intensity upon annealing of the sample has been discussed in detail by Savenije et al. [63]. The heat-induced change in morphology leads to a growth of separate domains and to ordering within these domains of polymer and fullerene. This is accompanied by a loss of interface area and reduced concentration of trapping sites. Hence, the steady-state concentration of charge carriers at low temperatures dramatically decreases upon ordering due to temperature-assisted annealing.

The observation of the change in linewidth is best explained with the effect of motional narrowing [19, 20]. The $P3HT^+$ spectrum is broadened by unresolved hyperfine interactions with surrounding protons. With higher mobility, more protons interact with the polaron in a given period of time, resulting in a narrowing of the line due to the enhanced motion of the polaron (also see Section 3.2.2 about line broadening). For $P3HT$ the mobility is enhanced enormously upon annealing, caused by the resulting higher degree of order in this otherwise mostly amorphous polymer. Thus, the narrowing of the P^+ linewidth from frozen solution via dried film to annealed film reflects the change in charge carrier mobility. A high degree of polaron delocalization in the annealed samples is also confirmed by shortening of the relaxation time T_1 as measured by the spin echo technique in HFEPR.

5.1.5 Conclusion

To summarize, we have studied a variety of solid films of C_{70} -fullerene derivatives and dimers blended with two different conjugated polymers, with the emphasis on the photogenerated radical anion. We identified spectral features originating from C_{70} in PIA and EPR spectroscopy, namely an additional sub-gap PIA peak at 0.92 eV and an EPR-shoulder at $g \geq 2.005$. By comparing results from different blends we can infer that these features are indeed signatures of the C_{70} radical anion and not originating from the side chains of the fullerenes or charge transfer states at polymer: C_{70} -fullerene interfaces. When recorded with conventional X-band EPR, this signal is overlapping with the signal of the positive polaron, which does not allow for its direct identification. Owing to the superior spectral resolution of the HFEPR technique, we were able to separate light-induced signals from positive and negative polarons and provided the first experimental identification of the radical anion localized on the C_{70} -cage in P3HT: C_{70} -derivative composites. The reported PIA-band and g -tensor parameters are of importance, as these are the characteristic fingerprints of the charge separated state and enable directed studies of charge transfer reactions in C_{70} -based bulk-heterojunctions.

5.2 CT in Polymer:PC₆₀BM:PC₇₀BM Ternary Blends: Which Fullerene Gets the Electron?

Abstract

The highest efficiencies reported for organic solar cells are for devices incorporating blends of conjugated polymers and C₇₀-derivatives, due to their higher optical absorption compared to C₆₀. Yet the costly purification of higher fullerenes might hinder a widespread adoption of this promising material class. However, recent results showed that polymers blended with an unpurified mixture of the derivatives PC₆₀BM and PC₇₀BM yield solar cells with comparable performance.

This is surprising, because from absorption and photoluminescence spectra, different energy levels for both fullerenes are expected. If there were a noticeable difference in electron affinity, one of the two fullerenes would act as an electron trap in a mixed phase, hence hindering transport and limiting device performance. This raises the question on which fullerene type the electron is residing after light induced charge transfer from the polymer? Using light-induced EPR, we can distinguish between holes on the polymer and electrons on either C₆₀ or C₇₀, since their EPR spectra are slightly shifted against each other. Our results demonstrate that there is no strong preference for either fullerene. Thus from an economic point of view “unpurified” fullerenes might be a viable option for large scale production.

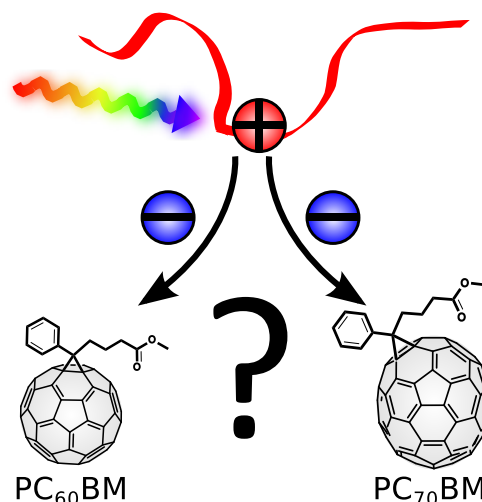


Figure 5.8: If different fullerene acceptors are available, which one gets the electron after photoinduced electron transfer from a conjugated polymer?

5.2.1 Introduction

Even with the obvious advantages of C_{70} -derivatives for organic solar cells, from an economic point of view it might be too expensive for wide-spread usage [68]. The production of raw fullerenes typically yields C_{60} , C_{70} and higher fullerenes in a ratio of approximately 3/4, 1/4 and 1–3 %, respectively (see Figure 5.9). After purification to >99 % purity, the price of C_{70} is about one order of magnitude higher than for C_{60} . Additionally, producing solution processable derivatives such as PCBM raises the price to the order of several hundred euros per gram. Therefore it should be investigated on how to reduce this intrinsic cost factor, especially for C_{70} .

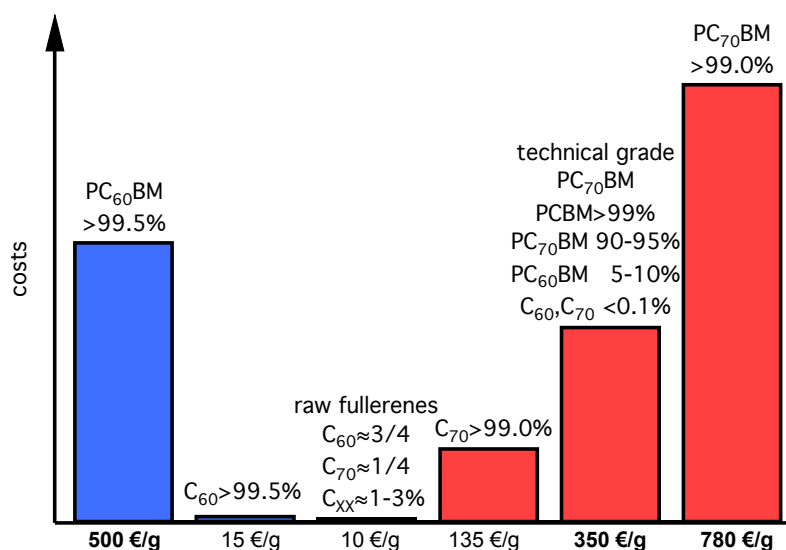


Figure 5.9: Costs per g and purity of fullerenes and PCBM-derivatives. Prizes from NeoTech-Product.ru (raw fullerenes) and Solenne BV (purified fullerenes and PCBM). Note the steep increase in pricing for purification and adding PCBM-sidechains.

Recent results by Popescu et al. demonstrate that the purification step itself might not be necessary to its full extent. Solar cells produced from the polymer P3HT with a PC₆₀BM / PC₇₀BM-mixture without further purification achieve the same efficiency as those produced from purified PC₇₀BM [69]. The author suggests a so-called “technical-grade” PC₇₀BM which has a high percentage of PC₇₀BM (90–95 %) with the rest mainly being PC₆₀BM (5–10 %), while other (higher) fullerenes are excluded to be possible impurities ($\ll 0.1$ %). Nowadays technical-grade PC₇₀BM can be purchased for less than even the highly purified PC₆₀BM from Solenne BV [70].

Comparison of Fullerene Energy Levels

It is surprising that solar cells using a non-purified “technical grade” PC₇₀BM do work, because the energy levels of C₆₀ and C₇₀ were thought to be not exactly identical. If there were a difference in electron affinity for C₆₀ and C₇₀, one of the two could act as an electron trap in a mixed phase, hence hindering electron transport and limiting device performance. Having a closer look at the differences of the molecules is essential.

The comparison of the field-effect mobilities measured in field-effect transistors made from PC₆₀BM and PC₇₀BM showed very similar electron mobilities [71]. This is also favorable for the intended use in a mixed phase and underlining their potential electronic compatibility. In contrast to that, a recent study by Schafferhans et al. on fullerene-based thin-film diodes has shown that while there are similar electron trap densities in both PC₆₀BM and PC₇₀BM, the traps are deeper in devices employing PC₇₀BM [72]. The deliberate doping of polymer:PC₆₀BM solar cells with very small amounts of PC₈₄BM was even used to directly study the deteriorating effect of deep trap states in the fullerene-phase on solar cell performance and recombination mechanisms [73]. Using transient absorption spectroscopy, the polaron recombination dynamics in P3HT:fullerene blend films were studied for C₆₀, C₇₀ and C₈₀ with PCBM and bis-PCBM side chains attached. They were found to be largely acceptor dependent, explained by the difference in shielding of the fullerene by its side chain(s) [74]. For pure fullerenes a direct comparison of cyclo-voltammetry of PCBM-derivatives made from C₆₀, C₇₀ and C₈₄ has shown that the HOMO / LUMO levels of PC₆₀BM and PC₇₀BM differ slightly by 5–15 meV, while PC₈₄BM is shifted by ≈300 meV, explaining its enhanced electron trapping properties [75, 74]. Additionally, from PL-spectra, the singlet-gap for radiative recombination has been determined to be 1.70 eV for PC₇₀BM and 1.66 eV for PC₆₀BM. Hence, the PL is red-shifted by 40 meV for PC₆₀BM [76] (see previous Chapter 5.1).

The reported differences for C₆₀, C₇₀ and their derivatives are small, but nonetheless they demonstrate that the molecules are energetically not identical. The question arises which fullerene will get the electron after photo-induced charge transfer from the donor material, if both C₆₀ and C₇₀ are available. Do the energetic differences of the fullerenes have an influence on the charge transfer reaction?

Use of EPR to Study Ternary Blends

The previous Chapter discussed in detail that the EPR spectra of electrons and holes in polymer:fullerene blends deviate strongly from one another. Consequently it is possible to distinguish electrons localized on either C₆₀ or C₇₀, making the electron population densities of the two fullerenes directly accessible [76, 77].

5 Results

A closer look at the spectrum of P3HT blended with a special C₆₀-C₇₀-dimer molecule already revealed that contributions of both fullerene anions are present, indicating that the charge transfer process might not be dominated by one fullerene type (see Figure 5.5b in the previous Chapter).

In this study we used the obtained knowledge about the EPR signatures of both fullerenes to measure the electron distribution in ternary blends of PC₆₀BM, PC₇₀BM and the donor polymer P3HT. From the results we then estimated the actual energetic difference for an electron to be localized on either fullerene in a mixed phase.

5.2.2 Experimental Details

Samples

The materials used for this study are the conjugated polymers P3HT and PTB7 together with the fullerene-derivatives PC₆₀BM and PC₇₀BM (see Chapter 2.4). The PCBM-derivatives were obtained from Solenne BV. No additional purification was performed. The stated purity for PC₆₀BM is >99.5 % and >99.0 % for PC₇₀BM. Additionally, we obtained a “technical grade” PC₇₀BM, which consists of a mixture of 93.8 % PC₇₀BM and 6.2 % PC₆₀BM (weight-%), as stated for this batch by Solenne BV. Known impurities consist of <0.1 % C₆₀ and C₇₀ without sidechains, while higher fullerenes (such as C₈₄), are excluded to be possible impurities (\ll 0.1 %). The overall purity of PCBM-derivatives is >99 %.

Sample preparation took place inside a nitrogen glovebox to avoid exposure to oxygen. The materials were dissolved in chlorobenzene with a concentration of 20 mg/ml and stirred over night. Then, small amounts of the polymer and fullerene solutions were mixed in the desired blend ratio. P3HT was blended with equal amounts of fullerenes (100 : 100), as this is approximately the best mixing ratio considering solar cell performance. The fullerene amount X was varied between only PC₇₀BM ($X = 100$) and only PC₆₀BM ($X = 0$). Therefore the total blend ratio was P3HT:PC₇₀BM:PC₆₀BM = (100 : X : 100 - X). After vacuum-drying 0.2 ml portions of the solutions in EPR tubes, the sample tubes were flushed with helium several times and finally sealed under \approx 20 mbar helium atmosphere with a blow torch. EPR spectra were recorded for as-prepared samples and additionally after 10 min thermal annealing at 130°C.

To exclude the presence of paramagnetic impurities, such as residual metallic catalysts from the synthesis, a full sweep EPR spectrum over the accessible magnetic field range of the spectrometer was recorded for several of the prepared samples. Despite the expected polaronic signatures of P3HT⁺, C₆₀⁻ and C₇₀⁻, no additional EPR signals were found, stating the high purity of the used materials.

EPR

EPR spectra were recorded with the X-band spectrometer described in Chapter 4. The magnetic field modulation amplitude was set to 0.05 mT. The g -factor was calibrated for each measurement according to Chapter 4.2. Illumination was provided by a 532 nm DPSS laser arriving in the cavity with 20 mW.

Measuring cwEPR spectra of polarons in organic semiconductors at cryogenic temperatures needs careful considerations concerning which microwave power settings are suitable. At low temperatures the cwEPR spectra of spins in organic semiconductors always show microwave power saturation to some extent, due to fast passage effects and saturation of the spin lattice relaxation time. It is thus impossible to directly determine the total number of spins from an EPR signal. A straightforward solution for this task would be to record the EPR spectra at very low microwave powers to prevent signal saturation. However, at temperatures below 70 K this is not feasible with the lowest accessible microwave power settings of a cwEPR spectrometer for this kind of organic samples.

Figure 5.10a shows typical spectra of a 100 : 50 : 50 blend of P3HT:PC₇₀BM:PC₆₀BM for different microwave power settings taken at 70 K. The inset shows intensities measured at the two positions marked with small vertical arrows (C_{70}^- and C_{60}^-) at $g = 2.0054$ and $g = 1.9992$. At the higher g -factor position only C_{70}^- contributes to the measured signal intensity, while at the lower g -factor a superposition of mostly C_{60}^- and to some extent P3HT⁺ contributes. This is sufficient in this case to show the effect of saturation. All signals show saturation – they deviate from the non-saturated ideal square root line (steeper black line in the inset). Even for the lowest power setting this is probably still the case. Thus, a hypothetical identical number of spins for each of the three spin species would yield different EPR signal intensities at a given temperature and microwave power. However, the saturation behavior of these species is expected to remain identical for each of the studied blending ratios. therefore its effect can be adjusted by careful normalization as described below.

Additionally, Figure 5.10b shows the respective polar plot of the lock-in raw-data (X and Y), with the detection phase Θ determining the in-phase and out-of-phase EPR signal. For the highest microwave power setting, the signal is highly distorted and shows large deviations in form of out-of-phase contributions. This kind of measurement is unsuitable for the planned signal analysis, since it is not even possible to accurately determine a *single* detection phase Θ for all signal components. For the lower two microwave power settings, all signal components are in-phase with the detection angle Θ . While the signals are partly saturated, they do not show additional out-of-phase distortions, which is favorable for the intended intensity analysis.

5 Results

In this case (70 K), a microwave setting of 0.632 mW (25 dB) yields optimal signal-to-noise ratio and only minor out-of-phase distortions in the polar plot. The same considerations were made for all measurement temperatures and the following settings were found to yield undisturbed signals with reasonable signal-to-noise ratio: 0.020 mW for 15 K and 20 K / 0.0632 mW for 30 K / 0.632 mW for 70 K and 6.32 mW for 100 K.

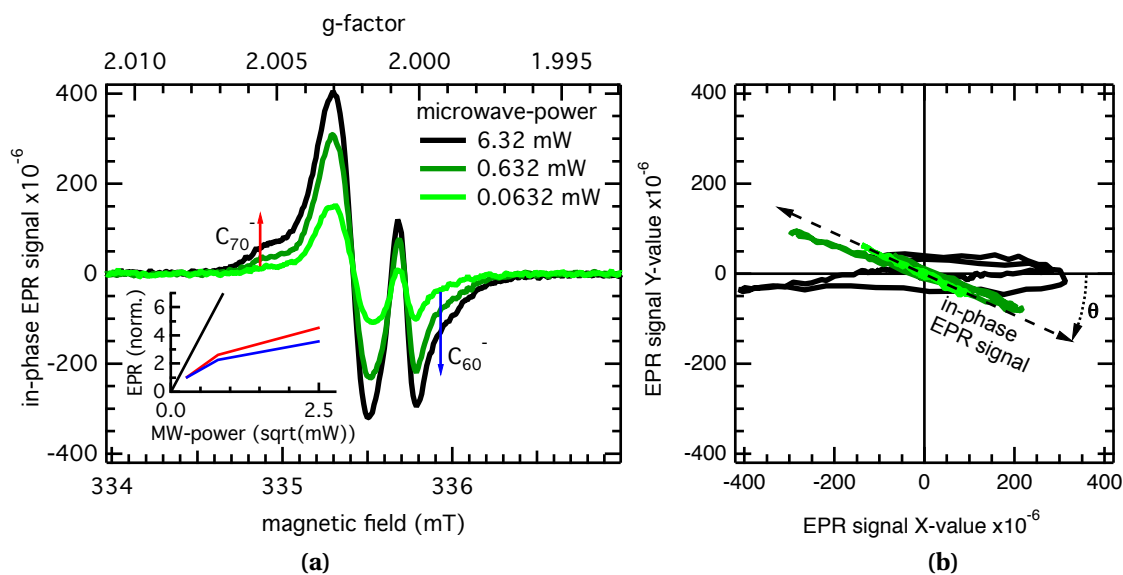


Figure 5.10: **a)** Exemplary EPR spectra taken for different microwave powers at 70 K. The inset shows the normalized EPR signal intensities for C_{60}^- and C_{70}^- , measured at the marked positions, over the square root of the microwave power setting. The steeper black line is a guide to the eye, representing a non-saturated signal. **b)** Polar plot of the corresponding lock-in raw-data (X and Y). The detected signal changes in intensity and especially signal-phase Θ , due to saturation of the EPR lines.

5.2.3 Results

EPR spectra

Figure 5.11 shows EPR spectra of illuminated blends of P3HT:PC₇₀BM:PC₆₀BM with blending ratios of 100 : X : 100 – X. Additionally, a sample with the commercially available “technical grade” PC₇₀BM was measured (93.8 %). Simulations of the positive polaron P3HT⁺ localized on the polymer as well as the signatures of the radical anions C_{60}^- and C_{70}^- are shown for comparison. All three components have slightly different g-factors, which results in a spectral shift towards each other. The experimental spectra are superpositions of the individual components with their relative intensities depending on the number of charge carriers localized on the respective material. Of special interest are the spectral positions marked by the vertical arrows I_{exp1} and I_{exp2} , where the

5.2 CT in Polymer:PC₆₀BM:PC₇₀BM Ternary Blends: Which Fullerene Gets the Electron?

gradual change of the spectra from 0 % (no PC₇₀BM) to 100 % (no PC₆₀BM) is reflected by the shifting intensities between the contributions of C₆₀⁻ and C₇₀⁻ to the spectrum.

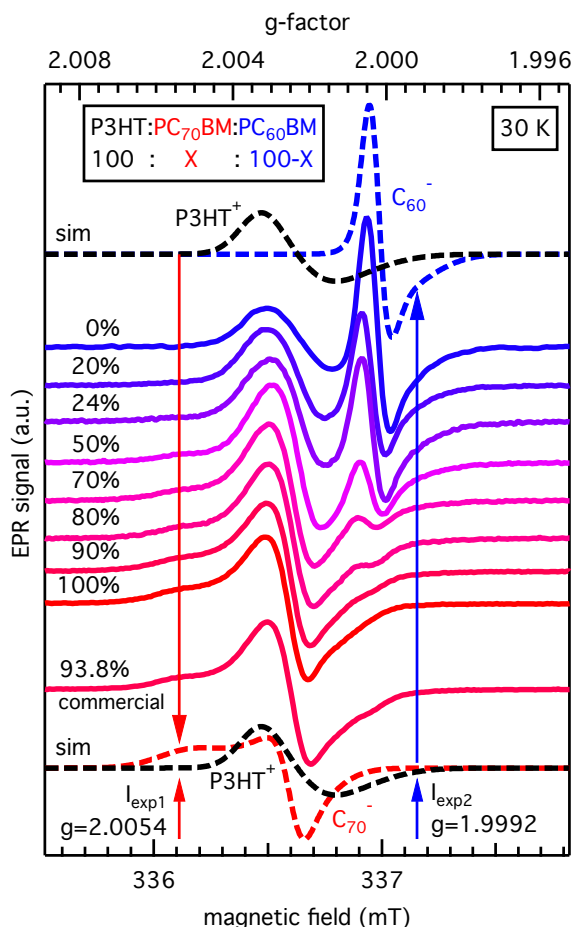


Figure 5.11: Experimental EPR spectra (solid lines) of P3HT:PC₇₀BM:PC₆₀BM blends with varying PC₇₀BM percentage of the fullerene contents (T = 30 K). A sample with the commercial “technical grade” PC₇₀BM has also been measured. Dashed lines show simulations of the spectra of P3HT⁺, C₇₀⁻ and C₆₀⁻ for comparison. The red and blue vertical arrows mark the spectral positions at which the intensities I_{exp1} and I_{exp2} have been measured in order to quantify the distribution of electrons between the two fullerenes.

Additional measurements have been made (not shown) for blends with the polymer PTB7. The EPR spectra are similar to those on the basis of P3HT. At the sides of the spectrum, where C₆₀⁻ and C₇₀⁻ contribute to the signal intensity, features of both fullerene radical anions can be detected according to their weight-percentage. However, a detailed analysis as described below for P3HT is not possible since the broad linewidth of PTB7⁺ overlaps completely with the fullerene signatures. Nevertheless, there is no indication that the distribution of electrons between the two fullerenes is influenced by the choice of the donor polymer.

Influence of Temperature, Excitation Wavelength and Thermal Annealing

Measurements were carried out at temperatures of 100 K and below, because only at cryogenic temperatures, a sufficient signal-to-noise ratio can be achieved for these and similar materials [62]. At lower temperatures, signal intensities were higher due to enhanced trapping of charge carriers [61]. Line widths also showed a slight temperature dependence, which has been assigned previously to motional narrowing [19]. Overall EPR signal intensities were roughly the same for the changing blend ratios at each temperature. Hence, no enhanced trapping due to the ternary blends was observed. One could have expected additional charge carrier trapping at low temperatures, because deeper lying traps in blends made of PC₇₀BM have been reported in comparison to trap energies in PC₆₀BM [72]. From our results we can infer that this does not seem to be the dominating effect for these ternary blend systems.

We tested whether there is a dependence on the excitation wavelength. Since the two PCBM derivatives have different absorption spectra and will absorb different amounts of the incident light in a solar cell, this could yield an uneven electron distribution. A halogen bulb white light and a 532 nm laser at various illumination intensities were used. To also check for an effect of morphology, EPR spectra were recorded before and after thermal annealing (10 min at 130°C). The resulting spectra differ in overall signal intensity, but overlap perfectly after normalization. Hence, annealing and illumination have no effect on the electron distribution between the two fullerene acceptors.

We want to point out that the shown EPR spectra reflect the steady state populations after charge transfer and relaxation of the charges in the different domains of the blend films. Because the spectra are independent of experimental conditions and sample treatment, we can deduce that the distribution of electrons between the two fullerenes depends solely on their energetics and respective weight-percentage in the samples.

EPR Simulations

Simulations and fits of the EPR spectra were performed using EasySpin [48] and further data analysis was done with Igor Pro. The spectra of the 1:1 blends of P3HT:PC₆₀BM and P3HT:PC₇₀BM were fitted using the *g*-factor values known from our previous studies presented in Chapter 5.1 and in literature [77]. Free fitting parameters were the intensities and the linewidths (*g*-strain), as they are changing slightly with experimental conditions. Also the *g*-tensor values needed very minor adjustments as these components of the parameter set do also have a slight dependence on the magnetic field strength used in the EPR spectrometer (in this case 0.335 T in comparison to 4.65 T used in previous work).

5.2 CT in Polymer:PC₆₀BM:PC₇₀BM Ternary Blends: Which Fullerene Gets the Electron?

Table 5.3 shows the used set of parameters for 30 K, with which the isolated spectra of P3HT⁺, C₆₀⁻ and C₇₀⁻ were simulated as shown in Figure 5.11. The values are almost identical to those determined by HFEPR in the previous chapter and agree with them within their error margins (see Table 5.2 for comparison).

$g^{a)}$	P3HT ⁺	strain	C ₆₀ ⁻	strain	C ₇₀ ⁻	strain
g_{xx}	2.00337	0.00121	2.00052	0.00041	2.00543	0.00193
g_{yy}	2.00232	0.00171	2.00031	0.00057	2.00265	0.00064
g_{zz}	2.00107	0.00257	1.99931	0.00190	2.00235	0.00203

Table 5.3: Main components of the g -tensors and g -strains of polymer polarons (P3HT⁺) and fullerene radical anions (C₆₀⁻ and C₇₀⁻) in P3HT-fullerene blends at 30 K.

EPR Data Analysis

The goal of this section is to derive the percentage P of the electron population localized on either fullerene type ($P_{70}(X)$ and $P_{60}(X)$) from their EPR signal intensities, measured for samples with X being the mixing ratio of PC₇₀BM.

A straight-forward approach to extract the relative signal intensities for P3HT⁺, C₇₀⁻ and C₆₀⁻ from the spectra shown in Figure 5.11 would be the following: first, simulation of the separate spectra with the parameter set given in Table 5.3, and second, fitting the experimental spectra by only using the intensities as free fitting parameters. Unfortunately, the almost complete overlap of the involved spin signatures and the limited g -factor resolution of the X-band EPR prevent this approach and render the direct simulations of the ternary blend spectra numerically unstable in EasySpin.

Nevertheless it is absolutely feasible to accurately measure the spectral intensities at well defined positions within the EPR spectra (e.g. I_{exp1} and I_{exp2}) to derive the wanted values for $P_{70}(X)$ and $P_{60}(X)$ using several boundary conditions. In the following, the derivation of these values in dependence of the measured intensities is given.

We start with the definition of $P_{70}(X)$ as being the absolute number of the electrons $N_{70}(X)$ located on C₇₀ over the sum of all electrons $N_{70}(X) + N_{60}(X)$.

$$P_{70}(X) = \frac{N_{70}(X)}{N_{70}(X) + N_{60}(X)} = \left[\frac{N_{60}(X)}{N_{70}(X)} + 1 \right]^{-1} \quad (5.1)$$

In general, for every EPR transition of a studied spin-system the following Equation does apply:

$$I_{spin} = \alpha_{spin} \cdot N_{spin} \quad (5.2)$$

5 Results

Here, I is the observed EPR intensity and α is a proportionality factor depending on the experimental conditions (e.g. temperature, microwave power), the spin system (e.g. line width, spin relaxation times, saturation), and the exact g -factor at which the EPR intensity of the given species is probed within the observed spectral width.

For the studied samples the following boundary conditions do apply:

$$N_{pol}(X) = N_{70}(X) + N_{60}(X) \quad (5.3)$$

The total number of holes is equal to the sum of all electrons. This simplifies to the following, if one of the two fullerenes is omitted for $X = 100$ or 0 , respectively.

$$N_{pol}(100) = N_{70}(100) \quad (5.4)$$

$$N_{pol}(0) = N_{60}(0) \quad (5.5)$$

Using these considerations leads to the following expression for $P_{70}(X)$:

$$P_{70}(X) = \left[\underbrace{\frac{I_{60}(X)}{I_{70}(X)}}_A \cdot \underbrace{\frac{I_{70}(100)}{I_{pol}(100)}}_{\frac{1}{R100}} \cdot \underbrace{\frac{I_{pol}(0)}{I_{60}(0)}}_{R0} + 1 \right]^{-1} \quad (5.6)$$

Part A is the fraction of the measured intensities of electrons on the two fullerene species, while $\frac{R0}{R100}$ is equal to $\frac{\alpha_{70}}{\alpha_{60}}$ and is nothing else than the normalization due to Equation 5.2.

After careful consideration EPR intensities were extracted at the left and right side of the three overlapping EPR spectra: I_{exp1} at $g = 2.0054$ and I_{exp2} at $g = 1.9992$. This lead to the smallest possible errors in the analysis. At the first spectral position I_{exp1} , only C_{70}^- yields any signal intensity:

$$I_{exp1}(X) = I_{70}(X) \quad (5.7)$$

Unfortunately, there is no spectral position where only signal intensity of C_{60}^- can be detected ($I_{60}(X)$) without a background of the positive polaron I_{pol} localized on the polymer, due to the broad line width of the polymer EPR signal. Therefore, at the second spectral position I_{exp2} , the sum of holes on the polymer and electrons on C_{60} is being detected:

$$I_{exp2}(X) = I_{60}(X) + I_{pol}(X) \quad (5.8)$$

5.2 CT in Polymer:PC₆₀BM:PC₇₀BM Ternary Blends: Which Fullerene Gets the Electron?

For the case of the sample without PC₆₀BM ($X = 100$), this simplifies to:

$$I_{exp2}(100) = I_{pol}(100) \quad (5.9)$$

Using Equations 5.7 and 5.9, the ratio $R100$ of Equation 5.6 can be linked to experimental data:

$$R100 = \frac{I_{pol}(100)}{I_{70}(100)} = \frac{\alpha_{pol}}{\alpha_{70}} = \frac{I_{exp2}(100)}{I_{exp1}(100)} \quad (5.10)$$

To also link the ratio $R0$ of Equation 5.6 to accessible intensities, the help of simulations is necessary. Since for the case of $X = 0$ (no PC₇₀BM), the resulting EPR spectrum of P3HT⁺ and C₆₀⁻ has the smallest amount of spectral overlap, the performed simulations have the highest possible degree of certainty, yielding the necessary relative intensities.

$$\text{from simulations: } R0 = \frac{\alpha_{pol}}{\alpha_{60}} = \frac{I_{pol}(0)}{I_{60}(0)} \quad (5.11)$$

With the formalism above, $I_{60}(X)$ can be written as

$$I_{60}(X) = \frac{I_{exp2}(X) - R100 \cdot I_{exp1}(X)}{1 + R0} \quad (5.12)$$

Including Equation 5.7 and the expression for $I_{60}(X)$ into Equation 5.6 yields a useable expression for $P_{70}(X)$.

$$P_{70}(X) = \left[\underbrace{\frac{I_{exp2}(X)}{I_{exp1}(X)} - R100}_{A} \cdot \frac{R0}{R100} + 1 \right]^{-1} \quad (5.13)$$

Figure 5.12 shows the resulting percentage of electrons $P_{70}(X)$ and $P_{60}(X)$ in dependence of the PC₇₀BM weight ratio X . The data set for the commercially available “technical grade” PC₇₀BM (93.8 %) has also been included. The analysis was carried out for several temperatures, of which 15, 30, 70 and 100 K for annealed samples are shown in Figure 5.12a. Data sets for measurements at 20 K of annealed samples are shown together with those at 30 K and 70 K for not annealed samples in Figure 5.12b.

For comparison, the diagonal solid lines are added, which represent what an even distribution of electrons between both fullerenes would be according to the weight-percentage (X). The experimental values are very close to this ideal distribution and agree with it considering the error bars. The advantage in signal-to-noise for the lower temperature measurements is obvious.

5 Results

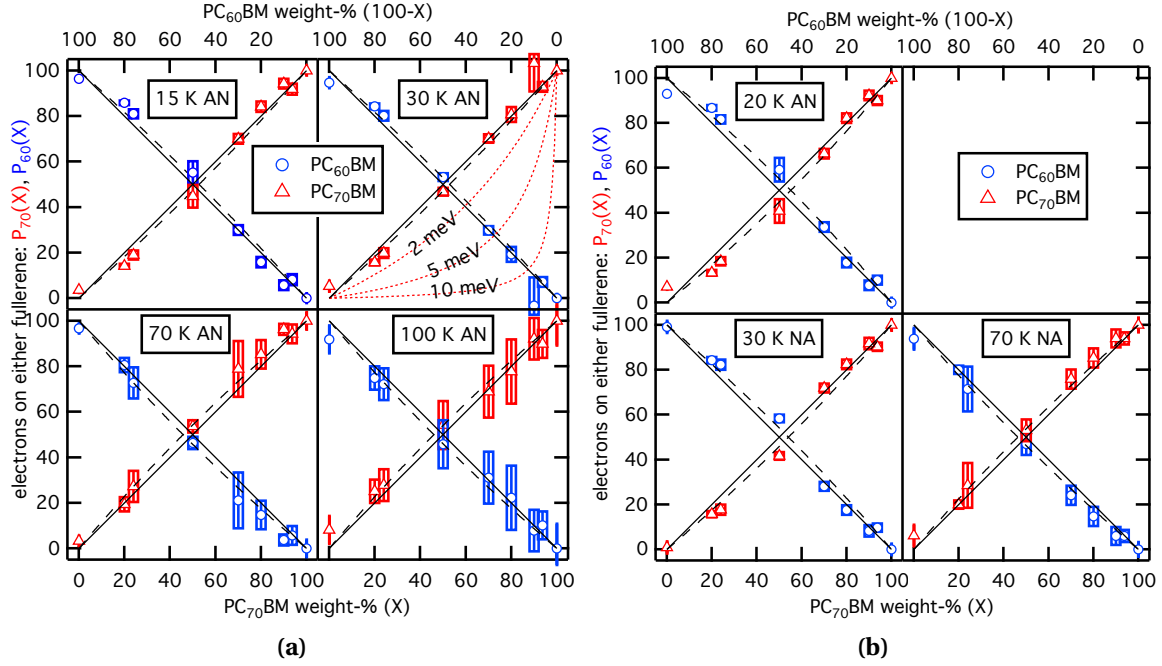


Figure 5.12: Distribution of electrons localized on either PC₇₀BM or PC₆₀BM depending on the fullerene weight-percentage for annealed (AN) and not annealed (NA) samples. The solid diagonal lines are guides to the eye, corresponding to a distribution equal to the weight ratio. The curved dashed lines are fits to the data using the Boltzmann-distribution shown in Equation 5.16. The dotted red curves in the plot (30 K AN) are exemplary simulations for the energy of an electron on PC₇₀BM being a few meV higher than for PC₆₀BM.

Error Estimation

The error bars shown in Figure 5.12 are derived in the following way: The horizontal error bars are estimated from the weighing and liquid mixing uncertainties while producing the small sample amounts ($\pm 2\%$). The vertical error bars are calculated by quantifying the standard deviation σ_{off} of the off-resonance zero line of the EPR spectra far from the resonance (noise floor at $g < 1.996$ and $g > 2.008$) and setting twice this value in relation to the sum of the two measured intensities:

$$vertical\ error = \frac{2 \cdot \sigma_{off}}{I_{exp1} + I_{exp2}} \quad (5.14)$$

Determining the Energy Difference

The electron populations (N_1 , N_2) can be approximated as a two-level system with the two fullerenes providing a higher and a lower-lying energetic level for electrons, separated by an energy-gap ΔE . This kind of system can be described by a Boltzmann distribution:

$$\begin{array}{c} N_2 \text{ --- } C_{70} \\ \updownarrow \Delta E \\ N_1 \text{ --- } C_{60} \end{array} \quad \frac{N_2}{N_1} = \frac{w_2}{w_1} \exp\left(-\frac{E_2 - E_1}{k_B T}\right) \quad (5.15)$$

Here, T is the experimental temperature and k_B the Boltzmann constant. The values w_1 and w_2 are the statistical weights of the two energy levels, hence the relative number of occupiable states X . Applying to the formalism described above this translates to:

$$\frac{P_{60}(X)}{P_{70}(X)} = \frac{X}{1-X} \exp\left(-\frac{\Delta E}{k_B T}\right) \quad (5.16)$$

This distribution can be fitted to the data in Figure 5.12 and is plotted as curved dashed lines for each temperature. Taking the error bars into account, we calculate the corresponding energy values ΔE shown in Figure 5.13 for data sets taken at various temperatures of AN and NA samples. The resulting values are scattered within 2 meV around zero and independent of temperature and annealing treatment. Note that the values for 30 K and 70 K for AN and NA samples do actually overlap almost perfectly well, demonstrating the high level of reproducibility.

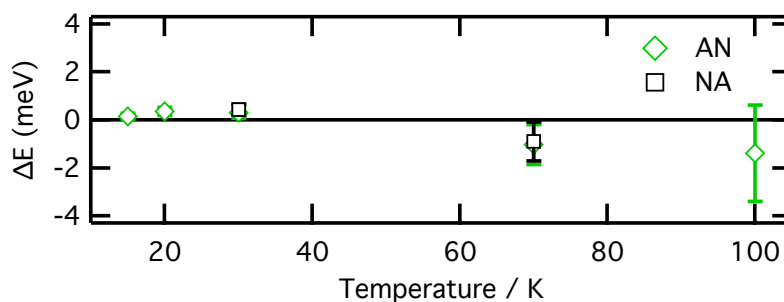


Figure 5.13: Energy gap ΔE derived from the Boltzmann fits for AN and NA samples.

To verify the high energetic sensitivity of this method, exemplary simulations using Equation 5.16 shown as the curved dotted lines in the upper right graph (30 K AN) of Figure 5.12a have been included. They show the energy level of an electron on PC₇₀BM being 2, 5 or 10 meV higher than on PC₆₀BM. If there would be an energy difference ΔE of only a few meV, it would result in a strong occupation preference of the lower-lying fullerene, directly noticeable in the EPR spectra. Consequently it is reasonable to treat this energy difference as 0 ± 1 meV.

5.2.4 Discussion

If we compare this result with the width of the density of states (DOS) in disordered organic materials, commonly discussed to be on the order of tens of meV, one could argue that an energy difference of a few (single digit) meV has probably no effect on real-world devices whatsoever. However, we point out that the approach of using a Boltzmann distribution to quantify this value is only a rough estimate, since we are not dealing with two discrete levels, but largely overlapping energy-bands. Nevertheless the electron distributions shown in Figure 5.12 are in agreement with an even distribution of electrons on both fullerenes, i.e., $\Delta E = 0$.

When studied in a time resolved experiment, we would expect C_{70} to receive a larger share of incident photons than C_{60} , because of its higher optical absorption. This initial excitation inequality between the two fullerenes will then most likely equalize on a sub-ps timescale, while the excitons diffuse towards a heterointerface for charge separation. To come back to the initial question “Which fullerene gets the electron?” or in other words whether one fullerene would act as an energetic trap state for electrons in a ternary blend system. We can now answer and state that both fullerenes, despite their differences when studied in purified form, do have identical electron affinity in a mixed phase: electrons show no preference or enhanced trapping. As a result C_{70}/C_{60} mixtures can be treated as a composite material with the combined advantages of both constituents: high optical absorption and lower price.

5.2.5 Conclusion

With the motivation to reduce the costs of C_{70} derivatives for solar cell absorbers, we have studied blends of P3HT:PC₇₀BM with differing doping levels of PC₆₀BM. As the purification of C_{70} is expensive, the most probable impurity being C_{60} , we were interested in whether the purification process might not be necessary to the full extent, hence leaving C_{60} as an impurity in an industrial scale process.

Analyzing relative EPR signal intensities we have found that in ternary blends of P3HT:PC₇₀BM:PC₆₀BM, the electron populations on the two fullerenes distribute directly proportional to their respective weight-percentage. When compared to a Boltzmann distribution, an estimate for the energy difference for electrons localized on either fullerene can be derived to be on the order of less than 1 meV. These results demonstrate that any energetic differences between C_{60} and C_{70} fullerene derivatives, which are present when measured in purified form, are leveled out in a mixed phase.

This finding is valid, regardless of the experimental conditions we applied, e.g. the temperature (10–100 K) and excitation wavelength (532 nm, white light) or sample an-

5.2 *CT in Polymer:PC₆₀BM:PC₇₀BM Ternary Blends: Which Fullerene Gets the Electron?*

nealing treatment. Additionally, no enhanced trapping can be observed, since EPR signal intensities at low temperatures are roughly the same for changing fullerene ratios.

We expect that this result is true not only for PC₆₀BM and PC₇₀BM blended with P3HT, but for pure C₆₀ and C₇₀ as well. Thus, it is expected also to be relevant for solar cells produced by evaporation processes, which could similarly employ unpurified C₇₀ as acceptor material.

We conclude that both fullerenes co-crystallize or at least self-assemble on a small length scale, which results in an averaging effect for the optical and energetic properties of the blend film. Considering costs for the large scale production of organic solar cells, “unpurified” C₇₀ derivatives might be a viable option.

5.3 (Ir-)Reversible P3HT:O₂ Interactions Studied by Spin-Sensitive Methods

Abstract

Understanding of degradation mechanisms in polymer:fullerene bulk-heterojunctions on the microscopic level aimed at improving their intrinsic stability is crucial for the breakthrough of organic photovoltaics. These materials are vulnerable to exposure to light and / or oxygen, hence they involve electronic excitations.

To unambiguously probe the excited states of various multiplicities and their reactions with oxygen, we applied combined magneto-optical methods based on multifrequency (9 and 275 GHz) electron paramagnetic resonance (EPR), photoluminescence (PL), and PL-detected magnetic resonance (PLDMR) to the conjugated polymer P3HT and bulk heterojunctions with the fullerene PC₆₀BM. We identified two distinct photochemical reaction routes, one being fully reversible and related to the formation of polymer:oxygen charge transfer complexes, the other one, irreversible, being related to the formation of singlet oxygen under participation of bound triplet excitons on the polymer chain. With respect to the blends, we discuss the protective effect of the methano fullerenes on the conjugated polymer bypassing the triplet exciton generation.

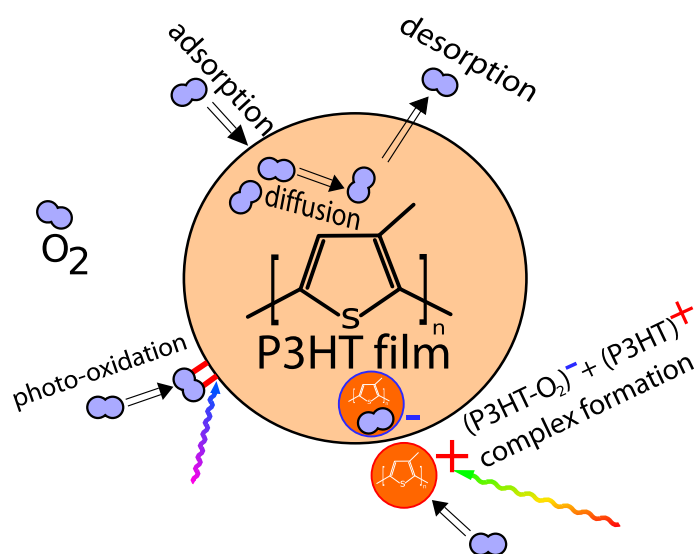


Figure 5.14: Depiction of irreversible and reversible interactions of P3HT with oxygen.

5.3.1 Introduction

Conjugated polymers have received considerable attention as materials for the fabrication of organic electronics and photovoltaic devices due to their remarkable semi-conducting and optoelectronic properties and the possibility to process devices from solution [3, 78]. For solar cells, being exposed to harsher conditions than many other device types, understanding the impact of different environmental influences is crucial to increasing the longevity of the cells [79]. The performance of a bulk heterojunction solar cell is determined not only by the energetic matching of donor and acceptor materials, but also by defect states hindering proper charge separation and extraction. Previous studies of oxygen-induced defect states in polymer devices show that charge carrier mobilities decrease by orders of magnitude upon exposure to air [60, 61]. Abdou et al. [80] noted that under illumination, P3HT forms a weakly bound charge transfer (CT) complex with oxygen. Due to the low spectral resolution in X-band EPR (9.4 GHz), the assignment of the EPR signal to P3HT⁺ polarons or (P3HT:O₂)_{CT}⁻ CT complexes remained elusive. Furthermore, Lüer et al. [81] found partially irreversible photoluminescence (PL) quenching of P3HT and attributed the origin to the quenching of singlet excitons with charged complexes. The chemical reactions behind the irreversible effects were examined by Hintz et al. [82]. They showed that photo-oxidation happens primarily on the alkyl side chains, forming peroxide species, which in turn destroy the thiophene unit, but the initial phototoxicity attacking the side chain is still presumed to be governed by triplet photosensitization [83].

Our intention is to complete this picture by using the possibilities of magnetic resonance to investigate the excitation pathway leading to the attack of the polymer side chain. EPR facilitates monitoring of polarons and charged complexes *in situ* avoiding the detour over electric contacts. By using high frequency (HF) EPR at 275 GHz, we were able to separate the spectra of P3HT⁺ polarons and (P3HT:O₂)_{CT}⁻ complexes and clarify that standard X-band EPR shows the superposition of the two contributions as one line. Additionally, the measurement of PL intensity and its resonant change (Δ PL) using the EPR extension, PL-detected magnetic resonance (PLDMR), allowed us to determine the degradation-related variations of the polymers' triplet yield.

5.3.2 Experimental Details

PL

Photoluminescence spectra were recorded according to the setup described in Chapter 4.3. Samples were spin-cast from solution onto sapphire substrates.

Sample Preparation

Samples in EPR tubes were prepared from the conjugated polymer P3HT and the soluble fullerene-derivative PC₆₀BM as described in Chapter 4. After evaporation of the solvent (chlorobenzene), the samples were annealed for 10 min at 140°C. The P3HT sample tube stayed connected to the vacuum pump with an optional inlet valve for ambient air during the whole measurement cycle. The sample tube containing P3HT:PC₆₀BM (weight ratio 1:1) was sealed under vacuum with a blow torch.

X-Band EPR and PLDMR

To obtain EPR curves and the evolution transients, the X-band EPR spectrometer described in Chapter 4 has been used. Illumination was provided by a 532 nm DPSS laser arriving in the cavity on a sample-spot of roughly 4 mm in diameter with 80 mW, resulting in an intensity of ~ 600 mW/cm². The PL intensity of the sample was recorded with a silicon photodiode behind a 550–1000 nm filter mounted to the rear access of the EPR cavity. The time-dependent EPR measurements were performed at room temperature, and the magnetic field was set to a value corresponding to the g -factor $g = 2.0014$ at the first derivative peak of the P3HT signal and stabilized by a field-frequency lock unit. The g -factor was calibrated as discussed in Chapter 4.2.

For PLDMR, the setup described in Chapter 4.2.3 was used. The microwaves amplified by a solid state amplifier arrive in the cavity with a power of ~ 60 mW. Instead of the microwave absorption, the variation of PL intensity (Δ PL) due to resonant microwave irradiation was recorded. The measurements were performed with a lock-in amplifier, referenced by switching the microwave radiation on/off with ~ 4 kHz. All PLDMR measurements shown here were recorded at $T = 10$ K.

HFEP

The HFEP measurements were performed at room temperature with the resonant conditions 275 GHz / 9.8 T. Lock-in detection using field-modulation was applied in a similar way as in the X-band setup. Further experimental details are given elsewhere [84, 85]. For these measurements, P3HT was dissolved in dry toluene by stirring it at 60°C for 1 h. Then the solution was stirred at room temperature for one week, whereby the capping of the vial was removed to allow the toluene to evaporate. Care was taken to prevent exposure of the P3HT polymer to air by keeping the material in a glove-box during the sample preparation. The resulting P3HT powder was then inserted in a small diameter quartz tube and mounted into the 275 GHz cavity.

5.3.3 Results

EPR

Figure 5.15 shows the influence of light and air on the X-band EPR signal of P3HT recorded at room temperature without illumination. The initially very weak signal (1) is probably caused by residual impurities and can be ignored for further analysis. This signal is not caused by metallic catalysts, since those signals would usually be observed at much higher g -factor (low field region), and no additional signals have been found for these batches. Upon exposure to light *or* air (2) the signal rises very slightly. Only with the combined exposure to air and green laser (532 nm) illumination over 1 h can a substantial increase of the EPR signal be observed (3). This signal is persistent; the spectrum has been recorded in the dark after illumination. It can be completely removed (4) after an additional vacuum annealing step for 10 min at 140°C.

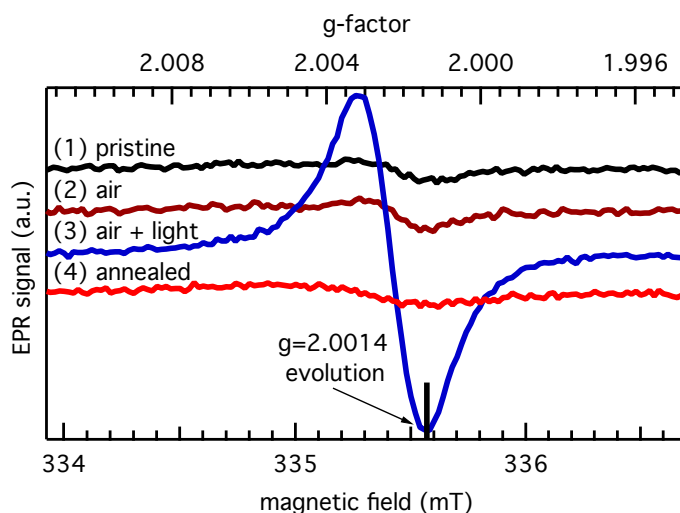


Figure 5.15: X-band EPR spectra of P3HT taken at 295 K without illumination: (1) as prepared in vacuum, (2) in air, (3) after air and light exposure (1 h), (4) after additional annealing for 10 min at 140°C in vacuum. The arrow points to the g -factor at which the evolution measurements were recorded (see Figure 5.19).

Abdou et al. [80] explained this rise of the EPR signal by the formation of oxygen-induced CT complexes. The spectral shift in EPR they showed can not be confirmed with the data presented here. Also, the reported intense signal of pure P3HT in vacuum is not in accordance with the vanishing weak initial signal in the pristine sample (see Figure 5.15 (1)). Possibly, the P3HT presently available is of higher purity than was available in 1996. Due to the low spectral resolution of X-band EPR, the assignment of the signal to CT complexes is rather ambiguous and needs further investigation.

HFEPR

To clarify the assignment of the observed single EPR line at X-band (9.4 GHz) to the proposed paramagnetic species, 275 GHz EPR experiments have been carried out at room temperature. Figure 5.16 represents the result of the HFEPR experiment on an illuminated P3HT sample. The two observed components are thought to be the EPR signals of the pair formed by P3HT⁺ and the (P3HT:O₂)_{CT}⁻ complex. From the comparison of the measured EPR curve with the simulated EPR spectrum of *g*-anisotropy-broadened EPR lines, it is concluded that the curve originates from at least two paramagnetic species A and B. In Figure 5.16, the principal axes of these species A and B are indicated. Due to the extremely small difference in the *g*-tensors, we have no means to attribute species A to P3HT⁺ and B to (P3HT:O₂)_{CT}⁻ or vice versa.

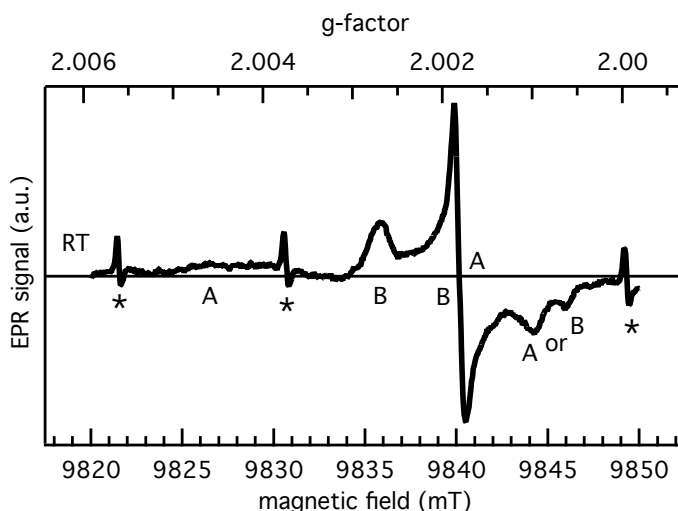


Figure 5.16: The HFEPR signal at 275 GHz of an illuminated P3HT sample at room temperature. Symbols A and B indicate the principal axes of the *g*-tensors of two paramagnetic species thought to be P3HT⁺ and (P3HT:O₂)_{CT}⁻ or vice versa. The asterisks (*) indicate signals of Mn²⁺ ions serving as *g*-markers.

The P3HT sample was subsequently subjected to several treatments (similar to the experiments shown in Figure 5.15) at room temperature, and the effect was monitored on the 275 GHz EPR signals. First, the sample was kept in the dark in a gaseous helium atmosphere and the EPR signal was recorded. Then, still in the gaseous helium atmosphere, the sample was exposed to light from a Hg arc, and an identical EPR signal was observed as in Figure 5.16. Exposure to air without illumination did not affect the signal. A considerable increase was observed when the sample was exposed to light and air, and both signal contributions showed the same increase in intensity. This indicates that the formation of both P3HT⁺ and (P3HT:O₂)_{CT}⁻ is a coupled process, and that the stoichiometric ratio is 1. Finally, when subsequently keeping the sample in the dark,

5 Results

the signal did not change appreciably at room temperature. The experiments show that it is the combined effect of light and air (oxygen) that causes the generation of the two paramagnetic species. In X-band EPR, the superposition of both contributions is measured as one signal.

EPR of P3HT:PC₆₀BM blends

Figure 5.17 shows the X-band EPR spectra of a P3HT:PC₆₀BM 1:1 blend at 100 and 295 K. At low temperatures, the typical well-known spectrum of the two overlapping signals of P3HT⁺ polarons and PC₆₀BM⁻ anions can be observed [58, 62, 77] (also see Chapter 5.1). However, at room temperature, only a marginal signal at $g = 2.002$ can be detected, showing no illumination dependence, and can thus be assigned to residual impurities similar to the EPR signal observed in Figure 5.15 (1). In other words: The PC₆₀BM⁻ anions and especially the P3HT⁺ polarons can not be observed with standard EPR methods at room temperature. This is caused by the fast recombination of these charge carriers at room temperature. This is caused by the fast recombination of these charge carriers at room temperature [62, 86]. The fact that they can be observed as dedicated signals at lower temperatures stems from strong charge localization, i.e. trapping of charges in separate domains of the blended materials. This hinders recombination and therefore prolongs the charge carrier lifetime enormously, yielding the observed EPR spectra.

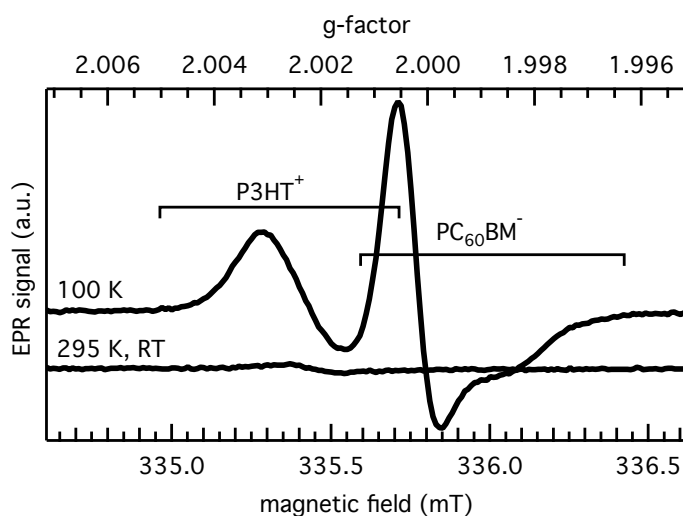


Figure 5.17: X-band EPR spectra of a P3HT:PC₆₀BM 1:1 blend taken at 100 and 295 K under illumination. The partially overlapping signals from P3HT⁺ polarons and PC₆₀BM⁻ anions at 100 K are marked. Almost no signal can be observed at 295 K.

Thermal annealing of the blend samples does not change the observed lineshapes at low temperatures. However, the signal intensity decreases dramatically upon annealing due to small-scale phase separation and the resulting loss of interface surface. [63, 77] The residual signal observed at room temperature (Figure 5.17) does not change substantially.

After comparison of the spectra shown in Figures 5.15–5.17 the following conclusion can be drawn: The oxygen-induced P3HT⁺ polaron and (P3HT:O₂)_{CT}⁻ complex demonstrate very slow recombination compared to P3HT:PC₆₀BM blends. In fact, the created paramagnetic species are persistent at room temperature and do not recombine readily after switching off the illumination. Thus at least one of the partners (P3HT⁺/(P3HT:O₂)_{CT}⁻) must be a trap state at room temperature hindering recombination.

PL of P3HT under Oxygen Exposure

For all samples studied, typical P3HT PL could be observed (see Figure 5.18). Upon addition of PC₆₀BM or oxygen, these spectra were partly quenched, yet the spectral shape remained identical. This demonstrates that no other radiative recombination processes were enabled, and the singlet excitons responsible for PL of P3HT were unaffected. Thus the PL intensity is a proper scale to quantify singlet quenching in P3HT under oxygen exposure.

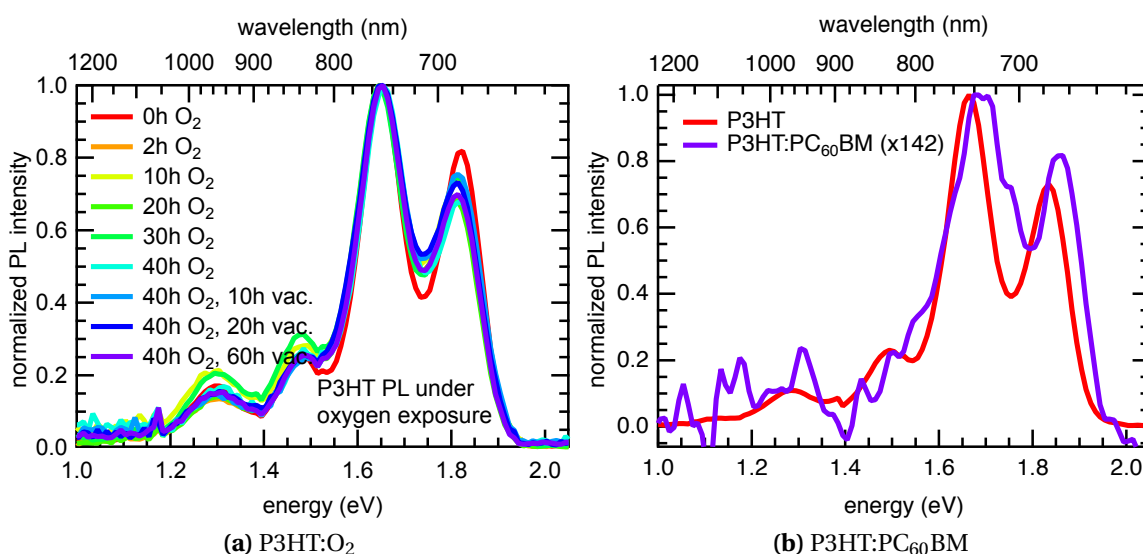


Figure 5.18: Normalized PL-spectra recorded at 30 K of (a) P3HT after prolonged exposure to first oxygen and then vacuum and (b) P3HT:PC₆₀BM together with pristine P3HT for comparison.

EPR/PL long-term evolution

After clarifying the origin of the EPR signals in oxygen-exposed P3HT, we studied the temporal evolution of this signal with X-band EPR and simultaneously measured the PL intensity as shown in Figure 5.19.

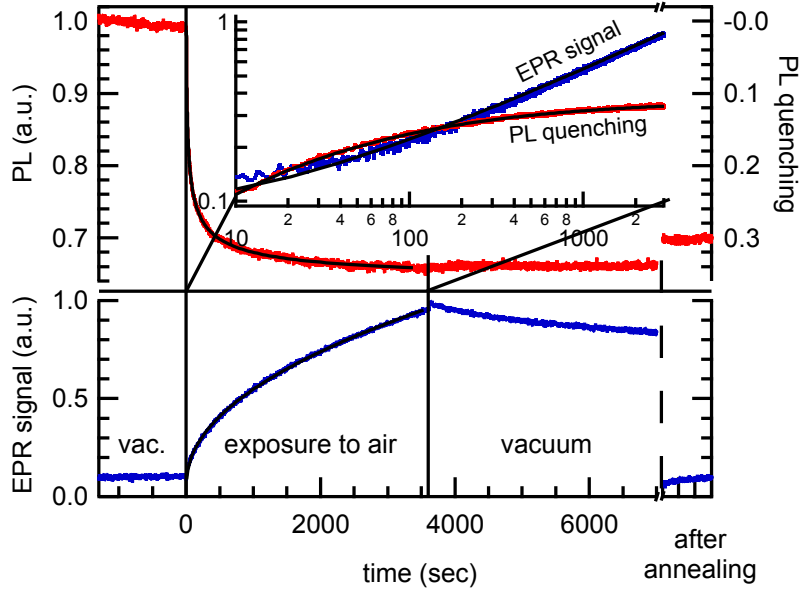


Figure 5.19: The evolution of the EPR signal ($g = 2.0014$ peak), the PL and the PL quenching ($=1-PL$) at room temperature. Before 0 s, the sample was illuminated under vacuum. From that point on, air was introduced. This led to a continuing power law rise of the EPR signal and a decay of the PL. The inset shows a log–log plot of this time-range. From 3600 s on, the sample was evacuated, which led to slow decay of the EPR signal, but no change for the PL. After annealing, the PL recovered slightly, while the EPR signal was removed completely.

Before ($t < 0$ s), the sample was in vacuum under constant illumination. PL and EPR signals changed only slightly in the time scale of hours, as long as the sample was exposed either to air (not shown) *or* light. We surmise that oxygen was desorbed into the P3HT, but without light any interaction was strongly suppressed, and the oxygen could be removed by evacuating the sample. This is consistent with the theoretical estimates of Lu and Meng [87], who postulate a highly oxygen-pressure-dependent hole-doping of P3HT in the dark. When using environmental air at atmospheric pressure (as we did), we would expect only marginal doping without light.

The situation changes under concurrent light and air exposure from $t = 0$ s on: the EPR signal rises, and the PL is quenched by 35 % within 1 h. This evolution is independent of the gas diffusion into the sample bulk, which was confirmed by reversing the exposition order to first oxygen and then light (not shown). A diffusion time less than

5.3 (Ir-)Reversible P3HT:O₂ Interactions Studied by Spin-Sensitive Methods

1 s can be estimated from a layer thickness of $\approx 1 \mu\text{m}$ and a diffusion constant for O₂ in P3HT films of $1.2 \mu\text{m}^2\text{s}^{-1}$ (from Ref. [80]) or even $0.15 \mu\text{m}^2\text{s}^{-1}$ (from Ref. [81]).

From 3600 s (1 h) on, the sample was evacuated again. This did not result in a recovery of the PL, but the EPR signal slowly decreased within hours. Applying a thermal annealing step (140°C for 10 min) while still evacuating the sample removed the EPR signal, whereas the PL recovered only slightly. This means that the weak physical adsorption of molecular oxygen to P3HT is fully reversible when reducing the oxygen-pressure by evacuating. The annealing assists this process by creating additional thermal motion of the polymer. The fact that the PL remained quenched, although EPR measurements state that all CT complexes were removed, implies that another interaction process is responsible for the PL quenching. We therefore conclude that the irreversible part of the PL quenching is due to photo-oxidation of the polymer.

The inset in Figure 5.19 shows the time range of 0–3600 s (light and air exposure) in a log–log plot for the EPR signal and the PL quenching (=1-PL). The different curve shapes are obvious. The EPR enhancing and the PL quenching occur at different time scales, supporting the assumption of two separate interaction processes between P3HT and oxygen. The EPR signal evolution can be fitted with a power law ($EPR\ signal = c \cdot t^\alpha$) which is in accordance with former results on radiation-induced (in our case, laser light) defect production [88]. We found $\alpha = 0.477$ which should be dependent on the experimental conditions (partial O₂-pressure, light intensity). The PL quenching was fitted using an equivalent formulation of the Hill Equation¹ [89, 90].

$$PL\ quenching = PL_{start} + \frac{PL_{end} - PL_{start}}{(\tau/t)^n + 1} \quad (5.17)$$

We found $\tau = 21.7$ s which is also dependent on experimental conditions. More interesting is the exponent $n = 0.547$ describing the affinity of a macromolecule (e.g., P3HT) to undergo a chemical reaction with potential ligands (e.g., O₂). For $n > 1$, a positively cooperative reaction is to be assumed, i.e., once one ligand is bound to the molecule, its affinity for other ligand molecules increases. For $n = 1$, no change in affinity is to be observed. If $n < 1$, the affinity of the molecule decreases during the ongoing interaction with further ligands. This seems to be the case for photo-oxidation of P3HT. Already degraded polymer-segments have a reduced affinity for further interaction with oxygen.

Regarding the reversibility of the oxygen doping processes, our results contradict the findings of Liao et. al.: [91] They claim that the doping is reversible when facilitated with visible light, and only UV excitation leads to irreversible photo-oxidation. Our results concerning the PL quenching show irreversible degradation already with green

¹Jan. 2013: [http://en.wikipedia.org/wiki/Hill_equation_\(biochemistry\)](http://en.wikipedia.org/wiki/Hill_equation_(biochemistry))

5 Results

excitation light, however with a rather high light intensity of $\sim 600 \text{ mW/cm}^2$. Lürer et al. [81] attributed the PL quenching mainly to the formation of CT complexes, while we show that even after complete removal of these complexes, the PL remains quenched. Hence, only the slight reversible recovery of the PL after the thermal annealing might stem from PL quenching due to CT complexes, while the irreversible part is photo-oxidation.

PLDMR

The open question is the connection between the reversible CT complex formation and irreversible photo-oxidation, and hence the destruction of the polymer. To answer it, we investigated the triplet generation properties of P3HT in relation to oxygen degradation. For P3HT it is well-known that, without an electron-accepting moiety, a significant part of generated singlet excitons undergoes an intersystem crossing (ISC) to the energetically favorable triplet state [92]. Other contributions to the triplet yield are the recombination of non-geminate polarons [36, 93] or (in P3HT:fullerene blends) electron back transfer from the fullerene LUMO level to the P3HT triplet level (if energetically possible) [94].

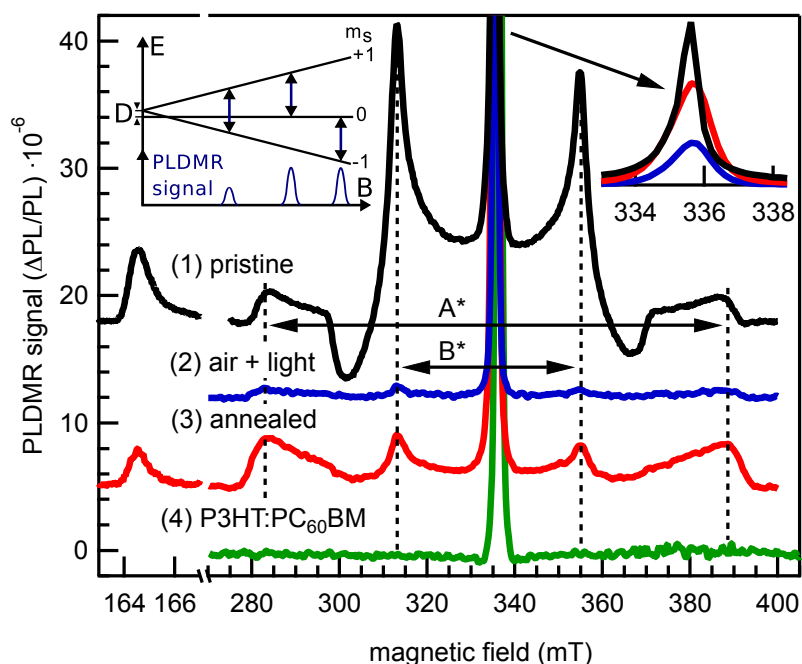


Figure 5.20: PLDMR spectra taken at 10 K in vacuum. (1–3) P3HT: (1) as prepared, (2) after air and light exposure, (3) after additional annealing for 10 min at 140°C in vacuum. (4) P3HT:PC₆₀BM 1:1. The right inset shows a zoom on the central peak (P3HT 1–3) and the left inset shows the generation mechanism of the measured triplet pattern. Arrows A* and B* indicate possible triplet orientations.

5.3 (Ir-)Reversible P3HT:O₂ Interactions Studied by Spin-Sensitive Methods

Figure 5.20 shows PLDMR spectra of P3HT and P3HT:PC₆₀BM 1:1. The $\Delta m_s = \pm 1$ and the first-order forbidden $\Delta m_s = \pm 2$ half-field transition can be observed. The central peak in these spectra originates from non-geminate polaron pairs or can also be referred to as “distant triplets” with little or no zero-field splitting (see Chapter 3.7). The pristine curve (1) shows a distinct powder pattern observed for most thiophene-based polymers. Zero-field splitting D is responsible for the wing-like appearance of the powder pattern and is also correlated with the spatial extent of the corresponding triplet state (see Chapter 3.6). The different peaks result from the P3HT crystalline orientation in relation to the external magnetic field. We can distinguish between orientations A* and B*.

Note that the PLDMR signal is normalized to the photoluminescence ($\Delta PL/PL$), so the reduction of the total PL intensity has no influence on the overall signal height in PLDMR.

The triplet exciton patterns in the pristine sample (Figure 5.20 (1)) are almost completely quenched after exposure to oxygen (2). The initially generated singlet excitons are separated before a possible ISC can occur, as oxygen is a very good electron acceptor [95]. Similar shape of the PLDMR spectrum was observed in P3HT:PC₆₀BM blends (4), where the CT from polymer to fullerene is the dominant process and therefore completely prevents ISC to the triplet state. Yet the PL quenching is usually incomplete, leaving a small fraction (< 5 %) of the P3HT PL, enabling the application of PLDMR technique to blends.

After removing the adsorbed oxygen by evacuating and annealing (see the EPR section 5.3.3), only chemically bound oxygen remains, which is responsible for the irreversible PL quenching. In the PLDMR signal, the reduction of the overall signal height (3) in comparison to the pristine PLDMR (1) is attributed to the triplet generation in P3HT being a strongly multimolecular process [32, 35]. In a degraded polymer, the intact thiophene units have less other intact units in their vicinity, preventing triplet generation.

We interpret that the polymer chain segments which were not photo-oxidized can generate triplet excitons (orientation A*) as soon as the the electron accepting CT complexes are removed, while the triplet exciton (orientation B*) signal remains weaker due to a part of the polymer being permanently destroyed by photo-oxidation.

5.3.4 Discussion

Figure 5.21 shows the proposed oxygen-related degradation process scheme in a conjugated polymer, P (e.g., P3HT). The polymer (P) can be excited by visible light ($h\nu exc.$) yielding a singlet exciton ($^1P^*$). This exciton can recombine to the ground state by radiative (PL) and non-radiative ($non r.$) processes. Another possibility is the relaxation of the singlet via intersystem crossing (ISC) to the energetically favorable triplet state ($^3P^*$) [92], which can also be populated via alternative routes, e.g., via non-geminate polarons (not shown) [36, 93]. Under certain conditions, the formation of triplets in polymer:fullerene blends is also possible as it depends on the relative energy positions of polymer triplet excitons and the fullerene LUMO level [94]. Formed triplet excitons located on the polymer can then non-radiatively ($non r.$) relax to the ground state. Additional reactions emerge upon introduction of molecular oxygen, which has a triplet ground state configuration (3O_2). These reactions are both reversible (shown in the red box) and irreversible (green box) and discussed in the following.

The irreversible reaction starts by energy transfer (ET) of the polymer triplet to the triplet oxygen to generate excited singlet oxygen ($^1O_2^*$) [95]. This is the reactive species for photo-oxidation of the polymer (depicted by the *oxidation* to “ PO_2 ”) that irreversibly quenches PL and bleaches the UV-VIS absorption by attacking the polymer [82, 83].

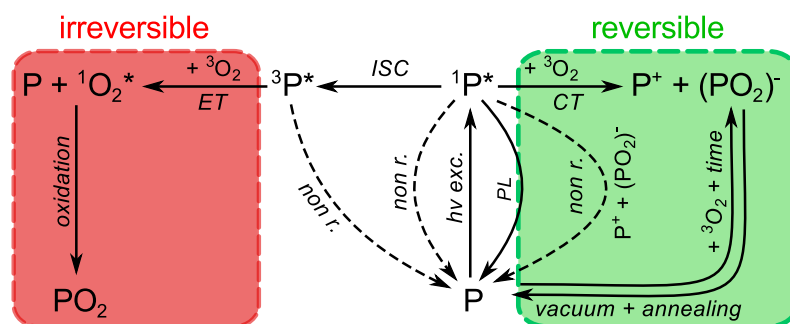


Figure 5.21: Oxygen related degradation processes in a conjugated polymer, P. Details are given in the text.

Another possible mechanism for the production of singlet oxygen is presented in the literature: optically excited P3HT:oxygen complexes, which can in turn relax to singlet oxygen states [96]. However, this process cannot be confirmed by the results presented in this work, since the PL quenching saturates upon formation of CT complexes (see Figure 5.19). Recent results by Guerrero et al. have shown that this is probably the case because the absorption of the P3HT:oxygen complex is red-shifted significantly in comparison to the regular P3HT absorption [97]. therefore this degradation reaction cannot be started by green laser illumination (532 nm).

5.3 (Ir-)Reversible P3HT:O₂ Interactions Studied by Spin-Sensitive Methods

The reversible reaction route shown is *CT* from the polymer to oxygen to create positively charged polarons (P^+) and weakly bound CT complexes: $(PO_2)^-$. The creation of free charge carriers (P^+ / P^-) via singlet excitons is also possible, which then react with oxygen, yielding the same result (not shown) [87]. This direct creation of free charge carriers is only relevant for high-energy photons (blue – UV) as can be seen by the external quantum efficiency of a P3HT diode [98]. The polarons and CT complexes formed give rise to the observed EPR signals in Figures 5.15 and 5.16 and can be removed slowly in *vacuum* at room temperature (see Figure 5.19: $t > 3600$ s) or rapidly by additional *annealing* at 140°C (see also Figure 5.15). This reversible doping also occurs very slowly in the dark at room temperature as shown by EPR measurements and proposed by Lu and Meng [87], but proceeds orders of magnitudes faster upon excitation ($h\nu exc.$) of the polymer.

The oxygen-induced doping in organic solar cells is responsible for a loss of short circuit current (J_{SC}) and reducing the overall mobility of charge carriers, while photo-oxidation of the devices also leads to a reduction in fill factor (FF) and open circuit voltage (V_{OC}) [61].

Additionally, the formation of polarons and CT complexes opens another non-radiative recombination channel (*non r.* / $P^+ + (PO_2)^-$) for singlet excitons back to the ground state ($^1P^* \rightarrow P$) [81]. This is the observed reversible part of the PL quenching and blocks the less favorable *ISC* to the triplet state. Thus the formation of polarons and CT complexes prevents further irreversible degradation by triplet-sensitized singlet oxygen. This can be observed in Figure 5.19: with increasing EPR signal, the reduction of the PL intensity stops almost. This is backed up by the quenched triplet generation found in PLDMR (see Figure 5.20 (2)).

A similar protection effect through quenching of the triplet generation was seen in poly(phenylene vinylene) (PPV):PC₆₀BM blends, which are also more robust against oxygen exposure than pure PPV [99, 100]. This is in accordance with the presented PLDMR results, showing that in P3HT:PC₆₀BM blends, no triplets are generated (see Figure 5.20 (4)) and thus would also prevent the creation of singlet oxygen over triplet photosensitization. However, this protection by quenching of the triplet production is not present in all polymer:fullerene blends and might be problematic, especially for new high-voltage blend combinations [94].

5.3.5 Conclusion

In conclusion, we demonstrated that at least two different mechanisms are responsible for the photodegradation of P3HT. With high-resolution EPR techniques, we have shown that the formation of CT complexes, previously proposed by Abdou et al., is fully reversible and is only partially responsible for the PL quenching. Instead, the dominant PL quenching mechanism is the irreversible photo-oxidation of the polymer by triplet-photosensitized singlet oxygen, as follows from the PLDMR. Important for the organic photovoltaic (OPV) applications is that the polymer degradation processes become significant only when it is exposed to light. Dark oxygen exposure can be reversed by annealing in a vacuum. These results are supported by the PLDMR measurements, which show a suppression of the triplet generation by polarons and CT complexes. In polymer:fullerene blends, a protective effect of CT complexes and fullerenes bypassing the formation of singlet oxygen and hence the degradation of the polymer can be anticipated.

5.4 Temperature-Dependent Charge Separation Dynamics in P3HT:PC₆₀BM

Abstract

The time-resolved EPR technique (trEPR) is a powerful tool to study the temporal evolution of charge transfer complexes (CTC), photo-generated at the donor:acceptor interface in organic bulk heterojunctions, such as P3HT:PC₆₀BM. Right after the photo-excitation by a ns laser pulse, spin-coupled radical pairs (SCRPs) are formed in the system, showing themselves as an alternating pattern of microwave absorption and stimulated microwave emission (E/A/E/A). At longer timescales the pattern converts into a pure absorptive one (A/A), due to free charges in the blend and thermalization of the spin system. Temperature-dependent trEPR spectra were recorded in order to study the separation dynamics as well as the spin thermalization. We found that at cryogenic temperatures of 50 K and below, most charges do not separate spatially but remain closely bound across the interface, evident by their persistent strong spin interaction.

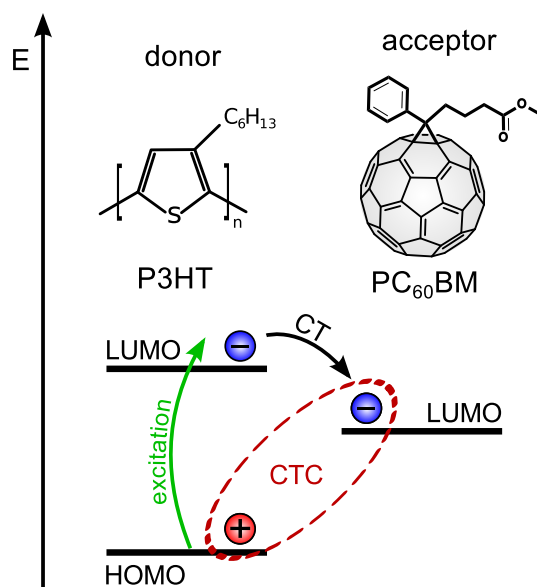


Figure 5.22: Depiction of the involved energy levels of the donor P3HT and the acceptor PC₆₀BM. After the initial charge transfer (CT), a hybrid state of the donor HOMO and the acceptor LUMO – a so-called charge transfer complex (CTC), is formed.

5.4.1 Introduction

After the primary photo excitation in bulk heterojunction organic solar cells, the resulting singlet exciton needs to be split at the donor:acceptor interface. This charge transfer process has been reported to occur within tens of femtoseconds and is thus much more efficient than any competing loss mechanism [3, 55, 101]. However, there has been a lot of discussion in literature, whether this results directly in spatially separated non-interacting charge carriers that can be referred to as free polarons [102, 103], or if the charges form an intermediate charge transfer complex (CTC) at the heterojunction [29, 104] as depicted in Figure 5.22. In this context common literature often refers to them as charge transfer state (CTS) and charge separated state (CSS). Recent results for solar cells composed of thiophene-type polymers and soluble C₆₀ fullerenes point out that CTCs are a typical intermediate state at least in this class of materials [105]. The CTCs can be distinguished between being in a short-living singlet-type state or a longer-living triplet-type state [104, 106, 107]. The fast-recombining singlet-type CTCs are here a loss mechanism effectively limiting the power conversion efficiency of solar cells. Instead triplet-type CTCs are favorable, because their lifetime is long enough to enable spatial separation of the charge carriers.

From an EPR point of view, CTCs can be described in the framework of spin-coupled radical pairs (SCRPs, see Chapter 3). This species is an ideal candidate to be studied by means of time-resolved EPR, since this method enables direct access to coupling parameters and dynamics [28, 108, 109, 110]. Early work by Pasimeni et al. showed that in bulk heterojunctions of thiophene oligomers with C₆₀-derivatives, CTCs can be observed as characteristic spectral fingerprint by trEPR [111, 112]. Directly after a ns laser flash, a signal with strong spin polarization emerges, consisting of four alternating emissive and absorptive lines (E/A/E/A). The spectrum exhibits perfect point symmetry about the center of the spectrum. This symmetry and the E/A/E/A polarization are proof of the initial $m_s = 0$ spin polarization (see Section 3.5). The $m_s = 0$ energy levels |2⟩ and |3⟩ are populated, while the triplet levels |1⟩ and |4⟩ are empty. The spectrum was reproduced by simulations to extract the exchange and dipolar interaction constants J and D , from which the inter-radical separation was specified to be 2.7 nm across the donor:acceptor interface (compare Equation 3.16 in Section 3.4.1). Recently we presented results on P3HT:PC₆₀BM blends that showed similar spectral features at 1 μs [29] after the laser flash. This spectrum transforms to two absorptive peaks at longer time delays and fits perfectly with the spectrum recorded by cwEPR. This cw spectrum has previously been assigned to free non-interacting polarons [57, 62] and thus we provided proof that CTCs are an intermediate state en route to photo current in organic bulk heterojunctions.

In this work we study the CTC's spectral fingerprint in trEPR over a broad temperature range. We show that at temperatures of 50 K and below, the charges neither separate nor move away from the donor:acceptor interface over time. Instead, the still-coupled spin system thermalizes and in the end, the charges recombine geminately. Furthermore the possibilities to simulate the SCRP spectrum are discussed with respect to the manifold of free parameters that render this approach difficult.

5.4.2 Experimental Details

The used materials are the conjugated polymer P3HT and the soluble fullerene derivative PC₆₀BM. Details are given in the according Chapter 2. The materials were solved in chlorobenzene at a concentration of ~20 mg/ml and blended at a mixing ratio of 1:1. 200 µl of the solution were poured into an EPR tube and sealed off after vacuum drying.

Continuous wave and time-resolved EPR spectra were recorded at cryogenic temperatures under cw and pulsed laser illumination (532 nm), respectively. The energy per pulse for the trEPR measurements was 2 mJ. Details are given in the main experimental Chapter 4.

5.4.3 Results and Discussion

Figure 5.23 shows a spectral series taken at different time delays after the laser flash for 50 K. For better overview of the temperature dependent measurements (10 K – 160 K), the recorded transients are also converted to two-dimensional matrices (time vs. magnetic field) and displayed in color-coded surface plots (see Figure 5.25). Here, blue color stands for microwave absorption, while red corresponds to stimulated microwave emission (white = no signal). The 2D plot for 50 K shown in Figure 5.25b is the full data set of the spectra shown in Figure 5.23. For all plots, the spectrometer's time resolution of ~200 ns is evident by the flat spectrum (white area) before the actual trEPR signal appears.

At early times (0.2–1 µs) the spectra consist of the previously described four peaks with E/A/E/A polarization pattern (red/blue/red/blue in the 2D plots). This four-peak fingerprint of SCRPs is clearly visible around 1 µs for 10 K and 50 K and still detectable at 100 K. The overall shape and width of this spectrum (Figure 5.23) is consistent with literature [111, 112] and our previous results [29], showing the direct comparability of the discussed data set.

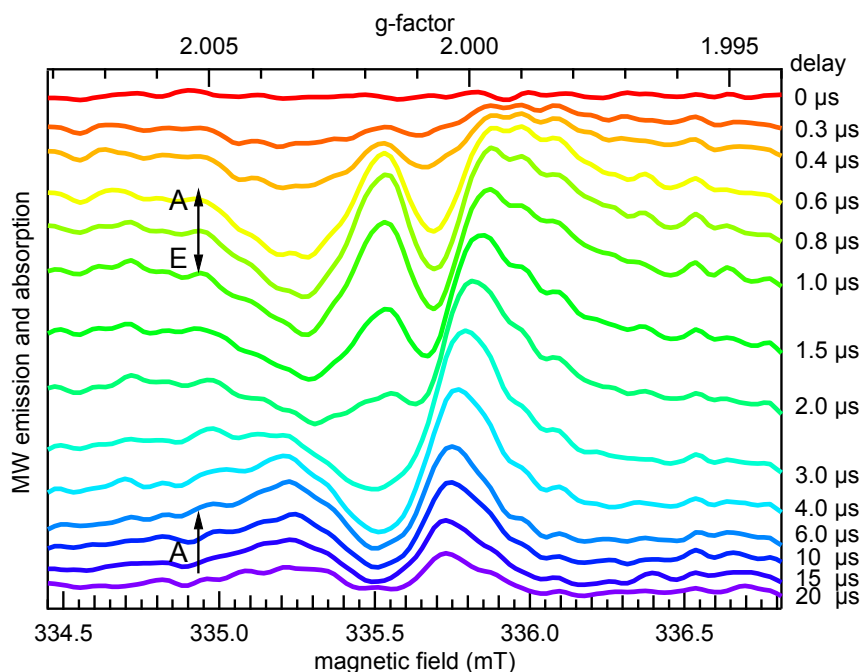


Figure 5.23: trEPR spectra taken at 50 K for different delays after the laser pulse showing the transition from a SCRP (four lines with E/A/E/A polarization) to a signal consisting of two absorptive lines (A/A).

Spectral Simulations

Figure 5.24 shows a trEPR spectrum taken $0.8 \mu\text{s}$ after the laser flash, recorded at a temperature of 50 K. The spectrum is taken from the spectral series shown in Figure 5.23. The spectrum has been fitted tentatively using the EPR simulation environment EasySpin [48]. The angular dependence of the dipolar interaction is considered, resulting in the experimentally observed powder patterns. For the presented simulations a parameter-set consisting of the coupling constants J' and D' , as well as the g_{iso} values of P3HT^+ ($g_{iso} = 2.00225$) and $\text{PC}_{60}\text{BM}^-$ ($g_{iso} = 2.00005$) were used according to the values from Table 5.3 in Chapter 5.2. While the full set of g -tensors for the separated charges is available, we refrained from using them, since the CTC wave function certainly deviates. Therefore $g_{iso} = \frac{1}{3}(g_{xx} + g_{yy} + g_{zz})$ is a good-enough approximation. The two linewidth-parameters used for the simulations are in the range of (0.1–0.4) mT. In EasySpin, the spin-interactions are defined as an electron–electron interaction vector: $\mathbf{J}_{ee} = J \begin{pmatrix} 1 \\ 1 \\ 1 \end{pmatrix} + D \begin{pmatrix} -1/3 \\ -1/3 \\ 2/3 \end{pmatrix}$. The resulting fit-values for two tentative simulations are shown in Table 5.4.

The acquired values for J' and D' are inconsistent and contradictory, yet both simulations fit the experimental data perfectly. The fact that a unique set of fitting parameters is not able to reproduce the experimental data has two reasons: First, the vast amount of parameters involved – and second, the poor spectral resolution of the ac-

quired spectra. The first point is even more serious, since not a single parameter set, but a distribution of parameters is responsible for the observed spectrum. For the expected inter-radical distance, a distribution of distances is to be expected due to the disordered nature of the used bulk-heterojunctions. Additionally, the four involved transitions most certainly have different line widths and spin relaxation dynamics in addition to a potential asymmetry due to g -strain. In conclusion, the attempt to fully simulate this kind of experimental trEPR spectrum and extract a meaningful set of parameters is ambiguous at least.

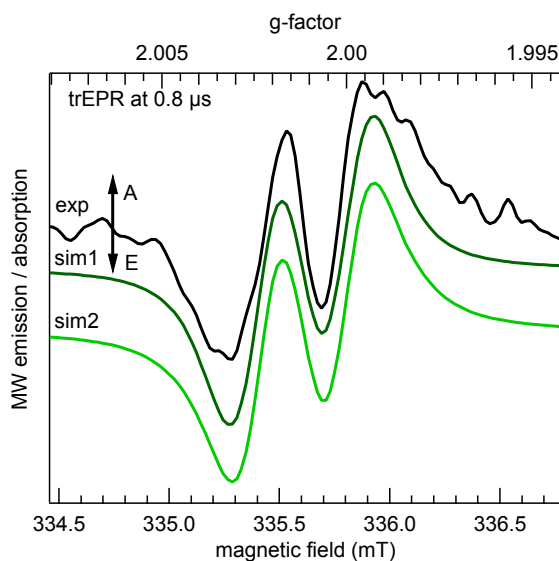


Figure 5.24: 50 K trEPR signal at 0.8 μ s taken from Figure 5.23 showing the typical E/A/E/A polarization of a SCRP with singlet precursor. Two tentative spectral simulations are shown for comparison.

spectrum	J' (mT)	D' (mT)	g_{iso} -values
sim1	0.084	-0.021	P3HT ⁺ : 2.00225 / PC ₆₀ BM ⁻ : 2.00005
sim2	0.027	0.032	P3HT ⁺ : 2.00225 / PC ₆₀ BM ⁻ : 2.00005

Table 5.4: Parameters of the tentative simulations sim1 and sim2 in Figure 5.24.

Despite these shortcomings it is evident that the presented spectrum is due to an intermediate SCRP, involved in the process of charge carrier generation in an organic solar cell. The significance of this fact is not diminished by the challenges of fully simulating the spectrum itself. Concerning the poor spectral resolution, it is to be expected, that a significant enhancement of time resolution and sensitivity can be achieved. The technical limitations are by no means fundamental and can be approved upon.

5 Results

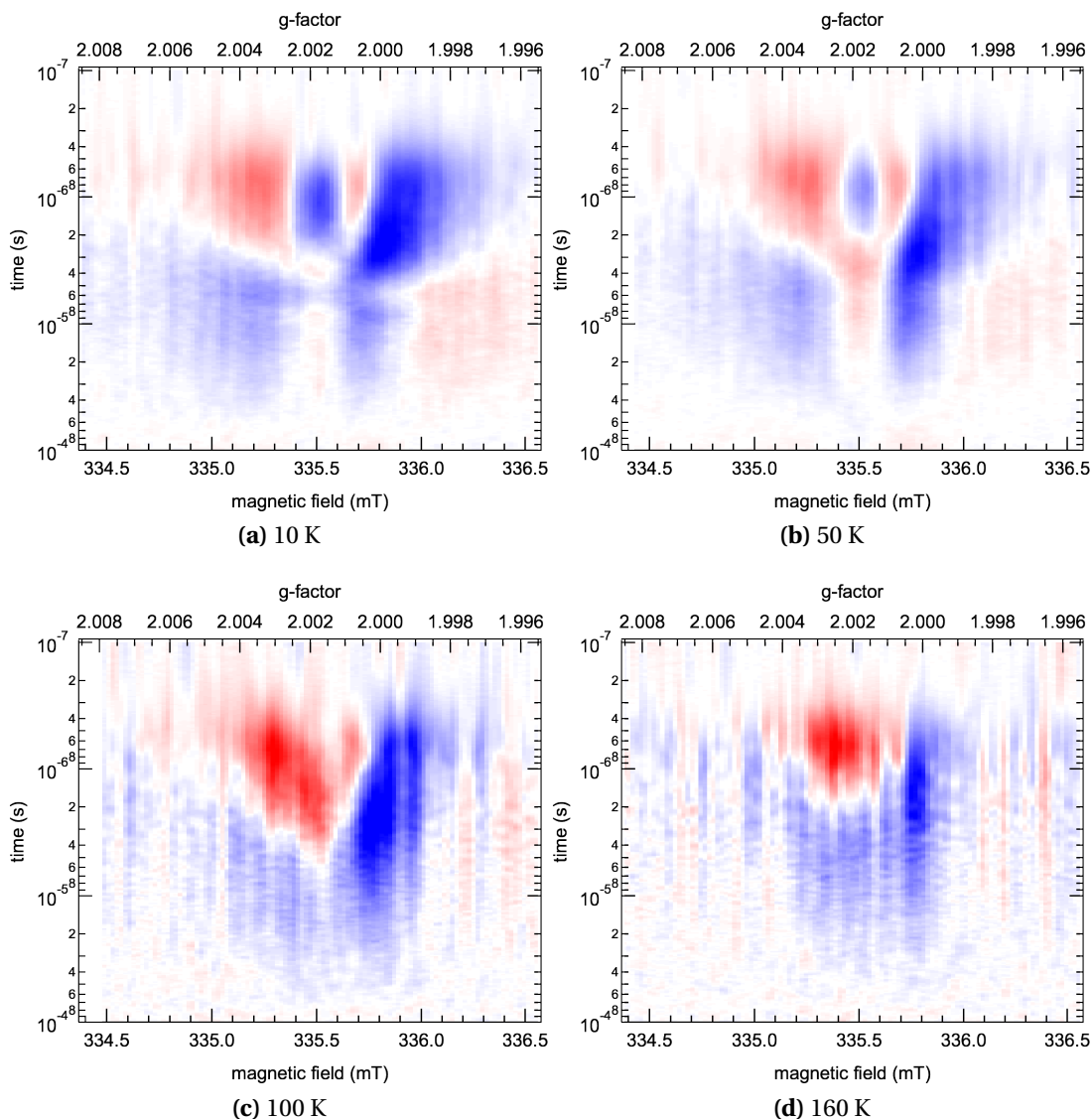


Figure 5.25: trEPR spectra taken at different temperatures with signals in microwave absorption (A – blue) and stimulated microwave emission (E – red). The temperature dependent change in spin thermalization time (end of microwave emission) and the transition from four lines with E/A/E/A polarization pattern to two absorptive lines (A/A) can be observed. The spectra are massively broadened at lower temperatures and even exceeding the recorded magnetic field range at 10 K.

Temperature Dependence

In the following microseconds the E/A/E/A spectrum and the microwave emission disappear. Instead, at later times ($>10 \mu\text{s}$), all spectra show two absorptive peaks (A/A). In the series of 10, 50 and 100 K the point in time, when the four-peak signal disappears and the two peak signal emerges, shifts to earlier times, i.e. from $3 \mu\text{s}$ at 10 K to less than $1 \mu\text{s}$ at 100 K. This is shown in Figure 5.26a together with the spin thermalization time. This is the point in time, when the microwave emission (red areas in the 2D plots) ends and is an upper estimate of the spin relaxation time T_1 . The microwave emission is especially pronounced and long lasting for lower temperatures. This is because of the temperature dependence of the T_1 time constant. At higher temperatures, the spin system relaxes faster towards thermal equilibrium.

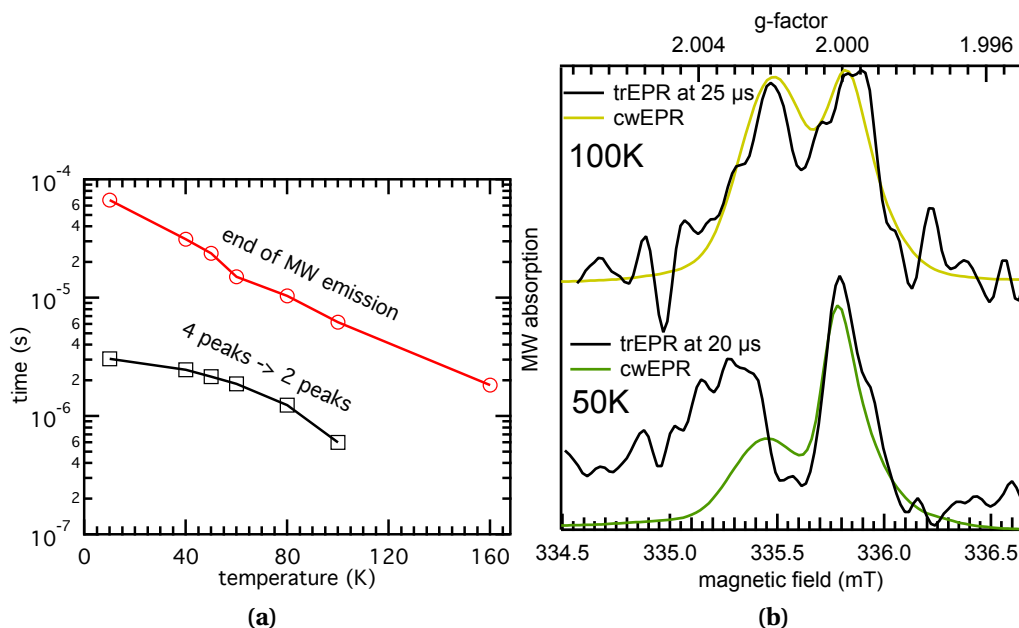


Figure 5.26: (a) Temperature dependence of the spin thermalization time (end of MW emission) and time for the spectral transition from four to two peaks. (b) Comparison of trEPR with integrated cwEPR spectra recorded under the same conditions. They overlap perfectly at 100 K, but the spectrum at 50 K is massively broadened.

The two-peak absorptive spectrum detected at longer delay times ($>10 \mu\text{s}$) was previously assigned to the formation of free non-interacting polarons in the blend [29]. Figure 5.26b shows the according trEPR spectra for temperatures of 100 K and 50 K. For comparison, integrated cwEPR spectra are superimposed that were recorded under the same conditions. As expected, the spectrum at 100 K is identical for both measurements, confirming our previous results: CTCs undergo spatial separation within

5 Results

several microseconds and can be detected as the EPR signals of electron and hole, localized on the fullerene and the conjugated polymer, respectively.

However, at 50 K the trEPR spectrum is massively broadened in comparison to the cwEPR spectrum. Therefore the previous argument for the creation of free polarons does not apply any longer for very low temperatures. The spectral discrepancy appears due to the fact that electron and hole still have strong spin coupling even at long delay times. This means the spin sublevels of the CTC just thermalized, but the charges did not separate to a distance, where the spin interaction is negligible. The two peaks at longer delay are actually four overlapping absorptive peaks of the SCRP (compare Figures 3.7 and 3.8 in Chapter 3.5). This signal is then decaying without further spectral change or narrowing (compare Figures 5.23 and 5.25b). Consequently, at very low temperatures most of the initially generated CTCs do not separate spatially at the donor:acceptor interface. Instead, the generated electron-hole pairs recombine geminately.

All of the observed signals disappear within 100 μs . Hence, most of the initially generated CTCs and succeeding polarons recombine in this time period. The remaining trapped charges are recombining very slowly and are detectable in cwEPR [63, 113]. trEPR is far less sensitive and persistent signals are usually hidden unnoticeable in the noise background.

The 2D plots in Figure 5.25 show massively wide CTC spectra at around 1 μs . Actually, they are even exceeding the recorded magnetic field range of ~ 2 mT at 10 K. Succeedingly, all spectra show a narrowing of the spectral width over time and for rising temperatures. Especially at 100 K and 160 K, the spectra are much narrower than at lower temperatures for each point in time. The spectral width of the CTCs can be explained as a function of the spin–spin coupling strength. The spectral separation of the two transition doublets of a SCRP is defined by $\Omega' = \sqrt{(J' - d')^2 + \Delta B^2}$ (note $d' < 0$), with ΔB being the spectral separation of electron and hole g -factors, while J' and d' are the spin coupling constants (see Chapter 3.4.3). Hence, strong coupling equals large $|J' - d'|$, which results in broader spectra.

For very low temperatures the charges do not separate but recombine directly, as discussed before. The spectral narrowing at early times is therefore either caused by a change in the inter-radical distance, or the closer pairs with stronger interaction are recombining first. At elevated temperatures (≥ 100 K), the initially broadened spectra collapse to the width of the cwEPR spectra, according to the formation of non-interacting polarons. This is also the case for the measurement at 160 K. The SCRP fingerprint is not observed and instead the initial signal is a narrow two-peak spectrum with E/A spin polarization. At this temperature the spectral width is in accordance with the forma-

tion of free polarons within the first microsecond. The E/A spin polarization is therefore implying that the P3HT⁺-polaron at $g = 2.002$ is initially in spin up polarization and emitting microwaves (red), while C₆₀⁻ at $g = 2.000$ is spin down (MW absorption, blue).

The temperature dependence of the point in time at which the spectrum of CTCs disappears, suggests it will be in the \sim ns regime for room temperature. This is in accordance with other models, that suggest a short separation time of charges at RT [104], or even negate the existence of CTCs for a time-resolution of several ns [103].

5.4.4 Conclusion

For future studies of CTCs in organic bulk heterojunctions it would be advantageous to employ higher microwave frequencies and magnetic fields. Both, because of sensitivity and spectral resolution as motivated in Chapter 3.3. Additionally, the time resolution of a trEPR setup is directly dependent on the spectrometer's microwave frequency (see Section 4.2.2). As evident by the presented spectra all these three parameters would need a serious improvement to enable a full spectral simulation of the initial CTC and the transition to spectra, observed at later delay times. Especially Q-band trEPR at 34 GHz would be ideally suited for this task, because this kind of EPR spectrometer works in principle identical to X-band spectrometers and thus enables the direct comparison of the recorded spectra [114]. Still, the full simulation of SCRIP spectra is ambiguous, because of the number of parameters involved and the fact, that there is not a single inter-radical distance, but probably a distribution of distances. All this leads to an averaging of the spectrum and requires serious consideration.

In conclusion, we have studied the temperature dependence of charge transfer complexes in P3HT:PC₆₀BM bulk heterojunctions by means of time-resolved EPR. Characteristic spectral patterns of CTCs are formed in the course of charge transfer from the polymer to the fullerene. These can be explained in the framework of spin coupled radical pairs and their transition into separated non-interacting polarons. We observed, that at temperatures of 50 K and below the initially formed CTCs do not separate over time, but instead recombine slowly after spin thermalization within 100 μ s. In contrast to that, the charges at higher temperatures show a trend to shorter and shorter separation times, perhaps pointing towards a ns time range for the creation of free polarons at room temperature.

6 Summary

In the presented thesis, the various excited states encountered in conjugated organic semiconductors are investigated with respect to their utilization in organic thin-film solar cells. Most of these states are spin-bearing and can therefore be addressed by means of magnetic resonance spectroscopy. The primary singlet excitation (spin 0), as well as positive and negative polaronic charge carriers (spin $1/2$) are discussed. Additionally, triplet excitons (spin 1) and charge transfer complexes are examined, focussing on their differing spin-spin interaction strength. For the investigation of these spin-bearing states especially methods of electron paramagnetic resonance (EPR) are best suited. Therefore according experimental methods were implemented in the course of this work to study conjugated polymers, fullerenes and their blends with continuous wave as well as time-resolved EPR and optically detected magnetic resonance.

The theory Chapters 2 and 3 describe the principles of the observed excited states in organic solar cells and put them in context with the interactions and splittings that can be accessed by EPR methods. Especially the influence of the g -factor anisotropy of polaronic charge carriers on their EPR signatures is explained in detail. Additionally, the exchange and dipolar interaction of strongly to loosely coupled charge carriers are discussed and divided into separate regimes of differing interaction strength.

A first emphasis of the work in Chapter 5.1 lies on spectroscopic signatures of negative polarons, localized on C_{70} fullerene molecules. Therefore blends of several polymer:fullerene-derivative combinations were examined and analyzed with focus on signatures of the fullerenes. As a result, a new NIR absorption band at a wavelength of 1360 nm (0.92 eV) was detected, which is specific for C_{70} fullerene anions and not found for C_{60} . By employing high and low frequency EPR at 130 GHz and 9.4 GHz, it was possible to access the spectrum of the C_{70} anions and derive their g -tensor components with high precision. The resulting values differ strongly from those measured for C_{60} anions. While all g -tensor components of C_{60} anions lie below the free electron g -factor g_e , the g -tensor components of C_{70} anions are equal or larger than g_e . To date, this discrepancy is theoretically not understood and the presented highly precise experimental values can thus serve as a starting point for such a theory, describing both fullerene anions.

6 Summary

These results were the prerequisite for the follow-up study presented in Chapter 5.2. Here, ternary blends of the polymer P3HT together with varying mixing ratios of the two fullerene-derivatives PC₆₀BM and PC₇₀M were investigated for their EPR signatures. By analyzing the relative EPR intensities of both anion signatures, an equal electron distribution among the two fullerene molecules, after the light-induced charge transfer between polymer- and fullerene-phase, could be deduced. Hence, an electron in an organic solar cell experiences no energetic difference between localization on either fullerene. This result is striking, since in literature numerous publications point out the energetic and transport-related differences found in samples of the *pure* fullerenes. These differences are apparently leveled out in mixed samples, enabling the characterization of fullerene-blends as energetically and optically homogeneous materials. This is highly relevant for the industrial-scale production of organic solar cells, because it is vastly more cost efficient to produce a mixture of C₆₀ and C₇₀-fullerenes, instead of their expensive separation and purification.

With respect to the application side, the results described in Chapter 5.3 are also highly topical, as the impact of processing organic semiconductors under the influence of light and air is investigated. Specifically, with the help of spin-sensitive methods, two different reversible and irreversible degradation mechanisms of the polymer P3HT could be identified. The irreversible process is triggered by triplet-activated singlet oxygen and leads to a substantial degradation of the materials' electronic properties. This process can be suppressed completely by processing under the exclusion of light. The second, reversible process consists of a doping of the polymer by adsorption of oxygen molecules to the polymer chains. Thereby a charge transfer complex is formed, that can also serve as a precursor of the irreversible degradation. Because of their small binding energy, these complexes can be dissociated by a vacuum process at elevated temperatures without causing lasting damage to the polymer. On an industrial scale this could be implemented by a dark printing process in air and a subsequent vacuum annealing step before vapor deposition of the metal back electrode. Complicated processing steps in inert atmosphere could therefore be avoided partially.

In Chapter 5.4 the capabilities of time-resolved EPR were employed to study the charge transfer between the polymer P3HT and the fullerene PC₆₀BM. At cryogenic temperatures below 160 K, signatures of charge transfer complexes could be detected. These hybrid states are localized at the polymer:fullerene interface and can be described in the framework of spin-coupled radical pairs as an intermediate en route to charge generation in this class of organic solar cells. The recorded spectrum of this species vanishes within a few microseconds and transforms to the signatures of spatially separated electron and hole, localized on fullerene and polymer, respectively.

From the temperature dependence of the charge separation can be deduced, that this process is thermally activated and occurs accelerated at elevated temperatures. Extrapolating this finding lets us expect that a potential charge transfer complex at room temperature would have a lifetime of merely several nanoseconds. In contrast to that, at temperatures below 50 K these complexes do not separate over time and instead remain strongly bound across the heterointerface before their geminal recombination.

The results presented in this thesis deliver stimulating contributions to the field of organic photovoltaics that are also relevant for their industrial scale production and could help to accelerate establishing this technology in the market. Additionally, interesting aspects for subsequent fundamental research on organic semiconductor materials are given, which are a good basis for follow-up studies dealing with further developed material systems.

Zusammenfassung

Die vorliegende Arbeit beschäftigt sich mit den vielfältigen Anregungszuständen in konjugierten organischen Halbleitern mit Hinblick auf deren Verwendung in organischen Dünnschicht-Solarzellen. Diese verschiedenen Zustände sind zumeist Spin-behaftet und daher mit Methoden der Magnetresonanz adressierbar. Es wird unterschieden zwischen Singulett-Exzitonen (Spin 0) als primärer Photoanregung, sowie positiven und negativen polaronischen Ladungsträgern (Spin $1/2$). Des Weiteren werden Triplet-Exzitonen (Spin 1) und Ladungstransferkomplexe behandelt, die sich durch unterschiedlich starke Spin-Spin Wechselwirkung auszeichnen. Zur Untersuchung dieser Spin-behafteten Zustände bieten sich insbesondere Methoden der Elektron-Paramagnetischen Resonanz-Spektroskopie (EPR) an. Im Zuge dieser Arbeit wurden dafür entsprechende Messmethoden der Dauerstrich (cw) EPR, zeitaufgelösten, transienten EPR und der optisch detektierten Magnetresonanz (ODMR) implementiert und zur Erforschung von konjugierten Polymeren, Fullerenen und deren Mischungen eingesetzt.

Der Theorieteil in den Kapiteln 2 und 3 beschreibt die Grundlagen der beobachteten Anregungszustände in organischen Solarzellen und stellt sie in Zusammenhang mit den Wechselwirkungen und Aufspaltungen, die mit EPR-Methoden nachweisbar sind. Insbesondere wird detailliert auf den Einfluss der g -Faktor-Anisotropie von polaronischen Ladungsträgern auf ihre EPR-Signaturen eingegangen. Außerdem werden die Austausch- und Dipolare Wechselwirkung von stark koppelnden Ladungsträgern behandelt und in Bereiche unterschiedlich starker Interaktion unterteilt.

Ein erster Schwerpunkt der Arbeit in Kapitel 5.1 liegt auf den spektroskopischen Signaturen von negativen Polaronen, die auf C_{70} -Fulleren-Molekülen lokalisiert sind. Dazu wurden Mischungen von mehreren Polymer:Fulleren-Derivat Kombinationen untersucht und mit Hinblick auf die Signaturen der Fullerene hin analysiert. Dabei wurde eine bisher nicht beschriebene Absorptionsbande im Nahinfraroten bei einer Wellenlänge von 1360 nm (0.92 eV) nachgewiesen, die spezifisch für C_{70} -Fulleren-Anionen ist und bei C_{60} nicht vorhanden ist. Unter der Verwendung von Hoch- und Niederfrequenz EPR bei 130 GHz und 9,4 GHz war es möglich den g -Tensor des C_{70} -Fulleren-Anions aufzuklären und hochpräzise zu vermessen. Die gefundenen Werte unterscheiden sich signifikant von denen, die für C_{60} -Anionen nachgewiesen wurden. Während die g -Tensor Komponenten von C_{60} -Anionen allesamt kleiner sind als der g -Faktor des freien Elektrons g_e , sind die g -Tensor Komponenten von C_{70} -Anionen gleich groß und größer als g_e . Dies ist bisher theoretisch nicht erklärt und die vorgestellten präzisen Messungen könnten daher als Ausgangspunkt für eine theoretische Behandlung dieser beiden Fulleren-Anionen dienen.

Diese Ergebnisse waren die Voraussetzung für die Folgestudie in Kapitel 5.2. Es wurden ternäre Mischungen des Polymers P3HT mit den beiden Fulleren-Derivaten PC₆₀BM und PC₇₀BM auf ihre EPR Signaturen hin untersucht. Die relativen EPR-Intensitäten der beiden Fulleren-Anionen wurden in Mischungen mit variierenden Mengenverhältnissen der beiden Fullere analysiert. Als Ergebnis stellte sich heraus, dass nach dem Licht-induzierten Ladungstransfer zwischen Polymer- und Fulleren-Phase, die Elektronen zwischen den zwei verschiedenen Fulleren-Molekülen, gleichverteilt werden. Für ein Elektron in einer organischen Solarzelle besteht demnach kein energetischer Unterschied zwischen diesen Fullerenen. Dieses Ergebnis ist erstaunlich, da in der Literatur diverse Arbeiten Unterschiede der Energie-Zustände und der Transport-Prozesse in Proben der *reinen* Fullere nachgewiesen haben. Diese Unterschiede werden in gemischten Proben offenbar ausgeglichen, so dass sich ein Fulleren-Gemisch als energetisch und optisch homogenes Material beschreiben lässt. Dies ist in Hinblick auf die großindustrielle Herstellung von organischen Solarzellen äußerst relevant, da es deutlich kostengünstiger ist, ein Gemisch aus C₆₀- und C₇₀-Fullerenen herzustellen, anstatt diese aufwendig zu separieren und aufzureinigen.

Mit Hinblick auf die Anwendung sind auch die Ergebnisse aus Kapitel 5.3 hochaktuell, da hier der Einfluss von Licht und Luft während der Prozessierung von organischen Halbleitern untersucht wurde. Im Speziellen wurden mit Spin-sensitiven Methoden zwei verschiedene reversible und irreversible Degradationsprozesse des Polymers P3HT nachgewiesen. Der irreversible Prozess wird durch Triplet-aktivierten Singulett-Sauerstoff ausgelöst und führt zu einer nachhaltigen Degradation der elektronischen Eigenschaften des Materials. Dieser Prozess kann durch Prozessierung unter Licht-Ausschluss vollständig unterbunden werden. Der zweite, reversible Prozess beinhaltet eine Dotierung des Polymers durch die Anlagerung von Sauerstoffmolekülen an die Polymerketten. Dabei wird ein Ladungstransferkomplex ausgebildet, der ebenfalls als Vorstufe der irreversiblen Degradation fungieren kann. Da dieser Komplex jedoch nur schwach gebunden ist, kann er durch einen Vakuum-Prozessschritt bei erhöhter Temperatur dissoziiert werden, ohne dass das Polymer dauerhaft Schaden erleidet. In industriellem Maßstab kann dies z.B. durch einen Druck-Prozess unter Licht-Ausschluss an Luft und ein anschließendes Vakuum-Tempnen vor dem Aufdampfen der Rückelektrode implementiert werden. Aufwendige Prozess-Schritte unter Schutzatmosphäre können demnach teilweise vermieden werden.

In Kapitel 5.4 wurde mit den Möglichkeiten der transienten EPR der Ladungstransfer zwischen dem Polymer P3HT und dem Fulleren PC₆₀BM untersucht. Dabei wurden bei kryogenen Temperaturen von unter 160 K Signale detektiert, die von Ladungstransferkomplexen hervorgerufen werden. Diese Hybridzustände an der Polymer:Fulleren-

6 Summary

Grenzfläche lassen sich als Spin-gekoppelte Radikalpaare beschreiben und stellen eine Zwischenstufe der Ladungsgeneration in dieser Klasse von organischen Solarzellen dar. Das nachgewiesene Spektrum dieser Spezies zerfällt binnen einiger Mikrosekunden und es verbleiben die Signaturen von räumlich getrenntem Elektron und Loch, die nun auf Fulleren und Polymer lokalisiert sind. Aus der Temperaturabhängigkeit dieser Ladungsträgerseparation lässt sich schlussfolgern, dass dieser Prozess thermisch unterstützt wird und dadurch bei erhöhter Temperatur beschleunigt wird. Durch Extrapolation dieser Ergebnisse ist davon auszugehen, dass bei Raumtemperatur ein möglicher Ladungstransferkomplex nur eine maximale Lebensdauer von einigen Nanosekunden aufweist. Im Gegensatz dazu wurde gezeigt, dass bei Temperaturen von weniger als 50 K diese Komplexe nicht mit der Zeit separieren, sondern offenbar über die Grenzfläche hinweg gebunden bleiben, um dann direkt geminal zu rekombinieren.

Die in der vorliegenden Arbeit präsentierten Ergebnisse konnten in mehreren Bereichen, die für die industrielle Fertigung von organischen Solarzellen relevant sind, interessante Beiträge leisten und können damit einen kleinen Teil dazu beitragen diese Technologie schneller am Markt zu etablieren. Ausserdem werden interessante Ansätze für die weitere Grundlagenforschung an organischen Halbleitermaterialien aufgezeigt und stellen einen guten Ausgangspunkt für zukünftige Studien an weiter entwickelten Materialsystemen dar.

Bibliography

- [1] M. A. Green, K. Emery, Y. Hishikawa, W. Warta and E. D. Dunlop. Solar cell efficiency tables (version 41). *Prog. Photovolt: Res. Appl.*, **21**, 1, 1 (2012). doi: [10.1002/pip.2352](https://doi.org/10.1002/pip.2352).
- [2] C. S. Tao, J. Jiang and M. Tao. Natural resource limitations to terawatt-scale solar cells. *Sol. Energy Mater. Sol. Cells*, **95**, 12, 3176 (2011). doi: [10.1016/j.solmat.2011.06.013](https://doi.org/10.1016/j.solmat.2011.06.013).
- [3] C. Deibel and V. Dyakonov. Polymer–fullerene bulk heterojunction solar cells. *Rep. Prog. Phys.*, **73**, 9, 096401 (2010). doi: [10.1088/0034-4885/73/9/096401](https://doi.org/10.1088/0034-4885/73/9/096401).
- [4] M. Rowell, M. Topinka, M. McGehee, H. Prall, G. Dennler, N. Sariciftci, L. Hu and G. Gruner. Organic solar cells with carbon nanotube network electrodes. *Appl. Phys. Lett.*, **88**, 233506 (2006). doi: [10.1063/1.2209887](https://doi.org/10.1063/1.2209887).
- [5] J. van de Lagemaat, T. Barnes, G. Rumbles, S. Shaheen, T. Coutts, C. Weeks, I. Levitsky, J. Peltola and P. Glatkowski. Organic solar cells with carbon nanotubes replacing InO: Sn as the transparent electrode. *Appl. Phys. Lett.*, **88**, 233503 (2006). doi: [10.1063/1.2210081](https://doi.org/10.1063/1.2210081).
- [6] X. Wang, T. Ishwara, W. Gong, M. Campoy-Quiles, J. Nelson and D. D. C. Bradley. High-Performance Metal-Free Solar Cells Using Stamp Transfer Printed Vapor Phase Polymerized Poly(3,4-Ethylenedioxythiophene) Top Anodes. *Adv. Funct. Mater.*, **22**, 7, 1454 (2012). doi: [10.1002/adfm.201101787](https://doi.org/10.1002/adfm.201101787).
- [7] R. F. Service. Outlook Brightens for Plastic Solar Cells. *Science*, **332**, 6027, 293 (2011). doi: [10.1126/science.332.6027.293](https://doi.org/10.1126/science.332.6027.293).
- [8] C. J. Brabec, S. Gowrisanker, J. J. M. Halls, D. Laird, S. Jia and S. P. Williams. Polymer-Fullerene Bulk-Heterojunction Solar Cells. *Adv. Mater.*, **22**, 34, 3839 (2010). doi: [10.1002/adma.200903697](https://doi.org/10.1002/adma.200903697).
- [9] J. H. Burroughes, D. Bradley, A. R. Brown, R. N. Marks, K. Mackay, R. H. Friend, P. L. Burns and A. B. Holmes. Light-emitting diodes based on conjugated polymers. *Nature*, **347**, 6293, 539 (1990). doi: [10.1038/347539a0](https://doi.org/10.1038/347539a0).

Bibliography

- [10] Y. Liang, Z. Xu, J. Xia, S.-T. Tsai, Y. Wu, G. Li, C. Ray and L. Yu. For the Bright Future - Bulk Heterojunction Polymer Solar Cells with Power Conversion Efficiency of 7.4 percent. *Adv. Mater.*, **22**, 20, E135 (2010). doi: [10.1002/adma.200903528](https://doi.org/10.1002/adma.200903528).
- [11] Z. He, C. Zhong, S. Su, M. Xu, H. Wu and Y. Cao. Enhanced power-conversion efficiency in polymer solar cells using an inverted device structure. *Nat. Photonics*, **6**, 9, 591 (2012). doi: [10.1038/nphoton.2012.190](https://doi.org/10.1038/nphoton.2012.190).
- [12] J. Cami, J. Bernard-Salas, E. Peeters and S. E. Malek. Detection of C60 and C70 in a Young Planetary Nebula. *Science*, **329**, 5996, 1180 (2010). doi: [10.1126/science.1192035](https://doi.org/10.1126/science.1192035).
- [13] P. R. Buseck, S. J. Tsipursky and R. Hettich. Fullerenes from the Geological Environment. *Science*, **257**, 5067, 215 (1992). doi: [10.1126/science.257.5067.215](https://doi.org/10.1126/science.257.5067.215).
- [14] I. Riedel, E. von Hauff, J. Parisi, N. Martín, F. Giacalone and V. Dyakonov. Diphenylmethanofullerenes: New and Efficient Acceptors in Bulk-Heterojunction Solar Cells. *Adv. Funct. Mater.*, **15**, 12, 1979 (2005). doi: [10.1002/adfm.200500097](https://doi.org/10.1002/adfm.200500097).
- [15] J. L. Delgado, E. Espíldora, M. Liedtke, A. Sperlich, D. Rauh, A. Baumann, C. Deibel, V. Dyakonov and N. Martin. Fullerene Dimers (C60/C70) for Energy Harvesting. *Chem. Eur. J.*, **15**, 48, 13474 (2009). doi: [10.1002/chem.200902039](https://doi.org/10.1002/chem.200902039).
- [16] J. A. Weil and J. R. Bolton. *Electron Paramagnetic Resonance*. Elementary Theory and Practical Applications. Wiley-Interscience, 2nd edition (2008).
- [17] S. B. Knorr. Elektronenspinresonanz-Untersuchungen zu elektronischen Eigenschaften von Fullerenen und deren Verbindungen. Ph.D. thesis, Universität Stuttgart (2002).
- [18] G. Jeschke. Determination of the nanostructure of polymer materials by electron paramagnetic resonance spectroscopy. *Macromol Rapid Comm*, **23**, 4, 227 (2002). doi: [10.1002/1521-3927\(20020301\)23:4<227::AID-MARC227>3.0.CO;2-D](https://doi.org/10.1002/1521-3927(20020301)23:4<227::AID-MARC227>3.0.CO;2-D).
- [19] K. Marumoto, Y. Muramatsu, S. Ukai, H. Ito and S.-I. Kuroda. Electron Spin Resonance Observations of Field-Induced Polarons in Regioregular Poly(3-octylthiophene) Metal-Insulator-Semiconductor Diode Structures. *J. Phys. Soc. Jpn.*, **73**, 7, 1673 (2004). doi: [10.1143/JPSJ.73.1673](https://doi.org/10.1143/JPSJ.73.1673).

- [20] K. Marumoto, Y. Nagano, T. Sakamoto, S. Ukai, H. Ito and S. Kuroda. ESR studies of field-induced polarons in MIS diode structures with self-organized regioregular poly(3-hexylthiophene). *Colloids and Surfaces A: Physicochem. Eng. Aspects*, **284-285**, 617 (2006). doi: [10.1016/j.colsurfa.2005.09.042](https://doi.org/10.1016/j.colsurfa.2005.09.042).
- [21] K. Marumoto, S.-I. Kuroda, T. Takenobu and Y. Iwasa. Spatial Extent of Wave Functions of Gate-Induced Hole Carriers in Pentacene Field-Effect Devices as Investigated by Electron Spin Resonance. *Phys. Rev. Lett.*, **97**, 25, 256603 (2006). doi: [10.1103/PhysRevLett.97.256603](https://doi.org/10.1103/PhysRevLett.97.256603).
- [22] M. Brustolon and E. Giamello, editors. *Electron Paramagnetic Resonance. A Practitioner's Toolkit*. Wiley & Sons, Inc. (2009).
- [23] M. Oxborrow, J. D. Breeze and N. M. Alford. Room-temperature solid-state maser. *Nature*, **488**, 7411, 353 (2012). doi: [10.1038/nature11339](https://doi.org/10.1038/nature11339).
- [24] O. Efimova and P. J. Hore. Role of exchange and dipolar interactions in the radical pair model of the avian magnetic compass. *Biophys. J.*, **94**, 5, 1565 (2008). doi: [10.1529/biophysj.107.119362](https://doi.org/10.1529/biophysj.107.119362).
- [25] C. C. Moser, J. M. Keske, K. Warncke, R. S. Farid and P. L. Dutton. Nature of biological electron transfer. *Nature*, **355**, 6363, 796 (1992). doi: [10.1038/355796a0](https://doi.org/10.1038/355796a0).
- [26] D. Upper. Unsuccessful Self-Treatment of a Case of Writers Block. *J Appl Behav Anal*, **7**, 3, 497 (1974). doi: [10.1901/jaba.1974.7-497a](https://doi.org/10.1901/jaba.1974.7-497a).
- [27] F. J. Adrian and L. Monchick. Theory of chemically induced magnetic polarization. Effects of S-T±1 mixing in strong magnetic fields. *J. Chem. Phys.*, **71**, 2600 (1979). doi: [10.1063/1.438616](https://doi.org/10.1063/1.438616).
- [28] R. Bittl and S. G. Zech. Pulsed EPR spectroscopy on short-lived intermediates in Photosystem I. *Biochimica et Biophysica Acta*, **1507**, 1-3, 194 (2001). doi: [10.1016/S0005-2728\(01\)00210-9](https://doi.org/10.1016/S0005-2728(01)00210-9).
- [29] J. Behrends, A. Sperlich, A. Schnegg, T. Biskup, C. Teutloff, K. Lips, V. Dyakonov and R. Bittl. Direct detection of photoinduced charge transfer complexes in polymer fullerene blends. *Phys. Rev. B*, **85**, 12 (2012). doi: [10.1103/PhysRevB.85.125206](https://doi.org/10.1103/PhysRevB.85.125206).
- [30] C. D. Buckley, D. A. Hunter, P. J. Hore and K. A. McLauchlan. Electron spin resonance of spin-correlated radical pairs. *Chem. Phys. Lett.*, **135**, 3, 307 (1987). doi: [10.1016/0009-2614\(87\)85162-X](https://doi.org/10.1016/0009-2614(87)85162-X).

Bibliography

- [31] G. L. Closs, M. D. E. Forbes and J. R. Norris. Spin-polarized electron paramagnetic resonance spectra of radical pairs in micelles: observation of electron spin-spin interactions. *J. Phys. Chem.*, **91**, 13, 3592 (1987). doi: [10.1021/j100297a026](https://doi.org/10.1021/j100297a026).
- [32] V. Dyakonov, G. Rösler, M. Schwoerer and E. Frankevich. Evidence for triplet interchain polaron pairs and their transformations in polyphenylenevinylene. *Phys. Rev. B*, **56**, 7, 3852 (1997). doi: [10.1103/PhysRevB.56.3852](https://doi.org/10.1103/PhysRevB.56.3852).
- [33] A. Suna. Kinematics of Exciton-Exciton Annihilation in Molecular Crystals. *Phys. Rev. B*, **1**, 4, 1716 (1970). doi: [10.1103/PhysRevB.1.1716](https://doi.org/10.1103/PhysRevB.1.1716).
- [34] R. E. Merrifield. Magnetic effects on triplet exciton interactions. *Pure Appl. Chem.*, **27**, 3, 481 (1971). doi: [10.1351/pac197127030481](https://doi.org/10.1351/pac197127030481).
- [35] J. Partee, E. Frankevich, B. Uhlhorn, J. Shinar, Y. Ding and T. Barton. Delayed fluorescence and triplet-triplet annihilation in Pi-conjugated polymers. *Phys. Rev. Lett.*, **82**, 18, 3673 (1999). doi: [10.1103/PhysRevLett.82.3673](https://doi.org/10.1103/PhysRevLett.82.3673).
- [36] V. Dyakonov and E. Frankevich. On the role played by polaron pairs in photophysical processes in semiconducting polymers. *Chem. Phys.*, **227**, 1-2, 203 (1998). doi: [10.1016/S0301-0104\(97\)00305-4](https://doi.org/10.1016/S0301-0104(97)00305-4).
- [37] A. Gruber. Scanning Confocal Optical Microscopy and Magnetic Resonance on Single Defect Centers. *Science*, **276**, 5321, 2012 (1997). doi: [10.1126/science.276.5321.2012](https://doi.org/10.1126/science.276.5321.2012).
- [38] N. Manson, J. Harrison and M. Sellars. Nitrogen-vacancy center in diamond: Model of the electronic structure and associated dynamics. *Phys. Rev. B*, **74**, 10, 104303 (2006). doi: [10.1103/PhysRevB.74.104303](https://doi.org/10.1103/PhysRevB.74.104303).
- [39] D. Riedel, F. Fuchs, H. Kraus, S. Vāth, A. Sperlich, V. Dyakonov, A. Soltamova, P. Baranov, V. Ilyin and G. Astakhov. Resonant Addressing and Manipulation of Silicon Vacancy Qubits in Silicon Carbide. *Phys. Rev. Lett.*, **109**, 22, 226402 (2012). doi: [10.1103/PhysRevLett.109.226402](https://doi.org/10.1103/PhysRevLett.109.226402).
- [40] M. M. Wienk, J. M. Kroon, W. J. H. Verhees, J. Knol, J. C. Hummelen, P. A. van Hal and R. A. J. Janssen. Efficient Methano[70]fullerene/MDMO-PPV Bulk Heterojunction Photovoltaic Cells. *Angew. Chem. Int. Ed.*, **42**, 29, 3371 (2003). doi: [10.1002/anie.200351647](https://doi.org/10.1002/anie.200351647).

- [41] F. Zhang, Z. Zhuo, J. Zhang, X. Wang, X. Xu, Z. Wang, Y. Xin, J. Wang, J. Wang, W. Tang, Z. Xu and Y. Wang. Influence of PC60BM or PC70BM as electron acceptor on the performance of polymer solar cells. *Sol. Energy Mater. Sol. Cells*, **97**, C, 71 (2012). doi: [10.1016/j.solmat.2011.09.006](https://doi.org/10.1016/j.solmat.2011.09.006).
- [42] M. Baumgarten and L. Gherghel. Electronic properties of charged fullerenes characterized by EPR and Vis-NIR spectroscopy. *Appl. Magn. Reson.*, **11**, 2, 171 (1996). doi: [10.1007/BF03162052](https://doi.org/10.1007/BF03162052).
- [43] H. Hase and Y. Miyatake. Comparative ESR study of C60 and C70 radical anions produced in [gamma]-irradiated organic solid solutions at 77 K. *Chem. Phys. Lett.*, **245**, 1, 95 (1995). doi: [10.1016/0009-2614\(95\)00974-9](https://doi.org/10.1016/0009-2614(95)00974-9).
- [44] M. Fujitsuka, A. Watanabe, O. Ito, K. Yamamoto and H. Funasaka. Laser Flash Photolysis Study on Photochemical Generation of Radical Cations of Fullerenes C60, C70, and C76. *J. Phys. Chem. A*, **101**, 43, 7960 (1997). doi: [10.1021/jp971850c](https://doi.org/10.1021/jp971850c).
- [45] D. Konarev, S. Khasanov, G. Saito, A. Otsuka, Y. Yoshida and R. Lyubovskaya. Formation of single-bonded (C60-)2 and (C70-)2 dimers in crystalline ionic complexes of fullerenes. *J. Am. Chem. Soc.*, **125**, 33, 10074 (2003). doi: [10.1021/ja035546a](https://doi.org/10.1021/ja035546a).
- [46] L. Gherghel and M. Baumgarten. Redox states of C60 and C70 measured by EPR and optical absorption spectroscopy, Part II. *Synth. Met.*, **70**, 1-3, 1389 (1995). doi: [10.1016/0379-6779\(94\)02891-2](https://doi.org/10.1016/0379-6779(94)02891-2).
- [47] O. Poluektov, L. Utschig, S. Schlesselman, K. Lakshmi, G. Brudvig, G. Kothe and M. Thurnauer. Electronic structure of the P-700 special pair from high-frequency electron paramagnetic resonance spectroscopy. *J. Phys. Chem. B*, **106**, 35, 8911 (2002). doi: [10.1021/jp021465+](https://doi.org/10.1021/jp021465+).
- [48] S. Stoll and A. Schweiger. EasySpin, a comprehensive software package for spectral simulation and analysis in EPR. *J. Magn. Reson.*, **178**, 1, 42 (2006). doi: [10.1016/j.jmr.2005.08.013](https://doi.org/10.1016/j.jmr.2005.08.013).
- [49] S. Sibley, S. Argentine and A. Francis. A photoluminescence study of C60 and C70. *Chem. Phys. Lett.*, **188**, 3-4, 187 (1992). doi: [10.1016/0009-2614\(92\)90007-A](https://doi.org/10.1016/0009-2614(92)90007-A).
- [50] R. Österbacka, C. P. An, X. Jiang and Z. V. Vardeny. Two-dimensional electronic excitations in self-assembled conjugated polymer nanocrystals. *Science*, **287**, 5454, 839 (2000). doi: [10.1126/science.287.5454.839](https://doi.org/10.1126/science.287.5454.839).

Bibliography

- [51] I. Montanari, A. F. Nogueira, J. Nelson, J. R. Durrant, C. Winder, M. A. Loi, N. S. Sariciftci and C. Brabec. Transient optical studies of charge recombination dynamics in a polymer/fullerene composite at room temperature. *Appl. Phys. Lett.*, **81**, 16, 3001 (2002). doi: [10.1063/1.1512943](https://doi.org/10.1063/1.1512943).
- [52] A. L. Holt, J. M. Leger and S. A. Carter. Electrochemical and optical characterization of p- and n-doped poly[2-methoxy-5-(2-ethylhexyloxy)-1,4-phenylenevinylene]. *J. Chem. Phys.*, **123**, 4, 044704 (2005). doi: [10.1063/1.1949188](https://doi.org/10.1063/1.1949188).
- [53] T. Oku, S. Nagaoka, A. Suzuki, K. Kikuchi, Y. Hayashi, H. Inukai, H. Sakuragi and T. Soga. Formation and characterization of polymer/fullerene bulk heterojunction solar cells. *J. Phys. Chem. Sol.*, **69**, 5-6, 1276 (2008). doi: [10.1016/j.jpcs.2007.10.117](https://doi.org/10.1016/j.jpcs.2007.10.117).
- [54] A. M. Ramos, M. T. Rispens, J. C. Hummelen and R. A. J. Janssen. A poly (p-phenylene ethynylene vinylene) with pendant fullerenes. *Synth. Met.*, **119**, 1-3, 171 (2001). doi: [10.1016/S0379-6779\(00\)00600-7](https://doi.org/10.1016/S0379-6779(00)00600-7).
- [55] N. Sariciftci, L. Smilowitz, A. Heeger and F. Wudl. Photoinduced electron transfer from a conducting polymer to buckminsterfullerene. *Science*, **258**, 5087, 1474 (1992). doi: [10.1126/science.258.5087.1474](https://doi.org/10.1126/science.258.5087.1474).
- [56] S. Morita, A. A. Zakhidov and K. Yoshino. Doping effect of buckminsterfullerene in conducting polymer: Change of absorption spectrum and quenching of luminescence. *Sol. State Comm.*, **82**, 4, 249 (1992). doi: [10.1016/0038-1098\(92\)90636-N](https://doi.org/10.1016/0038-1098(92)90636-N).
- [57] V. Dyakonov, G. Zorinants, M. Scharber, C. Brabec, R. Janssen, J. Hummelen and N. Sariciftci. Photoinduced charge carriers in conjugated polymer–fullerene composites studied with light-induced electron-spin resonance. *Phys. Rev. B*, **59**, 12, 8019 (1999). doi: [10.1103/PhysRevB.59.8019](https://doi.org/10.1103/PhysRevB.59.8019).
- [58] J. De Ceuster, E. Goovaerts, A. Bouwen, J. C. Hummelen and V. Dyakonov. High-frequency (95 GHz) electron paramagnetic resonance study of the photoinduced charge transfer in conjugated polymer–fullerene composites. *Phys. Rev. B*, **64**, 19, 1 (2001). doi: [10.1103/PhysRevB.64.195206](https://doi.org/10.1103/PhysRevB.64.195206).
- [59] K. Marumoto, Y. Muramatsu, N. Takeuchi and S. Kuroda. Light-induced ESR studies of polarons in regioregular poly (3-alkylthiophene)-fullerene composites. *Synth. Met.*, **135**, 1, 433 (2003). doi: [10.1016/S0379-6779\(02\)00557-X](https://doi.org/10.1016/S0379-6779(02)00557-X).

- [60] J. Schafferhans, A. Baumann, C. Deibel and V. Dyakonov. Trap distribution and the impact of oxygen-induced traps on the charge transport in poly(3-hexylthiophene). *Appl. Phys. Lett.*, **93**, 9, 093303 (2008). doi: [10.1063/1.2978237](https://doi.org/10.1063/1.2978237).
- [61] J. Schafferhans, A. Baumann, A. Wagenpfahl, C. Deibel and V. Dyakonov. Oxygen doping of P3HT:PCBM blends: Influence on trap states, charge carrier mobility and solar cell performance. *Org. Electron.*, **11**, 10, 1693 (2010). doi: [10.1016/j.orgel.2010.07.016](https://doi.org/10.1016/j.orgel.2010.07.016).
- [62] K. Marumoto, N. Takeuchi, T. Ozaki and S. Kuroda. ESR studies of photo-generated polarons in regioregular poly(3-alkylthiophene)–fullerene composite. *Synth. Met.*, **129**, 3, 239 (2002). doi: [10.1016/S0379-6779\(02\)00080-2](https://doi.org/10.1016/S0379-6779(02)00080-2).
- [63] T. J. Savenije, A. Sperlich, H. Kraus, O. Poluektov, M. Heeney and V. Dyakonov. Observation of bi-polarons in blends of conjugated copolymers and fullerene derivatives. *Phys. Chem. Chem. Phys.*, **13**, 37, 16579 (2011). doi: [10.1039/c1cp21607d](https://doi.org/10.1039/c1cp21607d).
- [64] A. J. Stone. Gauge Invariance of the g Tensor. *Proc. R. Soc. Lond. A*, **271**, 1346, 424 (1963). doi: [10.1098/rspa.1963.0027](https://doi.org/10.1098/rspa.1963.0027).
- [65] J. Friedrich, P. Schweitzer, K.-P. Dinse, P. Rapta and A. Stasko. EPR Study of Radical Anions of C₆₀ and C₇₀. *Appl. Magn. Reson.*, **7**, 415 (1994). doi: [10.1007/BF03162622](https://doi.org/10.1007/BF03162622).
- [66] D. Dubois, K. M. Kadish, S. Flanagan, R. E. Haufler, L. P. F. Chibante and L. J. Wilson. Spectroelectrochemical study of the C₆₀ and C₇₀ fullerenes and their mono-, di-, tri- and tetraanions. *J. Am. Chem. Soc.*, **113**, 11, 4364 (1991). doi: [10.1021/ja00011a069](https://doi.org/10.1021/ja00011a069).
- [67] F. J. Adrian. Spin-orbit effects in fullerenes. *Chem. Phys.*, **211**, 1-3, 73 (1996). doi: [10.1016/0301-0104\(96\)00243-1](https://doi.org/10.1016/0301-0104(96)00243-1).
- [68] A. Anctil, C. W. Babbitt, R. P. Raffaele and B. J. Landi. Material and Energy Intensity of Fullerene Production. *Environ. Sci. Technol.*, **45**, 6, 2353 (2011). doi: [10.1021/es103860a](https://doi.org/10.1021/es103860a).
- [69] L. M. Popescu. Fullerene based organic solar cells. Ph.D. thesis, University of Groningen (2008).
- [70] D. Kronholm, J. C. Hummelen, A. B. Sieval and P. Van't Hof. Blends of fullerene derivatives, and uses thereof in electronic devices. US patent 8076050 (2011).

Bibliography

- [71] P. H. Wöbkenberg, D. D. C. Bradley, D. Kronholm, J. C. Hummelen, D. M. de Leeuw, M. Cölle and T. D. Anthopoulos. High mobility n-channel organic field-effect transistors based on soluble C60 and C70 fullerene derivatives. *Synth. Met.*, **158**, 11, 468 (2008). doi: [10.1016/j.synthmet.2008.03.016](https://doi.org/10.1016/j.synthmet.2008.03.016).
- [72] J. Schafferhans, C. Deibel and V. Dyakonov. Electronic Trap States in Methanofullerenes. *Adv. Energy Mater.*, **1**, 4, 655 (2011). doi: [10.1002/aenm.201100175](https://doi.org/10.1002/aenm.201100175).
- [73] S. R. Cowan, W. L. Leong, N. Banerji, G. Dennler and A. J. Heeger. Identifying a Threshold Impurity Level for Organic Solar Cells: Enhanced First-Order Recombination Via Well-Defined PC84BM Traps in Organic Bulk Heterojunction Solar Cells. *Adv. Funct. Mater.*, **21**, 16, 3083 (2011). doi: [10.1002/adfm.201100514](https://doi.org/10.1002/adfm.201100514).
- [74] E. Busby, C. W. Rochester, A. J. Moulé and D. S. Larsen. Acceptor dependent polaron recombination dynamics in poly 3-hexyl thiophene: Fullerene composite films. *Chem. Phys. Lett.*, **513**, 1-3, 77 (2011). doi: [10.1016/j.cplett.2011.07.066](https://doi.org/10.1016/j.cplett.2011.07.066).
- [75] F. B. Kooistra, V. D. Mihailetschi, L. M. Popescu, D. Kronholm, P. W. M. Blom and J. C. Hummelen. New C₈₄ Derivative and Its Application in a Bulk Heterojunction Solar Cell. *Chem. Mater.*, **18**, 13, 3068 (2006). doi: [10.1021/cm052783z](https://doi.org/10.1021/cm052783z).
- [76] A. Sperlich, M. Liedtke, J. Kern, H. Kraus, C. Deibel, S. Filippone, J. L. Delgado and V. Dyakonov. Photoinduced C70 radical anions in polymer:fullerene blends. *Phys. Stat. Sol. RRL*, **5**, 3, 128 (2011). doi: [10.1002/pssr.201105030](https://doi.org/10.1002/pssr.201105030).
- [77] O. Poluektov, S. Filippone, N. Martín, A. Sperlich, C. Deibel and V. Dyakonov. Spin Signatures of Photogenerated Radical Anions in Polymer-[70]Fullerene Bulk Heterojunctions: High Frequency Pulsed EPR Spectroscopy. *J. Phys. Chem. B*, **114**, 45, 14426 (2010). doi: [10.1021/jp1012347](https://doi.org/10.1021/jp1012347).
- [78] C. Brabec and J. Durrant. Solution-processed organic solar cells. *MRS Bull.*, **33**, 07, 670 (2008). doi: [10.1557/mrs2008.138](https://doi.org/10.1557/mrs2008.138).
- [79] M. Jørgensen, K. Norrman and F. Krebs. Stability/degradation of polymer solar cells. *Sol. Energy Mater. Sol. Cells*, **92**, 7, 686 (2008). doi: [10.1016/j.solmat.2008.01.005](https://doi.org/10.1016/j.solmat.2008.01.005).
- [80] M. S. A. Abdou, F. P. Orfino, Y. Son and S. Holdcroft. Interaction of oxygen with conjugated polymers: Charge transfer complex formation with poly (3-alkylthiophenes). *J. Am. Chem. Soc.*, **119**, 19, 4518 (1997). doi: [10.1021/ja964229j](https://doi.org/10.1021/ja964229j).

- [81] L. Lüer, H. Egelhaaf, D. Oelkrug, G. Cerullo, G. Lanzani, B. Huisman and D. de Leeuw. Oxygen-induced quenching of photoexcited states in polythiophene films. *Org. Electron.*, **5**, 1-3, 83 (2004). doi: [10.1016/j.orgel.2003.12.005](https://doi.org/10.1016/j.orgel.2003.12.005).
- [82] H. Hintz, H. Egelhaaf, H. Peisert and T. Chassé. Photo-oxidation and ozonization of poly (3-hexylthiophene) thin films as studied by UV/VIS and photoelectron spectroscopy. *Polym. Degrad. Stab.*, **95**, 5, 818 (2010). doi: [10.1016/j.polymdegradstab.2010.02.004](https://doi.org/10.1016/j.polymdegradstab.2010.02.004).
- [83] C. Evans and J. Scaiano. Photochemical generation of radical cations from alpha.-terthienyl and related thiophenes: kinetic behavior and magnetic field effects on radical-ion pairs in micellar solution. *J. Am. Chem. Soc.*, **112**, 7, 2694 (1990). doi: [10.1021/ja00163a034](https://doi.org/10.1021/ja00163a034).
- [84] H. Blok, J. Disselhorst, S. Orlinskii and J. Schmidt. A continuous-wave and pulsed electron spin resonance spectrometer operating at 275 GHz. *J. Magn. Reson.*, **166**, 1, 92 (2004). doi: [10.1016/j.jmr.2003.10.011](https://doi.org/10.1016/j.jmr.2003.10.011).
- [85] H. Blok. Electron paramagnetic resonance and electron nuclear double resonance spectroscopy at 275 GHz. Ph.D. thesis, University of Leiden, The Netherlands (2006).
- [86] A. Förtig, A. Baumann, D. Rauh, V. Dyakonov and C. Deibel. Charge carrier concentration and temperature dependent recombination in polymer-fullerene solar cells. *Appl. Phys. Lett.*, **95**, 5, 052104 (2009). doi: [10.1063/1.3202389](https://doi.org/10.1063/1.3202389).
- [87] C.-K. Lu and H.-F. Meng. Hole doping by molecular oxygen in organic semiconductors: Band-structure calculations. *Phys. Rev. B*, **75**, 23, 235206 (2007). doi: [10.1103/PhysRevB.75.235206](https://doi.org/10.1103/PhysRevB.75.235206).
- [88] M. Jonas. Concepts and methods of ESR dating. *Radiat. Meas.*, **27**, 5-6, 943 (1997). doi: [10.1016/S1350-4487\(97\)00202-3](https://doi.org/10.1016/S1350-4487(97)00202-3).
- [89] A. Hill. The combinations of haemoglobin with oxygen and with carbon monoxide. I. *Biochem. J.*, **7**, 5, 471 (1913).
- [90] J. Weiss. The Hill equation revisited: uses and misuses. *FASEB J.*, **11**, 11, 835 (1997).
- [91] H. Liao, C. Yang, C. Liu, S. Horng and H. Meng. Dynamics and reversibility of oxygen doping and de-doping for conjugated polymer. *J. Appl. Phys.*, **103**, 10, 104506 (2008). doi: [10.1063/1.2917419](https://doi.org/10.1063/1.2917419).

Bibliography

- [92] A. Dhoot, D. Ginger, D. Beljonne, Z. Shuai and N. Greenham. Triplet formation and decay in conjugated polymer devices. *Chem. Phys. Lett.*, **360**, 3-4, 195 (2002). doi: [10.1016/S0009-2614\(02\)00840-0](https://doi.org/10.1016/S0009-2614(02)00840-0).
- [93] L. Hachani, A. Benfredj, S. Romdhane, M. Mejatty, J. Monge and H. Bouchriha. Fluorescence-detected magnetic resonance in organic systems: A pair-density matrix formalism approach. *Phys. Rev. B*, **77**, 3, 035212 (2008). doi: [10.1103/PhysRevB.77.035212](https://doi.org/10.1103/PhysRevB.77.035212).
- [94] M. Liedtke, A. Sperlich, H. Kraus, A. Baumann, C. Deibel, M. J. M. Wirix, J. Loos, C. M. Cardona and V. Dyakonov. Triplet Exciton Generation in Bulk-Heterojunction Solar Cells Based on Endohedral Fullerenes. *J. Am. Chem. Soc.*, **133**, 23, 9088 (2011). doi: [doi: 10.1021/ja2025432](https://doi.org/10.1021/ja2025432).
- [95] K. Kawaoka, A. Khan and D. Kearns. Role of singlet excited states of molecular oxygen in the quenching of organic triplet states. *J. Chem. Phys.*, **46**, 5, 1842 (1967). doi: [10.1063/1.1840943](https://doi.org/10.1063/1.1840943).
- [96] R. Scurlock and P. Ogilby. Singlet molecular oxygen (1. DELTA. gO₂) formation upon irradiation of an oxygen (3. SIGMA. g-O₂)-organic molecule charge-transfer absorption band. *J. Phys. Chem.*, **93**, 14, 5493 (1989). doi: [10.1021/j100351a035](https://doi.org/10.1021/j100351a035).
- [97] A. Guerrero, P. P. Boix, L. F. Marchesi, T. Ripolles-Sanchis, E. C. Pereira and G. Garcia-Belmonte. Oxygen doping-induced photogeneration loss in P3HT:PCBM solar cells. *Sol. Energy Mater. Sol. Cells* (2012). doi: [10.1016/j.solmat.2012.01.012](https://doi.org/10.1016/j.solmat.2012.01.012).
- [98] C. Deibel, D. Mack, J. Gorenflot, A. Schöll, S. Krause, F. Reinert, D. Rauh and V. Dyakonov. Energetics of excited states in the conjugated polymer poly(3-hexylthiophene). *Phys. Rev. B*, **81**, 8, 085202 (2010). doi: [10.1103/PhysRevB.81.085202](https://doi.org/10.1103/PhysRevB.81.085202).
- [99] H. Neugebauer, C. Brabec, J. Hummelen and N. Sariciftci. Stability and photodegradation mechanisms of conjugated polymer/fullerene plastic solar cells. *Sol. Ener. Mat. Sol. Cells*, **61**, 1, 35 (2000). doi: [10.1016/S0927-0248\(99\)00094-X](https://doi.org/10.1016/S0927-0248(99)00094-X).
- [100] I. V. Golovnin, A. A. Bakulin, S. A. Zapunidy, E. M. Nechvolodova and D. Y. Paraschuk. Dramatic enhancement of photo-oxidation stability of a conjugated polymer in blends with organic acceptor. *Appl. Phys. Lett.*, **92**, 24, 243311 (2008). doi: [10.1063/1.2945801](https://doi.org/10.1063/1.2945801).

- [101] I.-W. Hwang, D. Moses and A. J. Heeger. Photoinduced Carrier Generation in P3HT/PCBM Bulk Heterojunction Materials. *J. Phys. Chem. C*, **112**, 11, 4350 (2008). doi: [10.1021/jp075565x](https://doi.org/10.1021/jp075565x).
- [102] H. Ohkita, S. Cook, Y. Astuti, W. Duffy, S. Tierney, W. Zhang, M. Heeney, I. McCulloch, J. Nelson, D. D. C. Bradley and J. R. Durrant. Charge Carrier Formation in Polythiophene/Fullerene Blend Films Studied by Transient Absorption Spectroscopy. *J. Am. Chem. Soc.*, **130**, 10, 3030 (2008). doi: [10.1021/ja076568q](https://doi.org/10.1021/ja076568q).
- [103] J. Kniepert, M. Schubert, J. Blakesley and D. Neher. Photogeneration and Recombination in P3HT/PCBM Solar Cells Probed by Time-Delayed Collection Field Experiments. *J. Phys. Chem. Lett.*, **2**, 700 (2011). doi: [10.1021/jz200155b](https://doi.org/10.1021/jz200155b).
- [104] S. Singh and Z. V. Vardeny. Ultrafast Transient Spectroscopy of Polymer/Fullerene Blends for Organic Photovoltaic Applications. *Materials*, **6**, 3, 897 (2013). doi: [10.3390/ma6030897](https://doi.org/10.3390/ma6030897).
- [105] L. Franco, A. Toffoletti, M. Ruzzi, L. Montanari, C. Carati, L. Bonoldi and R. Po. Time-Resolved EPR of Photoinduced Excited States in a Semiconducting Polymer/PCBM Blend. *J. Phys. Chem. C*, **117**, 4, 1554 (2013). doi: [10.1021/jp306278v](https://doi.org/10.1021/jp306278v).
- [106] Y. Zhang, T. P. Basel, B. R. Gautam, X. Yang, D. J. Mascaro, F. Liu and Z. V. Vardeny. Spin-enhanced organic bulk heterojunction photovoltaic solar cells. *Nature Communications*, **3**, 1043 (2012). doi: [10.1038/ncomms2057](https://doi.org/10.1038/ncomms2057).
- [107] A. Rao, P. C. Y. Chow, S. Gélinas, C. W. Schlenker, C.-Z. Li, H.-L. Yip, A. K. Y. Jen, D. S. Ginger and R. H. Friend. The role of spin in the kinetic control of recombination in organic photovoltaics. *Nature*, **500**, 7463, 435 (2013). doi: [10.1038/nature12339](https://doi.org/10.1038/nature12339).
- [108] Y. Kobori, S. Sekiguchi, K. Akiyama and S. Tero-Kubota. Chemically Induced Dynamic Electron Polarization Study on the Mechanism of Exchange Interaction in Radical Ion Pairs Generated by Photoinduced Electron Transfer Reactions. *J. Phys. Chem. A*, **103**, 28, 5416 (1999). doi: [10.1021/jp990359d](https://doi.org/10.1021/jp990359d).
- [109] T. Miura, R. Carmieli and M. R. Wasielewski. Time-Resolved EPR Studies of Charge Recombination and Triplet-State Formation within Donor-Bridge-Acceptor Molecules Having Wire-Like Oligofluorene Bridges. *J. Phys. Chem. A*, **114**, 18, 5769 (2010). doi: [10.1021/jp101523n](https://doi.org/10.1021/jp101523n).
- [110] M. T. Colvin, A. B. Ricks, A. M. Scott, D. T. Co and M. R. Wasielewski. Intersystem Crossing Involving Strongly Spin Exchange-Coupled Radical Ion Pairs in

Bibliography

- Donor–bridge–Acceptor Molecules. *J. Phys. Chem. A*, **116**, 8, 1923 (2012). doi: [10.1021/jp212546w](https://doi.org/10.1021/jp212546w).
- [111] L. Pasimeni, A. Maniero, M. Ruzzi, M. Prato, T. Da Ros, G. Barbarella and M. Zambianchi. Photoinduced electron transfer in sexithiophene/fullerene derivative blends: evidence of long-lived spin correlated radical pairs. *Chem. Comm.*, **8**, 5, 429 (1999). doi: [10.1039/A809036J](https://doi.org/10.1039/A809036J).
- [112] L. Pasimeni, M. Ruzzi, M. Prato, T. Da Ros, G. Barbarella and M. Zambianchi. Spin correlated radical ion pairs generated by photoinduced electron transfer in composites of sexithiophene/fullerene derivatives: a transient EPR study. *Chem. Phys.*, **263**, 1, 83 (2001). doi: [10.1016/S0301-0104\(00\)00339-6](https://doi.org/10.1016/S0301-0104(00)00339-6).
- [113] N. Schultz, M. Scharber, C. Brabec and N. Sariciftci. Low-temperature recombination kinetics of photoexcited persistent charge carriers in conjugated polymer/fullerene composite films. *Phys. Rev. B*, **64**, 24, 245210 (2001). doi: [10.1103/PhysRevB.64.245210](https://doi.org/10.1103/PhysRevB.64.245210).
- [114] S. Weber, T. Biskup, A. Okafuji, A. R. Marino, T. Berthold, G. Link, K. Hitomi, E. D. Getzoff, E. Schleicher and J. R. Norris, Jr. Origin of Light-Induced Spin-Correlated Radical Pairs in Cryptochrome. *J. Phys. Chem. B*, **114**, 45, 14745 (2010). doi: [10.1021/jp103401u](https://doi.org/10.1021/jp103401u).

7 Appendix

7.1 List of Useful Constants

These constants are adapted from the official CODATA set of internationally recommended values of fundamental physics constants maintained by NIST.¹

Constant	Value	Unit	Description
c	299 792 458(00)	m s^{-1}	speed of light in vacuum
h	$6.626\,069\,57(29) \cdot 10^{-34}$	J s	Planck constant
$\hbar = \frac{h}{2\pi}$	$1.054\,571\,726(47) \cdot 10^{-34}$	J s	Planck constant over 2π
k_B	$1.380\,648\,8(13) \cdot 10^{-23}$	J K^{-1}	Boltzmann constant
ϵ_0	$8.854\,187\,817(00) \cdot 10^{-12}$	$\text{F m}^{-1} = \text{A s (V m)}^{-1}$	electric constant
μ_0	$4\pi \cdot 10^{-7}$	$\text{N A}^{-2} = \text{T}^2 \text{m}^3 \text{J}^{-1}$	magnetic constant
$\mu_B = \frac{e\hbar}{2m_e}$	$9.274\,009\,68(20) \cdot 10^{-24}$	J T^{-1}	Bohr magneton
$g_e = \frac{\gamma_e \hbar}{\mu_B}$	2.002 319 304 361 53(53)		free electron g-factor
γ_e	$1.760\,859\,708(39) \cdot 10^{11}$	$\text{s}^{-1} \text{T}^{-1}$	electron gyromagnetic ratio
γ'_p	$2.675\,153\,268(66) \cdot 10^8$	$\text{s}^{-1} \text{T}^{-1}$	shielded proton gyrom. ratio
e	$1.602\,176\,565(35) \cdot 10^{-19}$	A s	elementary charge
eV	$1.602\,176\,565(35) \cdot 10^{-19}$	$\text{V A s} = \text{J}$	electron volt
$\frac{hc}{eV}$	1 239.841 929	eV nm	nm \leftrightarrow eV conversion

¹Jan. 2013: <http://physics.nist.gov/cuu/Constants/index.html>

7.2 Publications and Conference Contributions

Awards

- Energy & Environmental Science Poster Prize at the SPP 1355 Summer School together with Hannes Kraus. Veitshöchheim 2011
- EUROMAR student grant for the visit of the EUROMAR 2012 conference in Dublin.

Full Paper in Review Journals

1. J. Delgado, E. Espíldora, M. Liedtke, A. Sperlich, D. Rauh, A. Baumann, C. Deibel, V. Dyakonov and N. Martín. Fullerene Dimers (C60/C70) for Energy Harvesting. *Chem. Eur. J.*, **15**, 48, 13474 (2009). doi: [10.1002/chem.200902039](https://doi.org/10.1002/chem.200902039).
2. O. Poluektov, S. Filippone, N. Martín, A. Sperlich, C. Deibel and V. Dyakonov. Spin Signatures of Photogenerated Radical Anions in Polymer-[70]Fullerene Bulk Heterojunctions: High Frequency Pulsed EPR Spectroscopy. *J. Phys. Chem. B*, **114**, 45, 14426 (2010). doi: [10.1021/jp1012347](https://doi.org/10.1021/jp1012347). arXiv: [1110.1577](https://arxiv.org/abs/1110.1577).
3. M. Liedtke, A. Sperlich, H. Kraus, C. Deibel, V. Dyakonov, S. Filippone, J. L. Delgado, N. Martín and O. G. Poluektov. Spectroscopic Signatures of Photogenerated Radical Anions in Polymer-[C70]Fullerene Bulk Heterojunctions. *ECS Trans.*, **28**, 17, 3 (2010). doi: [10.1149/1.3503347](https://doi.org/10.1149/1.3503347). arXiv: [1007.1653](https://arxiv.org/abs/1007.1653).
4. A. Sperlich, M. Liedtke, J. Kern, H. Kraus, C. Deibel, S. Filippone, J. L. Delgado and V. Dyakonov. Photoinduced C70 radical anions in polymer:fullerene blends. *Phys. Stat. Sol. RRL*, **5**, 3, 128 (2011). doi: [10.1002/pssr.201105030](https://doi.org/10.1002/pssr.201105030). arXiv: [1102.1899](https://arxiv.org/abs/1102.1899).
5. M. Liedtke, A. Sperlich, H. Kraus, A. Baumann, C. Deibel, M. J. M. Wirix, J. Loos, C. M. Cardona and V. Dyakonov. Triplet Exciton Generation in Bulk-Heterojunction Solar Cells Based on Endohedral Fullerenes. *J. Am. Chem. Soc.*, **133**, 23, 9088 (2011). doi: [10.1021/ja2025432](https://doi.org/10.1021/ja2025432). arXiv: [1107.3525](https://arxiv.org/abs/1107.3525).
6. A. Sperlich, H. Kraus, C. Deibel, H. Blok, J. Schmidt and V. Dyakonov. Reversible and Irreversible Interactions of Poly(3-hexylthiophene) with Oxygen Studied by Spin-Sensitive Methods. *J. Phys. Chem. B*, **115**, 46, 13513 (2011). doi: [10.1021/jp2077215](https://doi.org/10.1021/jp2077215). arXiv: [1110.1316](https://arxiv.org/abs/1110.1316).
7. T. Savenije, A. Sperlich, H. Kraus, O. Poluektov, M. Heeney and V. Dyakonov. Observation of bi-polarons in blends of conjugated copolymers and fullerene derivatives. *Phys. Chem. Chem. Phys.*, **13**, 37, 16579 (2011). doi: [10.1039/c1cp21607d](https://doi.org/10.1039/c1cp21607d). arXiv: [1110.1881](https://arxiv.org/abs/1110.1881).
8. J. Gorenflot, A. Sperlich, A. Baumann, D. Rauh, A. Vasilev, C. Li, M. Baumgarten, C. Deibel and V. Dyakonov. Detailed study of N,N'-(diisopropylphenyl)-terrylene-

- 3,4:11,12-bis(dicarboximide) as electron acceptor for solar cells application. *Synth. Met.*, **161**, 23, 2669 (2012). doi: [10.1016/j.synthmet.2011.09.041](https://doi.org/10.1016/j.synthmet.2011.09.041). arXiv: [1110.0658](https://arxiv.org/abs/1110.0658).
9. H. Braunschweig, V. Dyakonov, J. O. C. Jimenez-Halla, K. Kraft, I. Krummenacher, K. Radacki, A. Sperlich and J. Wahler. An Isolable Radical Anion based on the Borole Framework. *Angew. Chem. Int. Ed.*, **51**, 12, 2977 (2012). doi: [10.1002/anie.201108632](https://doi.org/10.1002/anie.201108632).
 10. H. Braunschweig, V. Dyakonov, J. O. C. Jimenez-Halla, K. Kraft, I. Krummenacher, K. Radacki, A. Sperlich and J. Wahler. Ein isolierbares Borol-basiertes Radikalanion. *Angew. Chem.*, **124**, 12, 3031 (2012). doi: [10.1002/ange.201108632](https://doi.org/10.1002/ange.201108632).
 11. J. Behrends, A. Sperlich, A. Schnegg, T. Biskup, C. Teutloff, K. Lips, V. Dyakonov and R. Bittl. Direct Detection of Photoinduced Charge Transfer Complexes in Polymer:Fullerene Blends. *Phys. Rev. B*, **85**, 12, 125206 (2012). doi: [10.1103/PhysRevB.85.125206](https://doi.org/10.1103/PhysRevB.85.125206). arXiv: [1107.5649](https://arxiv.org/abs/1107.5649).
 12. D. Riedel, F. Fuchs, H. Kraus, S. V  th, A. Sperlich, V. Dyakonov, A. A. Soltamova, P. G. Baranov, V. A. Ilyin and G. V. Astakhov. Resonant addressing and manipulation of silicon vacancy qubits in silicon carbide. *Phys. Rev. Lett.*, **109**, 22, 226402 (2012). doi: [10.1103/PhysRevLett.109.226402](https://doi.org/10.1103/PhysRevLett.109.226402). arXiv: [1210.0505](https://arxiv.org/abs/1210.0505).
 13. J. Niklas, K. L. Mardis, B. P. Banks, G. M. Grooms, A. Sperlich, V. Dyakonov, M. Leclerc, L. Yu and O. Poluektov. Highly-Efficient Charge Separation and Polaron Delocalization in Polymer-Fullerene Bulk-Heterojunctions: A Comparative Multi-Frequency EPR & DFT Study. *Phys. Chem. Chem. Phys.*, **15**, 24, 9562 (2013). doi: [10.1039/c3cp51477c](https://doi.org/10.1039/c3cp51477c). arXiv: [1305.6434](https://arxiv.org/abs/1305.6434).
 14. D. Stich, F. Sp  th, H. Kraus, A. Sperlich, V. Dyakonov and T. Hertel. Triplet-triplet exciton dynamics in single-wall carbon nanotubes. *submitted*, (2013).
 15. D. Riedel, V. A. Soltamov, H. Kraus, S. V  th, F. Fuchs, A. Sperlich, V. Dyakonov, P. G. Baranov, V. A. Ilyin and G. V. Astakhov. Room temperature quantum microwave emitters based on spin defects in silicon carbide. *submitted*, (2013).
 16. O. Poluektov, J. Niklas, K. L. Mardis, S. Beaupr  , M. Leclerc, J. L. Delgado, N. Mart  n, A. Sperlich and V. Dyakonov. Charged and Neutral Excitation on Fullerene Heterodimers in Organic Photovoltaic Bulk-Heterojunctions. *submitted*, (2013).
 17. A. Sperlich, S. V  th, J. R  mer, H. Kraus and V. Dyakonov. Charge Transfer in Polymer:PC₆₀BM:PC₇₀BM Ternary Blends: Where is the Electron Going? *in preparation*, (2013).
 18. H. Kraus, S. V  th, J. Kern, A. F  rtig, A. Sperlich, C. Deibel and V. Dyakonov. Triplet Excitons and Electron Back Transfer in PTB7:PC₇₀BM Organic Solar Cells. *in preparation*, (2013).

Contributed Talks

1. DPG Frühjahrstagung 2009 in Dresden. A. Sperlich, H. Kraus, C. Deibel and V. Dyakonov. Oxygen-Influence on the polymer semiconductor P3HT studied by Photoluminescence and Electron Spin Resonance.
2. DPG Frühjahrstagung 2010 in Regensburg. A. Sperlich, M. Liedtke, H. Kraus, O. Poluektov, C. Deibel, N. Martín and V. Dyakonov. Spectroscopic signatures of C₇₀-Anions in Polymer-Fullerene composites.
3. DPG Frühjahrstagung 2011 in Dresden. A. Sperlich, T. Savenije, M. Zawadzki, H. Kraus, C. Deibel and V. Dyakonov. Light induced spin-interacting charge-transfer states in polymer:C₆₀-fullerene blends.
4. ECME (European Conference on Molecular Electronics) 2011 in Barcelona: A. Sperlich, M. Liedtke, H. Kraus, A. Baumann, C. Deibel, C. M. Cardona and V. Dyakonov. Triplet Exciton Generation and Electron Back Transfer in BHJ Solar Cells based on Endohedral Fullerenes.
5. DPG Frühjahrstagung 2012 in Berlin. A. Sperlich, J. Römer, H. Kraus, C. Deibel and V. Dyakonov. Charge Transfer in Polymer:PC₆₀BM:PC₇₀BM triple Blends: Which Fullerene gets the Electron?
6. DPG Frühjahrstagung 2013 in Regensburg. A. Sperlich, H. Kraus, S. Väh, A. Förting, C. Deibel and V. Dyakonov. Triplet Exciton Generation and Electron Back Transfer in Organic Solar Cells.
7. ECS Spring Meeting 2013 in Toronto. A. Sperlich and V. Dyakonov. Triplet Exciton Generation and Electron Back Transfer in Photovoltaic Bulk-Heterojunctions with Endohedral Fullerenes.

Conference Posters

1. DPG Frühjahrstagung 2007 in Regensburg. A. Sperlich, M. Liedtke, J. Sieger, C. Deibel, I. Riedel, V. Dyakonov and N. Martín. Photoinduced polarons in conjugated polymer-fullerene composites studied with light-induced electron-spin resonance.
2. DPG Frühjahrstagung 2008 in Berlin. A. Sperlich, J. Friedman, I. Riedel, C. Deibel and V. Dyakonov. Electron spin resonance studies of sol-gel-processed mesoporous anatase-TiO₂-films and charge transfer in blends with P3HT.
3. Bayern Innovativ Cluster-Konferenz "Organische Photovoltaik" 2010 in Würzburg. A. Sperlich, H. Kraus, M. Zawadzki, C. Deibel and V. Dyakonov. Taking OPV for a Spin: Magnetic Resonance Techniques Reveal Charged States and Loss Mechanisms.

4. Energy & Environmental Science Poster Prize zur SPP 1355 Summer School together with Hannes Kraus. Veitshöchheim 2011. H. Kraus, A. Sperlich, S. Väh, A. Topczak, M. Zerson, R. Magerle, C. Deibel and V. Dyakonov. Magnetic resonance of solar cell materials: The influence of morphology and excitation pathways.
5. EUROMAR (European conference on Magnetic Resonance) 2011 in Frankfurt am Main. A. Sperlich, M. Liedtke, H. Kraus, C. Deibel and V. Dyakonov. Triplet Exciton Generation in Organic Solar Cells.
6. Bayern Innovativ Cluster-Konferenz "Organische Photovoltaik" 2011 in Würzburg. H. Kraus, A. Sperlich, S. Väh, A. Topczak, C. Deibel and V. Dyakonov. Magnetic resonance of solar cell materials: The influence of morphology and excitation pathways.
7. EUROMAR (European conference on Magnetic Resonance) 2012 in Dublin. A. Sperlich, S. Väh, H. Kraus and V. Dyakonov. Conjugated Polymer Microstructure Probed by Triplet State ODMR Spectroscopy.

Supervised Diploma and Master Theses

1. Björn Titze, 09-2008 "Elektronenspinresonanz-Untersuchungen von Degradationsprozessen in Polymer-Fulleren-Blends: Einfluss von Sauerstoff und thermischem Tempern"
2. Hannes Kraus, 11-2009 "Optisch detektierte Magnetresonanzspektroskopie an organischen Halbleitern"
3. Magdalena Zawadzki, 01-2011 "Zeitaufgelöste Elektronen-Spin-Resonanz-Spektroskopie an organischen Halbleitern"
4. Johannes Erben, 07-2011 "Time-Resolved Microwave Conductivity Measurements on Organic Semiconductors"
5. Stefan Väh, 11-2011 "Winkelaufgelöste Photolumineszenz detektierte Magnetresonanz an organischen Halbleitern", supervised together with Hannes Kraus.
6. Johannes Römer, 12-2011 "Multifrequenz-Elektronenspinresonanz an Materialsystemen der organischen Photovoltaik"
7. Andreas Fritze, 07-2012 "Transiente Mikrowellenabsorption an Dünnschichten organischer Halbleiter"
8. Daniel Riedel, 09-2012 "Resonant optical addressing and multi-quantum spin resonances of silicon vacancy defects in silicon carbide", supervised together with Hannes Kraus and Georgy Astakhov.
9. Maximilian Geßner, 04-2013 "Multifrequenz-Elektronenspinresonanz-Spektroskopie an Materialsystemen der organischen Photovoltaik"

7.3 Lebenslauf

Friedrich Andreas Sperlich

geboren am 25. März 1981 in Essen

verheiratet

Schulbildung

- | | |
|-------------|---|
| 1987 – 1991 | Grundschule Kölner Straße, 57290 Neunkirchen |
| 1991 – 2000 | Dietrich-Bonhoeffer-Gymnasium, 57290 Neunkirchen
Abitur, Note 1,3 (sehr gut) |

Grundwehrdienst

- | | |
|-----------------|----------------|
| 7/2000 – 3/2001 | 35279 Neustadt |
|-----------------|----------------|

Studium

- | | |
|-----------------|---|
| 4/2001 – 3/2007 | Physik (Diplom) an der Universität Würzburg |
| 4/2006 – 3/2007 | Diplomarbeit am Lehrstuhl für Energieforschung / Experimentelle Physik VI bei Prof. V. Dyakonov
Thema: <i>Elektronenspinresonanz-Untersuchungen an Polymerhalbleitern und ihren Blends</i> |
| 3/2007 | Diplom, Note: sehr gut |

Promotion

- | | |
|-----------------|---|
| 5/2007 – 5/2013 | Promotion an der Universität Würzburg bei Prof. V. Dyakonov
Thema: <i>Electron Paramagnetic Resonance Spectroscopy of Conjugated Polymers and Fullerenes for Organic Photovoltaics</i> |
| 5/2013 | Abschluß der Promotion. |

7.4 Danksagung

Am Ende dieser Arbeit möchte ich mich bei denen bedanken, die mich begleitet und unterstützt haben. Durch euch ist es mir erst möglich gewesen diese Promotion durchzuführen. Mein Dank gilt:

- Meinem Doktorvater Vladimir Dyakonov für die Möglichkeit diese Doktorarbeit am Lehrstuhl EP VI anzufertigen und dabei gleich eine ganze EPR-Arbeitsgruppe aufbauen zu können. Die Herausforderung hat mir viel Freude bereitet und durch die gegebene wissenschaftliche Freiheit, verbunden mit ausschweifenden Diskussionen, habe ich viel lernen können. Danke dafür!
- Aus dem Team der EP VI gilt mein besonderer Dank meinem Büro-Kollegen und guten Freund Hannes Kraus. Viele technische Probleme hätte ich nicht alleine lösen können und es war gut, nicht der einzige Nerd am Lehrstuhl zu sein ;-)
- Carsten Deibel danke ich für die Betreuung und seinen “kritischen Blick” auf wissenschaftliche Ergebnisse und Publikationen.
- Allen weiteren Kollegen an der EP VI, mit denen zusammen gemeinsam der Lehrstuhl von Null aufgebaut wurde, möchte ich hiermit für die tolle Arbeitsatmosphäre danken. Es hat Spaß und damit das Arbeiten leicht gemacht.
- Ebenso möchte ich den vielen Studenten danken, die unter meiner Betreuung ihre Diplom- und Masterarbeiten erstellt haben. (Siehe auch 7.2).
- Spezieller Dank gilt auch den externen Kooperationspartnern Oleg Poluektov (Argonne National Laboratory, US) und Tom Savenije (TU Delft, The Netherlands) für die produktive Zusammenarbeit.
- Ohne die Chaoten von Nerd2Nerd hätte mir Etwas gefehlt an der Uni. Das gemeinsame Ausleben unseres Spieltriebes und das Donnerstägliche Pizzaessen, sowie Dauer-IRCGen waren willkommene Support-Group und Freizeitvertreib. Ich hoffe es geht weiter so!

Zum Schluss möchte ich den wichtigsten Menschen danken - Meinen Eltern und meiner lieben Frau Marija. Für Euren Rückhalt und die anhaltende Unterstützung möchte ich Euch ganz herzlich danken.

Acknowledgment

The work at the University of Würzburg was supported by the German Research Foundation, DFG, within the SPP 1355 “Elementary Processes in Organic Photovoltaics” (DY18/6-1,2 and 3) and the BMBF in the framework of the OPV Stability Project (Contract No. 03SF0334F).